The Astrophysical Journal Supplement Series, 271:40 (48pp), 2024 April https://doi.org/10.3847/1538-4365/ad2166

Toward Precision Cosmology with Improved Planetary Nebula Luminosity Function Distances Using VLT-MUSE. II. A Test Sample from Archival Data

George H. Jacoby[1], Robin Ciardullo[2,3], Martin M. Roth[4], Magda Arnaboldi[5], and Peter M. Weilbacher[4]
[1] NSF's NOIRLab, 950 N. Cherry Ave., Tucson, AZ 85719, USA; george.jacoby@noirlab.edu
[2] Department of Astronomy & Astrophysics, The Pennsylvania State University, University Park, PA 16802, USA
[3] Institute for Gravitation and the Cosmos, The Pennsylvania State University, University Park, PA 16802, USA
[4] Leibniz Institute for Astrophysics Potsdam (AIP), An der Sternwarte 16, 14482 Potsdam, Germany
[5] European Southern Observatory, Karl-Schwarzschild-Straße 2, 85748, Garching, Germany
Received 2023 October 6; revised 2023 December 6; accepted 2023 December 7; published 2024 March 20

Abstract

Thanks to the MUSE integral field spectrograph on board the Very Large Telescope (VLT), extragalactic distance measurements with the [O III] λ5007 planetary nebula luminosity function (PNLF) are now possible out to $\sim$40 Mpc. Here we analyze the VLT/MUSE data for 20 galaxies from the ESO public archive to identify the systems' planetary nebulae (PNe) and determine their PNLF distances. Three of the galaxies do not contain enough PNe for a robust measure of the PNLF, and the results for one other system are compromised of the galaxy's internal extinction. However, we obtain robust PNLF distances for the remaining 16 galaxies, two of which are isolated and beyond 30 Mpc in a relatively unperturbed Hubble flow. From these data, we derive a Hubble constant of 74.2 ± 7.2 (stat) ± 3.7 (sys) km s^{-1} Mpc^{-1}, a value that is very similar to that found from other quality indicators (e.g., Cepheids, the tip of the red giant branch, and surface brightness fluctuations). At present, the uncertainty is dominated by the small number of suitable galaxies in the ESO archive and their less-than-ideal observing conditions and calibrations. Based on our experience with these systems, we identify the observational requirements necessary for the PNLF to yield a competitive value for H_0 that is independent of the Type Ia supernova distance scale.

Unified Astronomy Thesaurus concepts: Galaxies (573); Distance indicators (394); Hubble constant (758); Planetary nebulae (1249)

Supporting material: animations, machine-readable table

1. Introduction

The technique of obtaining distances using the planetary nebula luminosity function (PNLF) is now over three decades old (Ciardullo et al. 1989). During this time, most planetary nebula (PN) surveys were conducted with narrowband interference filters tuned to the wavelength of [O III] λ5007 (and sometimes Hα) at the redshift of the targeted galaxy. In practice, this meant performing PN photometry on images taken through $\sim$40 Å wide bandpasses and accepting the background noise associated with the filter width. This effectively limited the technique to objects within $\sim$15 Mpc —a range that, until recently, was similar to that of the Cepheid and the tip of the red giant branch (TRGB) techniques.

Today, observations through wide-field integral field spectrographs (IFS) have supplanted interference filter-based photometry for deep PNLF observations. In particular, the Multi-Unit Spectroscopic Explorer (MUSE) optical IFS (Bacon et al. 2010) has revolutionized PNLF measurements to both spiral and elliptical galaxies by coupling the large aperture and excellent image quality of the 8.2 m Very Large Telescope (VLT) with the effective resolution of an $R \sim 2000$ spectrograph. By reducing the sky + galaxy noise underlying each PN by more than a factor of 10 and allowing the simultaneous measurement of several spectral lines (such as [O III] λ5007, Hα, and [S II] $\lambda\lambda$6716, 6731), MUSE has facilitated the identification of large numbers of extragalactic PNe with almost no contamination from interloping objects, such as H II regions, supernova remnants (SNRs), and background emission-line galaxies. The result has been PNLF measurements to several dozen spiral and elliptical galaxies within $\sim$20 Mpc (e.g., Spriggs et al. 2021; Scheuermann et al. 2022). Moreover, Roth et al. (2021) have shown that through the careful use of a differential emission-line filter (DELF) technique, precision PN photometry is now possible out to distances as far away as $\sim$40 Mpc.

This changes the landscape for the PNLF method. When the PNLF was restricted to distances of $\lesssim$20 Mpc, it could only be used as an inter-method cross check that might detect deficiencies or systematic offsets between Population I standard candles, such as Cepheids, and techniques that work best in Population II systems, i.e., the TRGB and surface brightness fluctuations (SBF). However, by enabling PN photometry out to $\sim$40 Mpc, MUSE allows the PNLF to be competitive with the very deepest Cepheid (Riess et al. 2022) and TRGB (Jang & Lee 2017) measurements obtained from space. Moreover, at a distance of $\sim$40 Mpc, the typical peculiar velocity of a galaxy is only 10% that of the Hubble flow. Thus, PN photometry in a sample of $\sim$50 galaxies beyond $\sim$30 Mpc can place a meaningful constraint on the Hubble constant that is independent of the Type Ia supernova (SN) calibration.

In this paper, we apply the photometric methods described in Roth et al. (2021, hereafter Paper I) and the analysis techniques detailed in Chase et al. (2023) to further illustrate the ability of the PNLF to yield accurate distances to galaxies well beyond the Local Supercluster. We do this by using the archival MUSE

data cubes of 20 representative galaxies spanning a wide range of distances, absolute magnitudes, and Hubble types. We also examine possible systematic errors associated with the PNLF and examine strategies to improve the precision of the method. In short, this paper explores the range over which the PNLF can be used effectively to derive reliable extragalactic distances.

In Section 2, we describe our criteria for selecting promising PNLF targets from the MUSE archive. In Section 3, we review our method of identifying faint PN candidates in the target galaxies, removing interloping objects such as H II regions and SNRs, and measuring the planetary nebulae's (PNe's)apparent [O III] λ5007 magnitudes. In Section 4, we outline our method of deriving distances from the PNLF, including the case where unrecognized PN superpositions may be present in the data set. In Section 5, we present our PNLF distances and provide brief commentaries on the unique challenges presented by each galaxy. In Section 6, we compare our results to those of other techniques and assess the reliability/repeatability of the distances.

2. Galaxy Selection

The ESO science archive contains a large number of galaxies with MUSE observations. For this paper, we examined the database as of 2021 December 5 to identify a set of galaxies amenable to PNLF measurements that also provide an adequate and diverse sample to demonstrate the applicability of the technique. We then refined our list based on the following criteria:

1. Good image quality (i.e., a point-source full width at half-maximum (FWHM) $<1\farcs0$): The dominant source of noise for any extragalactic PN measurement is the background. Consequently, the identification and measurement of PNe against the continuum light of a host galaxy is a strong function of image quality, especially in the bright central regions where the highest density of PNe is located. Moreover, as the seeing degrades, the likelihood that two, closely separated PNe will be recorded as a single, bright object increases; this effect can distort the observed shape of the PNLF and lead to a systematic error in the galaxy's derived distance and its uncertainty (e.g., Chase et al. 2023). Thus, in order to obtain a large statistically complete sample of PNe with a minimal number of image blends, one generally requires excellent seeing. Image quality was therefore of paramount importance for our choice of galaxies.
2. Effective exposure time ($t > 3600$ s): PNLF distances are defined by the apparent magnitude of the rapid cutoff seen at the bright end of the PN luminosity function. A high-precision measurement of this cutoff magnitude (m^*) requires that the PN sample be reasonably complete at least $\sim$0.5 mag fainter than this cutoff, and preferably to $m^* + 1$. In $\sim1''$ seeing, the exposure time needed for MUSE to detect such objects in a galaxy $\sim$20 Mpc away is roughly 1 hr.
3. Likely distance ($D < 30$ Mpc): In almost all cases, a galaxy's recessional velocity, coupled with a bulk-motion model (e.g., Lynden-Bell et al. 1988; Tonry et al. 2000; Shaya et al. 2017) provides a rough estimate of its distance; for a subset of galaxies, very good distance estimates exist from the measurement of resolved (or semiresolved) stars. If this distance is too great and if the exposure time is not long enough to compensate, the data will not reach deep enough to observe the PNLF cutoff. Since one goal of this study is to compare MUSE PNLF distances to distances obtained from other indicators, we focused on targets that promised to yield good results, i.e., galaxies within $\sim$30 Mpc. We analyze more distant systems only if the exposure times are long and the image quality is excellent; in Paper I, for example, we included NGC 474 at $\sim$37 Mpc, as its halo was observed for 10 hr in $0\farcs78$ seeing.
4. Surveyed luminosity ($M_V < -19$): Bright planetary nebulae (PNe) are rare objects: from the fuel consumption theorem, an $M_V \sim -21.2$ galaxy will create only one PN per year (Renzini & Buzzoni 1986; Buzzoni et al. 2006), and less than $\sim$2% of all PNe are in the top $\sim$1 mag of the PN luminosity function. As a result, in order for the top magnitude of the PNLF to be well populated, one needs to survey at least $M_V \sim -19.5$ of galactic light (e.g., Ciardullo et al. 2005; Buzzoni et al. 2006). PN surveys of dwarf galaxies and systems with only limited MUSE coverage will, at best, produce distances with large error bars.
5. Preference for having Cepheid, TRGB, or SBF distances in the literature: There are exactly zero galaxies whose distances are known a priori; the two systems that come closest to satisfying this criterion are the Large Magellanic Cloud (LMC; via eclipsing binaries and the SN 1987A light echo; Panagia et al. 1991; Pietrzyński et al. 2019) and NGC 4258 (via the geometry of its megamaser; Reid et al. 2019). The best one can do to validate the results of any distance indicator is to compare its results to those obtained from other methods. Still, this type of analysis only demonstrates consistency, not correctness. At this time, Cepheid and TRGB distances lead the way in terms of perceived accuracy, with SBF results close behind. Thus, to achieve the goal of validating the accuracy of the PNLF, we prefer to include targets with distances measured using well-established techniques.
6. Preference for hosting Type Ia supernovae (SNe): There are two ways to view this selection criterion. If a galaxy hosts a Type Ia SN, then a PNLF distance can be used to calculate the SN's peak luminosity, and thereby improve the calibration of SN Ia as a distance indicator. Alternatively, we can use the existing SN Ia measurements to provide another check on the PNLF distances. Unfortunately, at the time of our galaxy selection, there were only four known Type Ia SNe (in three galaxies) that had MUSE archival observations which satisfied our other criteria (though more may exist in the future).

Table 1 gives the resultant list of the galaxies. The group is quite diverse and includes a central cD galaxy (NGC 1399), a low-luminosity active galactic nucleus (AGN) with two, apparently dark matter-less satellite dwarfs (NGC 1052), a Seyfert 2 galaxy with a megamaser (NGC 4418), two spiral galaxies undergoing interactions (NGC 4038/39 and NGC 1385), and several normal elliptical, lenticular, and spiral systems. Such diversity allows us to test the methods detailed in Paper I in different environments and provides a guide to the range of galaxies amenable to future PNLF measurements.

Table 1
List of Galaxies Analyzed

Galaxy	GSR Velocity				Range of Distances (Mpc)			SN Ia Name
	Type[a]	(km s^{-1})[b]	$E(B-V)$[c]	M_B[d]	Cepheid[e]	TRGB[e]	SBF[e]	
NGC 253	Sc	243	0.0161	−20.0	…	3.3–3.9	…	…
NGC 1052	E3/S0	1473	0.0228	−19.8	…	…	18.0–20.6	…
NGC 1326	SBa	1242	0.0163	−19.8	…	…	…	…
NGC 1351	$S0_1$/E6	1396	0.0115	−18.3	…	…	19.2–22.6	…
NGC 1366	$S0_1$	1120	0.0139	−17.5	…	…	18.6–21.2	…
NGC 1385	Sc	1400	0.0173	−19.8	…	…		…
NGC 1399	E1 (cD)	1301	0.0109	−20.3	…	…	17.6–21.4	…
NGC 1404	E2	1823	0.0097	−19.9	…	18.1[f], 18.7[g]	17.9–22.2	SN 2007on, SN 2011iv
NGC 1419	$E0_p$	1442	0.0112	−17.5	…	…	19.2–22.9	…
NGC 1433	SBb	928	0.0078	−19.7	…	9.0	…	…
NGC 1512	SBb_p	746	0.0091	−19.0	…	11.4–11.9	…	…
NGC 2207	Sc	2577	0.0748	−21.9	…	…	…	SN 1975A
NGC 3501	Scd	1057	0.0200	−18.9	…	…	…	
NGC 4038/9	Sc_p	1548	0.0398	−21.1	18.1–21.5	20.0–21.6, 21.7[f]	…	SN 2007sr
NGC 4365	E3	1170	0.0184	−20.5	…	…	20.4–23.6	…
NGC 4418	S0/a	2027	0.0202	−19.0	…	…	…	…
NGC 4472	E1/$S0_1$	913	0.0191	−21.8	…	…	14.5–17.8	…
NGC 5248	Sbc	1126	0.0210	−21.1	…	…	…	…
NGC 6958	$S0_1$	2730	0.0385	−20.5	…	…	…	…
MCG-06-08-024	$E4_p$	1692	0.0101	−16.1	…	…	19.2–19.5	…

Notes.
[a] From de Vaucouleurs et al. (1991).
[b] From NED.
[c] From Schlafly & Finkbeiner (2011).
[d] All total B magnitudes estimated from the Nearby Galaxies Catalog (Tully 1988) and NED, except for NGC 4418, which is derived from de Vaucouleurs et al. (1991) and our own distance modulus of $(m-M)_0 = 32.59$.
[e] Compiled by NED, except where noted.
[f] From Anand et al. (2022).
[g] From Hoyt et al. (2021).

3. Observations and Reductions

For our analysis, we extracted publicly available, fully reduced MUSE data cubes of the galaxies listed in Table 1 from the ESO archive (Romaniello et al. 2018). These data, which were obtained between 2014 June 25 and 2020 December 5, were taken under a variety of observing conditions, with exposure times ranging between 621 and 9600 s, and seeing (as listed in the archive) between 0.″51 and 1.″27. Because MUSE consists of 24 identical IFSs, which, in its wide-field mode, covers only a $1' \times 1'$ field of view, most galaxies in our list were only partially surveyed via a small number of pointings. In many cases, these pointings overlapped, allowing (at least in theory), a consistency check of each data cube's flux calibration.

To identify and measure the PNe in these galaxies, we used the DELF technique, which is described in detail in Paper I. This method, which is the IFS equivalent of the traditional on-band/off-band procedure commonly used with interference filters, maximizes the contrast of emission-line objects over the background while minimizing spaxel-to-spaxel flat-field residuals associated with the instrument. We outline our steps below. With DELF, each PN effectively is observed through its own optimized and tuned 3.75–6.25 Å narrowband filter.

After downloading a data cube from the archive, we create a 125 Å wide intermediate-bandwidth *continuum* image from the coaddition of 100 contiguous data cube layers centered ∼90 Å redward of [O III] λ5007 at the redshift of the galaxy. We then subtract a scaled version of this image from each of the cube's 15 layers surrounding [O III] λ5007 to create 15 *difference images*, one for each 1.25 Å data slice.

Next, to identify the PNe, we stepped through the 15 difference images, summing up three adjacent images at a time, and visually inspecting the frames for emission-line sources. Since the wavelength resolution of MUSE at ∼5000 Å is roughly 2.5 Å (i.e., twice the dispersion of the data cube), any pointlike object appearing on three consecutive frames was considered a PN candidate.

Once these candidates were identified, their spectra were extracted in a small aperture, typically with a radius of 3–5 spaxels (0.″6–1.″0), depending on the seeing. The [O III] emission lines were then examined for evidence of asymmetric, double-peaked, or broadened line profiles. If a line profile was well behaved, its total flux was obtained by modeling the emission with a Gaussian model; otherwise, an interactive tool was employed to deblend the Gaussian associated with the PN in question from other spectral components (usually arising from diffuse gas or other superposed sources).

Aperture corrections were then found by identifying bright point sources in the field, coadding 160 layers of the original data cube centered at redshifted λ5007, and measuring the stars' growth curves. The total flux of each object was then translated into an [O III] λ5007 magnitude, m_{5007} via

$$m_{5007} = -2.5 \log F_{5007} - 13.74, \quad (1)$$

where F_{5007} is the [O III] line flux in erg cm^{-2} s^{-1}.

Finally, the full spectrum of each object was inspected to exclude H II regions (using the ratio of Hα to [O III]; Herrmann

et al. 2008), SNRs (based on the strength of [S II] relative to Hα; Kreckel et al. 2017), and background Lyα emitting galaxies (from the line profile and the lack of other spectral features; Kudritzki et al. 2000; Arnaboldi et al. 2002). Furthermore, any object with only a single line was rejected because it could not be confirmed as a PN; these were always quite faint. A full description of this process is given in Paper I.

4. Obtaining a PNLF Distance

4.1. Historical Approach

The shape of the PNLF is not universal: in old stellar populations, the slope at faint magnitudes changes from galaxy to galaxy (e.g., Longobardi et al. 2013; Hartke et al. 2017, 2020; Bhattacharya et al. 2021), while in star-forming systems, the PNLF is known to contain multiple inflection points (Jacoby & De Marco 2002; Ciardullo 2010; Reid & Parker 2010). However, at the extreme bright end of the function, the PNLF's behavior is remarkably invariant and consistent with an abrupt truncation of an underlying power law. Moreover, measurements of roughly a dozen galaxies within ∼10 Mpc show that for systems more metal-rich than the LMC, the absolute magnitude where this truncation takes place is extraordinarily insensitive to stellar population (e.g., Ciardullo 2013). Thus, the traditional method of deriving a PNLF distance involves fitting the observed distribution of apparent [O III] λ5007 magnitudes to a function that captures the PNLF's truncation, such as

$$N(M) \propto e^{0.307M}\{1 - e^{3(M^*-M)}\}, \quad (2)$$

where $M^* = -4.54$ is the [O III] λ5007 absolute magnitude of the brightest possible planetary. This procedure proved extremely successful for galaxies within ∼10 Mpc, but beyond this distance, the values obtained from the PNLF were generally ∼0.2 mag smaller than those from Cepheids and the SBF method. This offset suggested the presence of one or more systematic errors (e.g., Ferrarese et al. 2000; Ciardullo 2022), such as the inclusion of contaminating objects (i.e., SNRs, H II regions, and background galaxies) in the PN samples, or an incorrect expression for the shape of the PNLF cutoff.

4.2. Recent Improvements with MUSE

The MUSE analyses by Spriggs et al. (2021) and Scheuermann et al. (2022) have pointed to another possible error in the PNLF: the projection of two separate PNe onto a single spatial (and spectral) resolution element. Although a chance alignment of two rare objects would seem improbable, Paper I demonstrated that photometric blends occur more often than previously realized. When this happens, a source may appear to have the spectrum of a normal PN, but with an [O III] magnitude that is up to 0.75 mag brighter than M^*. This can distort the observed PN luminosity function and lead to an incorrect (underestimated) value for both the PNLF distance and its uncertainty.

Chase et al. (2023) detailed the procedures needed to include the possibility of image blends in a PNLF analysis. In brief, if the [O III] fluxes of two superposed PNe are uncorrelated, the probability density function (PDF) for their summed [O III] flux is simply the convolution of the single object PDF with itself. At any position in a galaxy, the probability of observing a PN with a given magnitude m is therefore given by the weighted sum of two PDFs: one for single objects (Equation 2) and one for superpositions. Under the assumption that the distribution of PNe within a galaxy follows that of the underlying light, the weights of the two PDFs can be found by applying Poisson statistics to the number of PNe expected to be found on a single resolution element of data. This expectation value can then be estimated from the surface brightness of the galaxy, the total number of PNe observed, the velocity dispersion of the galaxy's stars, the image quality of the data, and the spectral resolution of the instrument.

Note that in our analysis, the expected PDF for every PN candidate depends not only on the form of the empirical function (Equation (2)) but also on the galactic surface brightness and velocity dispersion underlying the PN's location. Thus, one cannot simply fit the data with a single curve: a galaxy's best-fit distance must be derived by maximizing the combined likelihoods of the entire PN sample based on their individual PDFs. When PN blends are a possibility, histograms and cumulative distributions of PN magnitudes are useful visualization tools, but should not be used as the basis for a quantitative analysis.

4.3. Implementation of the Correction for PN Superpositions

As stated in the previous two paragraphs, a PNLF distance analysis, which includes the possibility of blends requires having some idea of the surface brightness distribution of the galaxy, the velocity dispersion of the stars underlying the position of each PNe, and the spectral and spatial resolution of the data (i.e., how close can two PNe be before we cannot tell there are two objects at one location). These values do not necessarily need to be precise, as there is some degeneracy between the parameters. However, PNLF analyses that do not include these factors can produce distances (and associated uncertainties) that are underestimated.

The most important parameters for modeling the effect of blends on the PNLF are the total amount of galaxy light sampled by a PN survey and the galactic surface brightness underlying the position of each PN. These data can either be estimated from previously published surface photometry, or from continuum measurements off the MUSE data cubes themselves. Of secondary importance is the stellar line-of-sight velocity dispersion at each PN's position in the galaxy. Such data are not available for all galaxies, and even then, the precision of the measurements is generally limited. Fortunately, PNLF distances are generally not very sensitive to this parameter, and any error in this quantity is easily subsumed into the overall error budget of the calculation. Finally, any analysis that includes the possibility of PN superpositions must include the spatial and spectral resolution of the data cube at the wavelength of the observed emission line. Simulations performed by Chase et al. (2023) show that to a good approximation, two adjacent PNe can only be spatially resolved in a MUSE data cube if their angular separation is greater than half the seeing FWHM or their velocity difference is greater than $\Delta v \approx 200$ km s^{-1}.

5. Results

In the following subsections, we present basic data for our program galaxies, including a summary of detected PN candidates, any peculiar challenges associated with the

analysis, and the results of fitting the empirical PNLF of Equation (2) to the data while including the possibility of PN superpositions (Chase et al. 2023). The galaxies selected include both early- and late-type systems, and their PN populations range from more than 200 detected objects, down to just a handful of PN candidates. Throughout the analysis, we assume the Milky Way foreground extinction model of Schlafly & Finkbeiner (2011) and $A_{5007} = 3.47E(B-V)$ (Cardelli et al. 1989).

The PNLF analyses presented below all involve solving for two variables: the distance modulus, which, in graphical form, shifts the fitted curve along the x-axis, and a (log) normalization, which offsets the curve in y. Since the fuel consumption theorem predicts that a stellar population's rate of PN production per unit bolometric luminosity should be almost independent of its age, metallicity, and initial mass function (Renzini & Buzzoni 1986; Buzzoni et al. 2006), we express our normalizations in terms of $\alpha_{2.5}$, the number of PNe predicted to be within 2.5 mag of M^* (assuming the shape given by Equation 2) scaled to the amount of galaxy bolometric luminosity sampled in the survey. Effectively, this means estimating the total amount of V-band light falling onto the MUSE IFS, applying a bolometric correction of B.C. $= -0.85$ (Buzzoni et al. 2006), and extrapolating the shape of the luminosity function from the survey's completeness limit to a depth that is 2.5 mag fainter than the PNLF cutoff. When expressed in this way, most galaxies have values of $\alpha_{2.5}$ between $\sim$5 and $\sim$50 PNe $L_\odot$ (Ciardullo 2010).

Our PNLF analyses carry two important caveats. The first is that the data cubes used in this work are archival, and most were obtained for purposes unrelated to our goals. Thus, many are not ideal for distance scale analysis. For example, in order to measure the total fluxes of faint PNe, one needs bright stars in the field of view, as these allow precise measurement of the data cube's point-spread function (PSF) and stellar aperture corrections. Many high galactic latitude MUSE observations do not have such stars. Similarly, since not all MUSE programs require the photometric conditions necessary for distance scale work, it is likely that the flux calibrations of some archival data cubes are more accurate than others. While we do attempt to include these uncertainties in our error budget, in some cases, the exact values are hard to quantify.

The second caveat is that all our distances are based on fitting the observed PN magnitudes to the function defined by Equation (2) with a constant value for the function's cutoff of $M^*-4.54$. It is possible that this expression does not capture the true shape of the PN magnitude distribution; for example, if the [O III] luminosity of a PN can exceed M^*—either due to high central star luminosity or a fortuitous sight line through the surrounding circum-nebular extinction—then the PNLF distances may be systematically underestimated. In addition, evidence suggests that M^* fades in the metal-poor populations that may be found in low-luminosity galaxies and in the outer halos of larger systems (e.g., Ciardullo & Jacoby 1992; Dopita et al. 1992; Richer & McCall 2008; Ciardullo 2012; Bhattacharya et al. 2021). In the absence of a metallicity correction, the PNLF technique would then overestimate the distance to the system. We comment on this latter possibility when necessary.

On the basis of our findings, we present our conclusions at the end of the paper regarding the prerequisites for targeted PNLF studies with MUSE. Unless otherwise referenced, the basic data for the selected objects were retrieved from the NASA/IPAC Extragalactic Database (NED) and SIMBAD database.

Each galaxy is depicted with a broadband red giant branch (RGB) image, which indicates where the archival MUSE fields are located, a grayscale *off-band* image, which displays the light extracted in a 50 Å bandpass longward of the redshifted [O III] and Hβ lines, and an exemplary difference image formed by subtracting the off-band image from the sum of three MUSE data cube layers centered on [O III] λ5007 at the redshift of the galaxy. These latter thumbnail images can be retrieved with full resolution through hyperlink access for immediate download.

For all but two galaxies (NGC 1433 and NGC 2207), we provide an 8 s animation (online) that begins with the off-band image and then steps through the MUSE layers centered on the galaxy's redshifted [O III] wavelength. The animation shows how all emission-line objects, especially the PNe, rise and fall in brightness with wavelength/velocity (which are noted in the corners of the video). The animation greatly facilitates the identification of the PNe compared to the static *diff* images that are provided. For the nearly face-on galaxy NGC 1433, the velocity gradient is small and so, an animation offers little insight. For NGC 2207, there are so few PNe that the animation also offers little.

A catalog of all our PN measurements, including the objects' positions, [O III] magnitudes, and the observed wavelengths of their λ5007 lines, is provided in machine-readable form with this paper; the details of this file are described in Table 3.

5.1. NGC 253

NGC 253 is an SAB(s)c starburst galaxy and the most massive member of the Sculptor group. At the time of our analysis, two MUSE data cubes of the galaxy's central regions were available in the ESO archive (IDs ADP.2018-11-22T21:29:46.157, ADP.2019-08-24T09:53:08.548, PI: L. Zschaechner, Program ID 0102.B-0078); a much more comprehensive set of observations has since been released and will be the subject of a separate paper. The exposure times of the two data cubes considered here are similar (1820 s for P1 and 1833 s for P2), and our measurements of the image quality at 5007 Å are similar (1.″06 and 0.″95 for P1 and P2, respectively). The locations of these pointings are shown in Figure 1.

The only previous PNLF study of NGC 253's PNLF is by Rekola et al. (2005), who used the classical on/off-band imaging technique to find 14 PNe in the field outlined in gray in the right panel of Figure 1. These authors also modeled the effect of dust extinction in the galaxy; while one generally does not expect the PNLF to be greatly affected by galactic internal extinction—the scale height of PNe should be several times that of the dust (e.g., Feldmeier et al. 1997; González-Santamaría et al. 2021; Guo et al. 2021)—the high inclination of NGC 253 ($i = 74°$) and the galaxy's prominent dust lanes are clearly an issue. Rekola et al. (2005) concluded that the effect of extinction on their sample of NGC 253 PNe is quite small, and derived a PNLF distance to the system of $(m-M)_0 = 27.62^{+0.16}_{-0.26}$ for a foreground reddening of $E(B-V) = 0.019$.

Our initial list of pointlike [O III] sources in NGC 253's P1 and P2 fields contained 48 and 42 objects, respectively. However, after excluding objects based on their spectra (i.e., eliminating H II regions and SNRs via the line strengths of Hα and [S II]), the list of PN candidates dropped to 19 and 15

Table 2
Archival Data Cubes

Pointing	Date of Obs.	Exp. Time (s)	Archive Seeing
NGC 253—P1	2018 Nov 7	1820	0.″89
NGC 253—P2	2019 Jul 29	1833	0.″83
NGC 1052—P1	2019 Sep 5	1685	0.″61
NGC 1326—P1	2017 Nov 19	3354	1.″11
NGC 1351—P1	2017 Nov 15	3379	0.″69
NGC 1351—P2	2016 Oct 6	4680	0.″93
NGC 1366—P1	2019 Aug 9	2445	1.″04
NGC 1385—P1	2019 Dec 31	2360	0.″74
NGC 1385—P2	2020 Dec 5	2417	1.″03
NGC 1385—P3	2020 Jan 21	2424	0.″63
NGC 1385—P4	2019 Jan 17	2418	0.″72
NGC 1385—P5	2020 Jan 20	2414	0.″67
NGC 1399—M	2014 Oct 2	954	0.″81
NGC 1404—P1	2017 Nov 22	3287	0.″70
NGC 1404—P2	2017 Nov 14	1687	0.″80
NGC 1433—P1	2019 Nov 22	2580	0.″75
NGC 1433—P2	2019 Nov 21	2580	0.″73
NGC 1433—P3	2019 Nov 20	2580	1.″05
NGC 1433—P4	2019 Oct 5	2580	0.″78
NGC 1433—P5	2016 Aug 26	3840	0.″76
NGC 1433—P6	2019 Oct 6	2580	0.″70
NGC 1433—P7	2019 Dec 21	2580	0.″82
NGC 1433—P8	2019 Dec 22	2580	0.″87
NGC 1433—P9	2019 Dec 23	2580	0.″64
NGC 1512—P1	2018 Dec 30	2406	0.″79
NGC 1512—P2	2018 Feb 17	3000	1.″75
NGC 1512—P3	2018 Feb 18	2402	0.″92
NGC 1512—P4	2018 Dec 30	2307	0.″58
NGC 1512—P5	2017 Sep 21	3280	0.″67
NGC 1512—P6	2018 Feb 19	2402	0.″65
NGC 1512—P7	2019 Jan 10	2384	1.″27
NGC 1512—P8	2019 Jan 10	2312	0.″78
NGC 1512—P9	2019 Jan 10	2300	0.″61
NGC 2207—P1	2019 Feb 19	2238	0.″83
NGC 2207—P2	2017 Nov 17	3338	0.″65
NGC 2207—P3	2017 Nov 18	3892	0.″83
NGC 3501—M	2016 Dec 30	9600	1.″51
NGC 4038/9—C1	2015 Apr 23	4951	0.″67
NGC 4038/9—C3	2015 May 11	4811	0.″58
NGC 4038/9—C4	2015 May 13	4985	0.″51
NGC 4038/9—C5	2015 May 21	5117	0.″82
NGC 4038/9—C9	2017 Apr 24	2584	0.″72
NGC 4038/9—C10	2016 May 12	2592	0.″74
NGC 4038/9—C11a	2017 Apr 23	2498	0.″79
NGC 4038/9—C11b	2017 Apr 25	2523	0.″74
NGC 4038/9—C12a	2016 Feb 1	2700	1.″22
NGC 4038/9—C12c	2016 Feb 1	2700	1.″09
NGC 4038/9—C12e	2016 Feb 4	2700	0.″86
NGC 4365—P1	2015 Feb 13	2343	0.″83
NGC 4418—P1	2020 Jan 30	5999	0.″76
NGC 4472—M1	2015 Apr 14	626	0.″72
NGC 4472—M2	2015 Jul 10	623	0.″82
NGC 4472—M3	2015 Apr 12	621	0.″93
NGC 5248—P1	2016 Apr 4	3411	0.″76
NGC 6958—P1	2017 Sep 18	1906	0.″96
MCG-06-08-024—P1	2016 Dec 27	4821	0.″67

Table 3
Contents of PN Catalog

Number	Units	Label	Description
1	...	Galaxy	Name of galaxy
2	...	PN ID	PN ID number
3	...	Field	Data cube ID
4	deg	R.A.	R.A., J2000, decimal degrees
5	deg	decl.	Decl. J2000, decimal degrees
6	mag	m_{5007}	Apparent 5007 magnitude
7	mag	e_{5007}	Uncertainty in m_{5007}
8	0.1 nm	$\lambda(5007)$	Observed wavelength of [O III] λ5007
9	...	Flag	Member of a statistically complete sample?[a]

Note.
[a] T indicates the PN was used for fitting the PNLF.

(This table is available in its entirety in machine-readable form).

sources. Unfortunately, less than a dozen of these objects have magnitudes in the top ∼1 mag of the PN luminosity function.

The derivation of NGC 253's PNLF distance presents a number of challenges. The first comes from the diffuse ionized gas (DIG) distributed throughout the field. This gas, along with the galaxy's H II regions and SNRs, is responsible for the large number of interlopers in our original list of PN candidates (red circles in the left panels of Figure 1) and for the possible existence of systematic errors in the background subtraction. As a result, the relatively small formal photometric errors associated with the brightest PNe (∼0.01 mag) do not necessarily account for the true uncertainties in our measurements. To compensate for this, we included an additional 5% error in all our photometry.

A second issue arises from the possibility of internal galactic extinction. As evidenced by their Balmer decrements, many of the PNe in NGC 253 are heavily obscured (e.g., Figure 2). Simplistic scale-height-based arguments (e.g., Feldmeier et al. 1997; González-Santamaría et al. 2021; Guo et al. 2021) suggest that internal extinction should not affect most PNLF measurements, but if NGC 253's dust is extincting the PNe, the effect should be removed before deriving a distance. Alternatively, since NGC 253 is a starburst object, it is also likely that many of its PNe have evolved from relatively high-mass progenitors. The circum-nebular extinction produced by these objects should not be touched since the component is an important contributor to the location of the PNLF cutoff (Ciardullo 2012; Davis et al. 2018). Unfortunately, since there is no easy way to disentangle the two sources of extinction, one must simply live with the possibility that internal galactic extinction, might be affecting the results. If so, then our formal PNLF distance will be an overestimate. (This argument applies to all the dusty galaxies analyzed in this paper.)

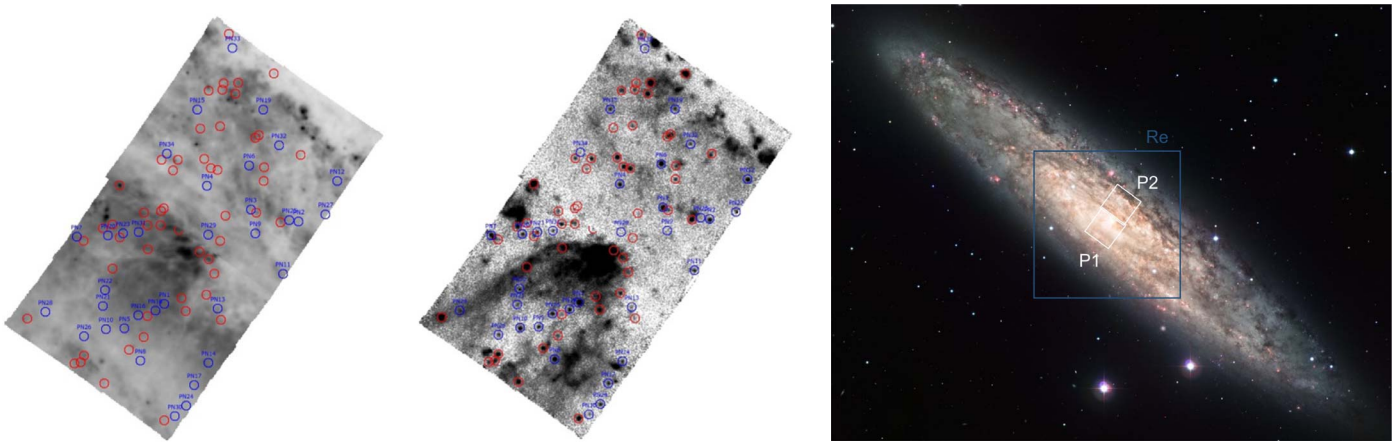

Figure 1. NGC 253. Left: thumbnail images of an off-band and difference image derived from the MUSE data cubes. Our PNe candidates are highlighted in blue, while emission-line interlopers are shown in red. Right: a broadband image showing the locations of pointings P1 and P2 (credit: ESO). A high-resolution image of the off-band and difference images is available online. The animation (available online) begins with the off-band image and then steps through the MUSE layers centered on the galaxy's redshifted [O III] wavelength to show how all emission-line objects, especially the PNe, rise and fall in brightness with wavelength.
(An animation of this figure is available.)

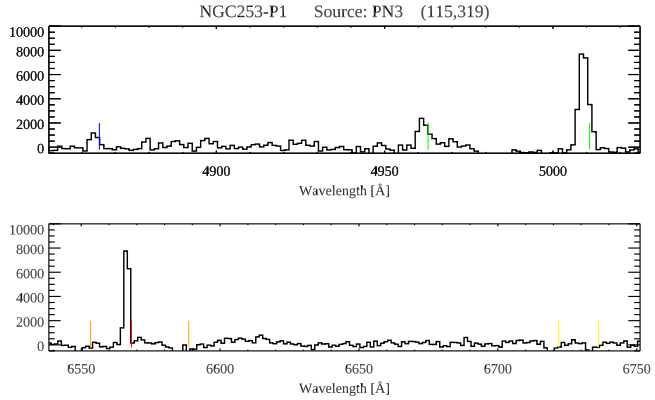

Figure 2. Blue and red regions of the spectrum of the bright, highly extincted planetary PN3 found in pointing P1 of NGC 253. The y-axis is in units of 10^{-20} erg cm^{-2} s^{-1} Å^{-1}. The extreme Hα/Hβ ratio indicates an extinction of $A_{5007} \sim 2.1$ mag.

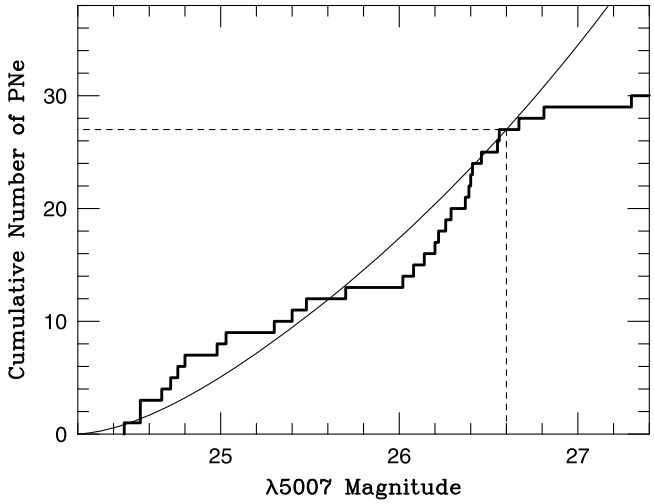

Figure 3. The cumulative luminosity function for PNe in NGC 253. The dark line represents the observed data; the curve is Equation (2) shifted to the most likely apparent distance modulus. The dashed line shows the location where incompleteness and the PNLF's star formation dip cause the curve to overpredict the number of PNe. Data brighter than this are consistent with being drawn from the empirical function.

Finally, we note that the P1 and P2 fields of NGC 253 do not possess any bright reference stars with which to determine the observations' aperture corrections. This is not an uncommon issue with MUSE archival data, since the field of view of the instrument is only $1' \times 1'$ (see Paper I). Our aperture corrections were therefore estimated using bright, compact star clusters as a reference. For distant galaxies, the use of such systems for point-source photometry should be valid, but at the distance of the Sculptor group, some of the clusters may be marginally resolved. If so, their use as *point sources* could introduce a zero-point error into our photometry and artificially brighten the PNLF. Additionally, since there is little overlap between the two MUSE fields, the errors associated with the aperture corrections may result in the photometry of the two fields having different zero-points. The systematic error introduced by this effect is discussed in Section 5.10.

Since our PN sample contains only ∼10 objects in the top magnitude of the luminosity function, a plot showing the differential distribution of these points is not very revealing. Consequently, Figure 3 plots the cumulative distribution of the PN magnitudes. (We will present cumulative distributions in later cases, as well, when the PN count is low.) The rapid departure from the distribution predicted by Equation (2) beyond $m_{5007} \sim 26.6$ is not principally due to incompleteness. Rather, it comes from a *dip* in the luminosity function ∼1.5 mag below the bright-end cutoff. This feature, which was first reported by Jacoby & De Marco (2002) for the PNLF of the SMC, is characteristic of most star-forming systems, though the exact location and strength of the dip varies with stellar population. (For a qualitative explanation of the phenomenon, see Ciardullo 2010.) At brighter magnitudes, the PN magnitude distribution follows the predictions of the empirical law quite well (i.e., a Kolmogorov–Smirnov (K-S) test cannot rule out the hypothesis that the PNe are drawn from that distribution), but with so few objects in the top ∼1 mag of the PNLF, the exact position of the function's cutoff cannot be fixed with any precision.

We used the analysis program of Chase et al. (2023) to derive NGC 253's PNLF distance. To estimate the likelihood of any PN superpositions, we used the H-band surface photometry of Forbes & Depoy (1992) to measure the

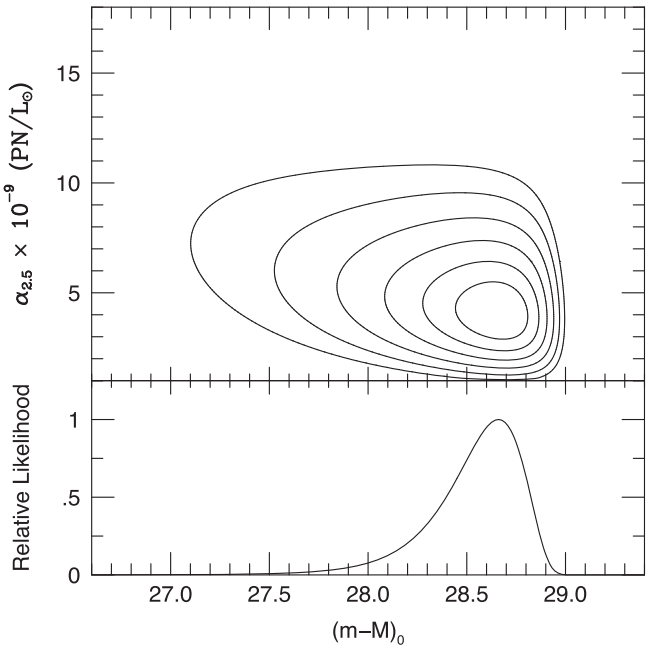

Figure 4. The results of the maximum-likelihood analysis for NGC 253. The top panel shows the likelihood contours drawn at 0.5σ intervals, with the abscissa giving the galaxy's true distance modulus, and the ordinate showing the number of PNe within 2.5 mag of M^* normalized to the amount of galactic bolometric light contained in the two MUSE data cubes. The lower panel marginalizes over this variable. The distribution is quite wide, due to the dearth of PNe in the top ∼1 mag of the luminosity function.

amount of galaxy light at each position in the data cube and converted these IR magnitudes to the V band using the galaxy's integrated optical and IR colors (Aaronson 1977; Jarrett et al. 2003). We then assumed that the spectral lines of any possible PN blend would be unresolved, as the line-of-sight velocity dispersion in a disk galaxy such NGC 253 should be much less than MUSE's spectral resolution. We then computed the galaxy's most likely distance modulus, under the assumption of a foreground Milky Way reddening of $E(B-V) = 0.016$ (Schlafly & Finkbeiner 2011).

Figure 4 shows the results of our analysis. With so few objects in the top magnitude of the luminosity function, the random error associated with our solution is substantial. If we fit NGC 253's PNLF down to a limiting magnitude of $m_{5007} = 26.6$, we obtain a galaxy distance modulus of $28.66^{+0.12}_{-0.28}$, or $5.4^{+0.3}_{-0.6}$ Mpc. This number is about a magnitude more distant than the PNLF distance found by Rekola et al. (2005) from a different set of PNe identified at larger radii in the galaxy. (Unfortunately, there are no PNe common to both data sets.) It is also a magnitude further than the galaxy's TRGB distances of ∼27.5 (e.g., Mouhcine et al. 2005; Dalcanton et al. 2009; Radburn-Smith et al. 2011).

The errors quoted above do not include the possible systematic offsets introduced by our very limited choice of aperture correction reference stars and our general lack of knowledge of the internal reddening. The former number is difficult to quantify with the present data set, while evidence for the latter is indirect. Although Rekola et al. (2005) concluded that internal extinction likely did not strongly affect their sample of NGC 253 PNe, our MUSE pointings lie much closer to the center of the galaxy, where the extinction is likely to be larger. Moreover, the best-fit value of $\alpha_{2.5}$ displayed in Figure 4 is slightly lower than expected for PN measurements in a spiral galaxy (Ciardullo 2010), suggesting that dust may be affecting PN detections.

The two MUSE data cubes analyzed in this work cover only a small fraction of the galaxy's $\sim 3 \times 10^{10} L_\odot$ of the B-band light. Thus, our result is just a feasibility test. However, since 2022 a more complete survey of NGC 253 has been published in the ESO archive. These MUSE pointings include proper aperture correction stars and should contain enough PNe to produce a PNLF statistical error comparable to that of the galaxy's TRGB distance measurement. We will address this opportunity in a future paper.

5.2. NGC 1052

NGC 1052 is a bright elliptical (E4) galaxy with a radio jet, a LINER-type nucleus, and a large-scale outflow that has been studied with the Wide-Field IFU spectrograph on the Australian National University 2.3 m telescope (Dopita et al. 2015). Recently, the system has garnered considerable attention, as two of NGC 1052's satellites, DF2 and DF4 appear to be ultradiffuse dwarf galaxies with little or no dark matter (van Dokkum et al. 2018). Since these dark matter estimates depend on the system's distance, an independent measure of this quantity is of considerable interest.

The ESO archive provides a data cube derived from the merger of two MUSE pointings with an effective exposure time of 1685 s and a measured seeing at 5007 Å of $0\farcs80$ (ESO archive ID ADP.2019-10-05T19:19:48.724, PI: L. Hernandez-Garcia, Program ID: 0103.B-0837). As shown in Figure 5, the data span the galaxy's minor axis, and overlap in the area of its bright nucleus The diff image, shown in Figure 5 highlights the outflow, which is quite bright, even in the high-excitation line of [O III] λ5007.

Our initial examination of NGC 1052's MUSE data cube found 100 PN candidates, with the brightest 20 having photometric errors less than 0.05 mag. However, we rejected 13 of these candidates, as their spectra are inconsistent with that of an [O III]-bright PN (e.g., Herrmann et al. 2008; Kreckel et al. 2017). These are identified in Figure 5 with red circles. In addition, as the distribution of objects in Figure 5 demonstrates, PN detections in the galaxy's inner $11''$ are problematic, due to the extremely bright emission from the region's diffuse gas. The exclusion of this region removed one object from our sample, leaving 86 PNe suitable for analysis, and ∼50 in the critical top ∼1 mag of the PNLF.

One major challenge associated with measuring NGC 1052's PNLF is contamination by the galaxy's diffuse emission-line gas. As illustrated by the difference image of Figure 5, the DIG in NGC 1052 creates a bright, complex background that compromises the photometry of faint PNe, even in the high-excitation [O III] line. Fortunately, in most cases, the PN's radial velocity is different enough from that of the DIG that the two components can be deblended quite easily using the MUSE spectra (see Paper I). The exception is in the nuclear region of the galaxy, where the luminosity of the outflow overwhelms that of the point sources.

The importance of NGC 1052's DIG is illustrated in Figure 6. The bottom panel shows the galaxy's PNLF as measured using simple point-source photometry, where the background is estimated using an annulus surrounding each source. The top panel shows the PNLF where the contribution of the diffuse emission-line gas has been removed by carefully examining each object's spectrum and deblending the PN's [O III]

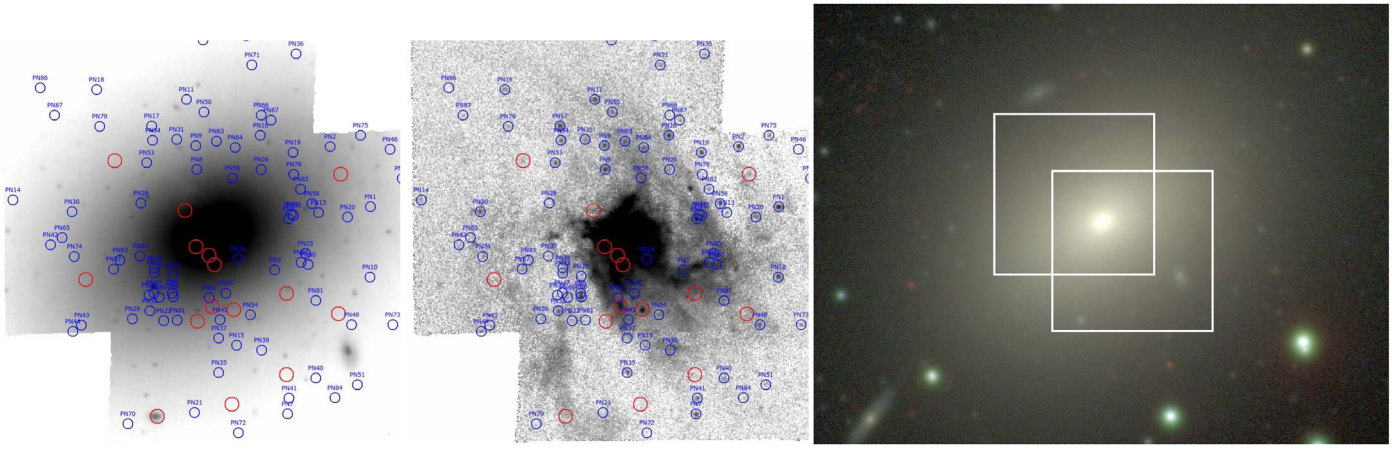

Figure 5. NGC 1052. Left: thumbnail off-band and difference images derived from the MUSE data cubes. Our PNe candidates are highlighted in blue, while emission-line interlopers are shown in red. Right: broadband image of the galaxy with a mosaic of the two MUSE pointings outlined in white. (Credit: Carnegie-Irvine Galaxy Survey (CGS).) A high-resolution image of the off-band and difference images is available online. The animation (available online) begins with the off-band image and then steps through the MUSE layers centered on the galaxy's redshifted [O III] wavelength to show how all emission-line objects, especially the PNe, rise and fall in brightness with wavelength.

(An animation of this figure is available.)

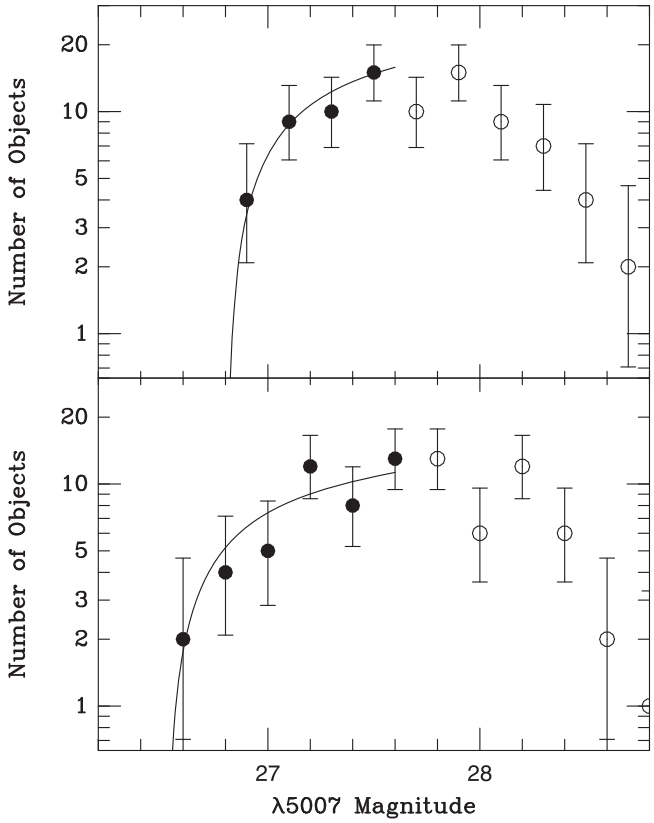

Figure 6. Top: the observed PNLF of NGC 1052 binned into 0.2 mag intervals, with error bars displaying 1σ confidence intervals (see Gehrels 1986). Open circles represent data beyond the completeness limit of the survey. The top panel shows the PNLF where the PN emission has been deblended from the DIG using the methods described in Paper I; the lower panel shows the same function when the sky estimates are based on simple aperture photometry. The curves show the best-fit PNLF: without deblending, the most likely apparent distance modulus is 0.25 mag smaller.

emission from that of the DIG using the methodology of Paper I. Clearly, the latter set of photometry is a better fit to Equation (2) and produces a distance that is ∼0.25 mag more distant. This highlights another advantage of MUSE PNLF measurements: narrowband photometry would have been unable to disentangle the two sources of [O III] emission.

To fit NGC 1052's PNLF, we determined the amount of galactic V-band light at every position in the MUSE data cube using the R-band surface photometry of Jedrzejewski et al. (1987) and an assumed color of $(V-R)=0.93$ (Persson et al. 1979). We find that, after excluding the central 11″ of the galaxy, roughly $V\sim 11.1$ of flux is contained within the two MUSE pointings. We then estimated the stellar velocity dispersion underlying each PN's position using the long-slit spectroscopy of Binney et al. (1990), and computed the most likely distance to the galaxy assuming a foreground extinction of $E(B-V)=0.023$ (Schlafly & Finkbeiner 2011). Our solution using these numbers is illustrated in Figure 7.

As shown in the figure, Equation (2) fits the observed PNLF extremely well, and there is no evidence of any overluminous objects. Our PNLF distance to NGC 1052 is $(m-M)_0 = 31.26^{+0.04}_{-0.07}$ ($17.9^{+0.3}_{-0.6}$ Mpc), where the uncertainties do not include the systematic error associated with MUSE's flux calibration and our photometric aperture correction. The former uncertainty is generally of the order of ∼3% (Weilbacher et al. 2020); to estimate the latter, we examined the photometry of the four, pointlike sources contained in the overlap region of the two NGC 1052 MUSE fields. These sources are relatively faint, with between 17,175 and 37,780 counts (in the units as explained in Appendix B), and the scatter of their inferred aperture corrections is $\sigma=0.075$ mag. If we use the standard deviation of the mean to define the expected error on the data cube's aperture correction, then this systematic component is ∼0.04 mag.

(We do note that the pointlike sources used to define the data cube's PSF are likely not Milky Way stars, but globular clusters belonging to NGC 1052. However, this should not affect our measurement of the aperture correction. If we scale M31's globular cluster system (Barmby & Huchra 2001) to the distance of NGC 1052, then a median globular cluster in the galaxy should have a half-light radius of only 0.″02, and the angular size of the M31's largest cluster would be $R_e\sim 0.''31$. This is much smaller than the 0.″80 seeing of the data cube.)

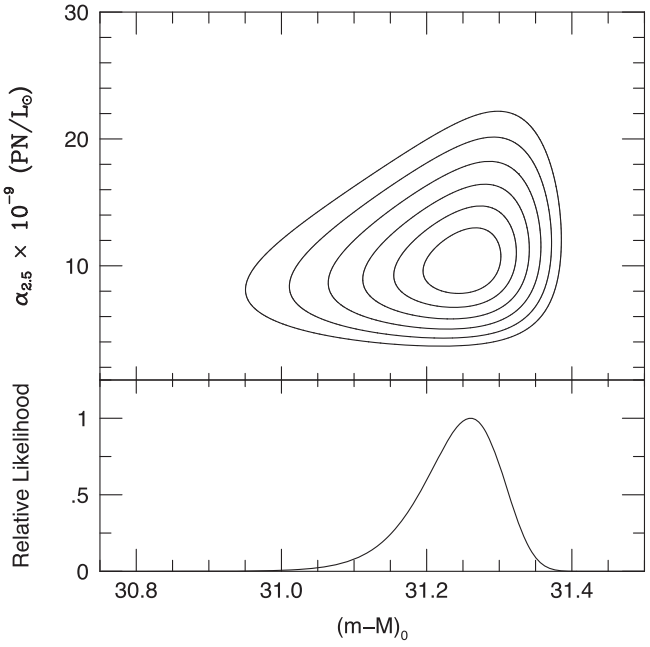

Figure 7. The results of the maximum-likelihood solution for NGC 1052's distance modulus. The top panel shows the likelihood contours (drawn at 0.5σ intervals), with the abscissa giving the galaxy's true distance modulus and the ordinate showing the number of PNe within 2.5 mag of M^*, normalized to the amount of bolometric light sampled. The lower panel marginalizes over the latter variable.

If we fold in the systematic errors associated with the MUSE flux zero-point, the data cube's aperture correction, and the likely error on the reddening, then our estimate for the galaxy's distance modulus becomes $(m - M)_0 = 31.26^{+0.07}_{-0.08}$ (for an M^* value of −4.54). This distance is essentially identical to that found from the Hubble Space Telescope (HST)/NICMOS measurement of the galaxy's near-IR SBFs ($(m - M)_0$=31.28 ± 0.27; Jensen et al. 2003). It is also consistent with the distances of the galaxy's two ultradiffuse satellite dwarfs, as inferred by first taking the ratio of their *I*-band SBFs to those of the dwarf galaxies of the M96 group, and then anchoring the zero-point to the megamaser distance of NGC 4258 (van Dokkum et al. 2018). Interestingly, direct TRGB measurements of these dwarfs give significantly larger values for the group's distance, with $(m - M)_0 = 31.72 \pm 0.12$ (Shen et al. 2021) and 31.50 ± 0.18 (Danieli et al. 2020). These distance moduli are excluded by our measurements. Finally, we note that Fensch et al. (2019) report the identification of three PNe in the dwarf NGC 1052-DF2. However, since none of these objects are likely to have magnitudes near the bright-end cutoff of the PNLF, their detection does not provide a useful constraint on the galaxy's distance.

5.3. NGC 1326 (Fornax Cluster Catalog 029)

NGC 1326, otherwise known as Fornax Cluster Catalog (FCC) galaxy 029 (Ferguson 1989), is a bright lenticular system (Hubble type (R1)SAB(r)0/a) with an outer ring of star formation (roughly 2′ from the nucleus) and an inner ring-like structure extending ∼9″ in diameter. Although the galaxy has Tully–Fisher measurements in the range of ∼13 to ∼19 Mpc (e.g., Bottinelli et al. 1984; Willick et al. 1997; Springob et al. 2009), the system's early Hubble type and moderately face-on ($i \approx 45°$) inclination calls those values into question. Nevertheless, the system's location in the core of the Fornax cluster, 3°.1 from the central cD galaxy NGC 1399, suggests that the Tully–Fisher estimates are reasonable. There are no Cepheid, TRGB, or SBF distances to the system.

We retrieved from the ESO archive a MUSE-DEEP data cube formed from the combination of two exposures (ESO Archive ID: ADP.2018-04-05T08:26:13.290, PI: M. Carollo, Program ID: 0100.B-0116). The effective exposure time for these data is 3354 s, and the seeing at 5007 Å is 1.″00. The footprint of the IFS is shown in Figure 8. The region encompasses the system's bright nuclear region and much of the galactic bar.

PN detections within the central 12″ of NGC 1326's nucleus are difficult, due to the region's high surface brightness and the copious amounts of diffuse [O III] emission. Thus, we confined our analysis to larger galactocentric radii, where we found 86 pointlike emission-line sources. Many of these objects, especially those close to the nucleus and along the galactic bar (the red circles in Figure 8), have the spectral signature of H II regions or SNRs and are excluded from our list of PN candidates. The final sample therefore consists of 55 objects; this PNLF is shown in Figure 9.

NGC 1326's PNLF is not very well defined. In part, this is because there is one PN candidate that is 0.31 mag more luminous than any other object. (Figure 9 shows the PNLF with the starting edge of the first bin chosen to minimize the discordant appearance of PN1.[6]) However, a more important factor is that, of the 40 PNe brighter than the nominal completeness limit of $m_{5007} = 27.8$, only ∼20 are in the magnitude range that defines the PNLF cutoff ($m \lesssim M^* + 1$).

There are several possible explanations for the overluminous nature of PN1. The first, and simplest, is that the apparent luminosity of the object (PN1) is simply due to poor photometry. As can be seen in the diff image in Figure 8, PN1 is located in a region of bright diffuse emission-line gas, adjacent to an interloping object (red circle). It is quite possible that the source's apparent high luminosity is due to imperfect background subtraction, in which case the object should be excluded from the analysis. Similarly, if the *overluminous* object is something other than a normal PN (such as a high-excitation, metal-poor H II region), it should also be eliminated from the data set. There is no evidence for this in the object's spectrum, but the interpretation cannot be completely excluded.

A third explanation is that there is nothing abnormal about the PN at all, and the 0.31 mag difference between it and the next brightest PNe is simply due to small number statistics. This seems unlikely, as that would imply that NGC 1326 is at least ∼4 Mpc closer than the main body of Fornax. But if the object is a normal PN, then it must be included in the fitting process. Similarly, it is possible that this bright [O III] source is actually formed from the combined flux of two normal PNe that are superposed upon each other. To wit, PN1 is located in a region of NGC 1326 with a *V*-band surface brightness of $\mu_V \sim 19.7$ mag arcsec^{-2} (Buta et al. 1998). According to Equation (3) of Chase et al. (2023), this means at the nominal Fornax distance of 19 Mpc, PN1 has a ∼20% chance of being a superposition of two objects in the top 2.5 mag of the PN luminosity function, and a ∼5% chance that both PNe are in the top 1 mag of the PNLF. If this hypothesis is correct, then, once again, the source must be included in the PNLF analysis.

[6] This choice in no way affects our PNLF distance estimates since our analysis does not use binned data. The histograms displayed in this paper were created solely for the purpose of visualization.

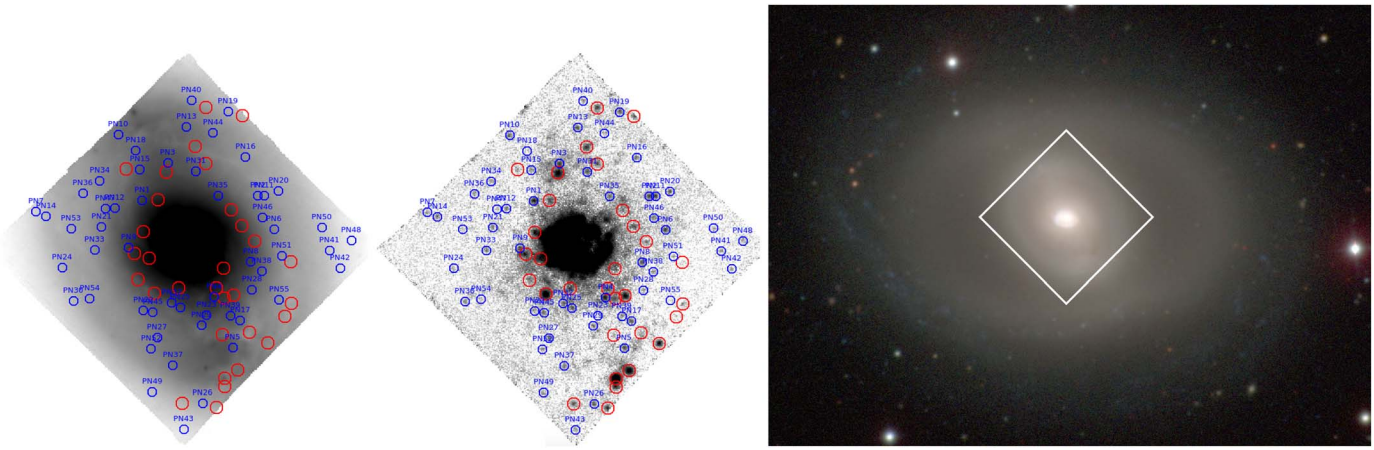

Figure 8. NGC 1326. Left: thumbnail off-band and difference images derived from the MUSE data cube. Our PNe candidates are highlighted in blue, while emission-line interlopers are shown in red. Right: a broadband image of the galaxy with the location of the MUSE field shown in white (Credit: CGS). A high-resolution image of the off-band and difference images is available online. The animation (available online) begins with the off-band image and then steps through the MUSE layers centered on the galaxy's redshifted [O III] wavelength to show how all emission-line objects, especially the PNe, rise and fall in brightness with wavelength.

(An animation of this figure is available.)

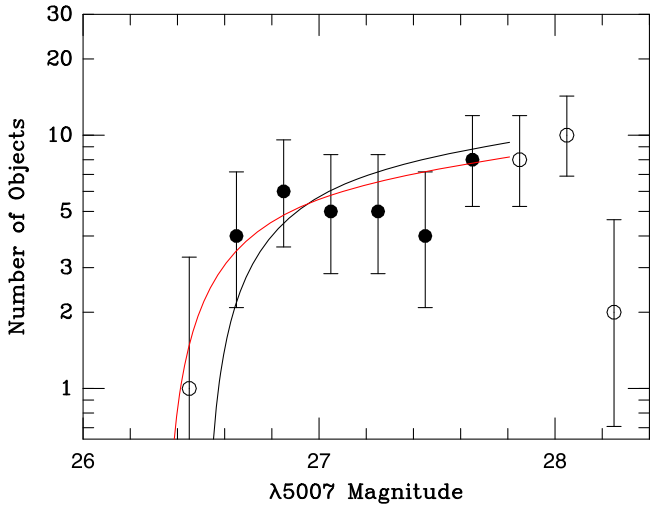

Figure 9. The observed PNLF of NGC 1326 binned into 0.2 mag intervals. The open circles beyond $m_{5007} \sim 27.8$ represent data beyond the completeness limit; the bright open circle shows PN1. The error bars represent each bin's 1σ confidence intervals (Gehrels 1986). The red curve illustrates the most likely fit to Equation (2) when PN1 is included in the sample; the black curve shows the fit when PN1 is excluded. The difference between the solutions is 0.17 mag.

Finally, it is possible that PN1 is a normal PN, but that our knowledge of the true shape of the PNLF is incomplete. Equation (2) was originally defined to fit the magnitude distribution of a statistically complete sample of ~120 PNe in the bulge and inner disk of M31 (Ciardullo et al. 1989). In such a finite data set (with only ~32 objects in the top ~1 mag of the luminosity function), extremely rare, short-lived objects may not be present. Indeed, although [O III] PNLFs now exist for dozens of galaxies, the PN samples are rarely large enough to exclude the possible existence of a very low-amplitude, bright-end tail to the luminosity function. If such a tail does exist, any attempt to fit PN1 with the expression given by Equation (2) will result in a systematic underestimate of the galaxy's distance. We will discuss the true shape of the empirical PNLF in Section 6.3.

We fit the PNLF of NGC 1326, with and without PN1, using the photometric measurements of Buta et al. (1998) to determine the galaxy surface brightness underlying each PN candidate. These data imply that the total amount of V-band light contained within the MUSE data cube is $V \sim 11.5$. However, we made no attempt to model the behavior of the stellar velocity dispersion in the MUSE field: since the spectroscopy of Dalle Ore et al. (1991) and Gadotti & de Souza (2005) both indicate that the line-of-sight velocity dispersion is much less than the velocity resolution of the MUSE spectrograph, we set $\sigma = 100$ km s^{-1} throughout the survey region. Finally, we assume $E(B-V) = 0.016$ as the foreground extinction to the galaxy (Schlafly & Finkbeiner 2011).

Figure 10 shows the results of our fits. As expected, the galaxy's distance is not well defined: 23 objects spread out over the top ~1 mag of the PNLF is insufficient for defining the precise location of the PNLF cutoff. As a result, whether or not one includes PN1 in the sample does not substantially change the quality of the fit. If PN1 is treated as a normal PN, then the galaxy is forced to a distance that is ~4 Mpc smaller than the canonical distance to Fornax, i.e., to $14.6^{+0.4}_{-0.7}$ Mpc. This result is unaffected by the inclusion of superpositions in the analysis: although it is possible that the object is a superposition of two sources, the likelihood that two PNe in sum would produce an [O III] source ~0.3 mag brighter than the next most luminous object is quite low and barely registers in the contour plot.

The exclusion of PN1 from consideration produces a fit that is only slightly better than that which includes the PN. (Without PN1, the K-S statistic for a comparison of the data with the model is $D_n = 0.162$, for a p-value of $p = 0.77$; with PN1, D_n=0.174, and $p = 0.83$.) Yet without PN1, the galaxy's most likely distance modulus is $\Delta\mu = 0.19$ mag greater, $(m - M)_0 = 31.00^{+0.06}_{-0.11}$, or $d = 15.9^{+0.5}_{-0.8}$ Mpc.

The uncertainties quoted above do not include the systematic errors associated with the reddening, MUSE flux calibration, data cube aperture correction, or limitations in the reference PNLF. In particular, although the aperture correction error obtained from the field's brightest pointlike source has a calculated uncertainty of only 0.028 mag, the standard deviation about the mean aperture correction for the three brightest PSF objects is 0.085 mag, implying an 0.05 mag error of the mean. This uncertainty, along with those for the MUSE flux calibration and foreground reddening, results in a distance

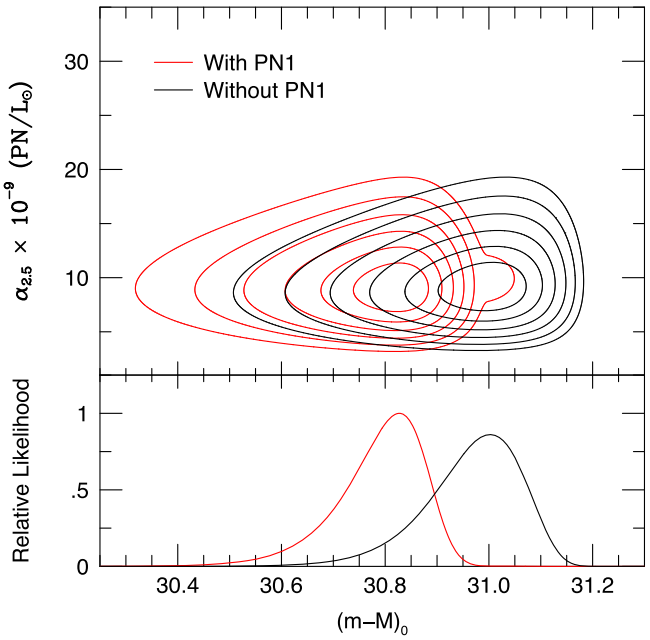

Figure 10. The top panel shows the results of the maximum-likelihood analysis for NGC 1326. The abscissa is the galaxy's true distance modulus, the ordinate is $\alpha_{2.5}$, the number of PNe within 2.5 mag of M^*, normalized to the amount of bolometric light sampled. The red contours, shown at 0.5σ intervals, illustrate the likelihoods when PN1 is included in the sample; the likelihood that PN1 is a superposition of two bright [O III] sources is reflected in the distorted probability contours at the $\sim 3\sigma$ level. The black contours display the same information when PN1 is excluded. The bottom panel marginalizes these data over $\alpha_{2.5}$.

modulus of $31.00^{+0.09}_{-0.13}$, or $d = 15.9^{+0.6}_{-0.9}$ Mpc. This number is still significantly smaller than the distance to Fornax, and suggests that the system may be foreground to the cluster's core.

5.4. NGC 1351 (FCC 083)

NGC 1351 (FCC 083) is another moderately bright Fornax lenticular (classification SAOp) that has two pointings in the ESO archive (ESO Archive IDs: ADP.2017-12-12T15:38:27.863 and ADP.2017-07-19T15:12:54.145, PI: M. Sarzi, Program ID: 296.B-5054). The first pointing, P1, is centered on the nucleus and has a nominal seeing at 5007 Å of 0.″88 and an exposure time of 3379 s; the second, P2, overlaps P1, as it is centered $\sim$35″ northwest of the nucleus along the galaxy's major axis. The latter data cube has a somewhat longer exposure (4680 s) and slightly worse (1.″11) image quality.

Our examination of the central pointing of NGC 1351 found 92 PN candidates, of which six were later rejected as interlopers based on their spectra. P2 had far fewer objects, as it sampled less light with poorer image quality: this pointing only added 16 PNe to the sample. In total, we detected 102 PNe in NGC 1351, with more than 30 objects in the top $\sim$1 mag of the luminosity function.

The observed PNLF is shown in Figure 12. The displayed data points exclude two objects (PN8 and 32) located within 10″ of the nucleus, as, in this region, the galaxy's bright background severely limits PN detections. But the remaining objects outline a fairly normal PNLF. In fact, the overall distribution is quite similar to that of NGC 1326, though with a greater population of PNe in the top $\sim$1 mag of the luminosity function. Like NGC 1326, NGC 1351's PNLF contains one object whose spectrum is fully consistent with that of normal PNe, but whose luminosity is 0.2 mag brighter than expected from Equation (2). Again, there are three explanations for the object.

The first is that the apparent luminosity of PN1 may be due to poor photometry. PN1's [O III] flux is partially blended with that of PN16, which is projected less than 1″ away (see Figure 13). Since the radial velocities of the two objects are similar, imperfect deblending of their PSFs could result in PN1 appearing overluminous. The second is that the object is some form of PN (or PN mimic) that does not obey the luminosity function defined by Equation (2). This possibility will be addressed further in Section 6.2. Finally, the object may be an otherwise normal PN that is superposed on another object. The background upon which PN1 is projected is not particularly bright ($\mu_V \sim 23.4$ mag arcsec^{-2}), but the possibility cannot be entirely discounted. Thus, we are left with the same ambiguity seen in NGC 1326, with one object having an outsized influence on the galaxy's derived distance. The difference between the two galaxies is that the larger number of PNe present in NGC 1351 makes the anomalous luminosity of PN1 more obvious. Consequently, if one assumes that PN1 is not an unlucky superposition of two sources, a K-S test can exclude its membership in the distribution defined by Equation (2) with greater than 93% confidence.

The situation is summarized in Figure 14, which shows the results of fitting Equation (2) to the data with and without the brightest PNe. For the analysis, we calculated the likelihood of unresolved PN superpositions using the B-band galaxy surface photometry of de Carvalho et al. (1991), a mean color of $(B-V) = 0.90$ (Faber et al. 1989) and the velocity dispersion data of D'Onofrio et al. (1995).[7] From the figure, it is clear that the calculated distance to the galaxy depends on whether PN1's photometry is accurate and whether it is, indeed, a normal PN, rather than some exotic object.

If PN1 is treated as a normal PN, then the galaxy's inferred distance modulus is $(m-M)_0 = 31.23^{+0.04}_{-0.07}$ ($17.7^{+0.3}_{-0.6}$ Mpc) for $E(B-V) = 0.011$. This is a formal solution only: as stated above, a K-S test excludes the null hypothesis that the observed set of PNe is drawn from the distribution defined by Equation (2). On the other hand, if the object is excluded from the sample, the galaxy's distance modulus increases to $(m-M)_0 = 31.39^{+0.04}_{-0.08}$ ($19.0^{+0.4}_{-0.7}$ Mpc), and the quality of the fit is much improved. Consequently, we adopt this larger distance in our analysis.

For NGC 1351, the aperture correction measurements are quite good, and the total systematic error, due to uncertainties in the MUSE flux calibration, the data cubes' aperture corrections, and foreground extinction, is $\sim$0.06 mag. This increases the error bars slightly so that the distance modulus to the galaxy becomes $(m-M)_0 = 31.39^{+0.05}_{-0.10}$, or $19.0^{+0.7}_{-0.9}$ Mpc. This value is nearly identical to the z_{850}-band SBF distance of 31.42 ± 0.07 (19.2 ± 0.6 Mpc) (Blakeslee et al. 2009).

One other feature of Figure 12 is worth noting. The number of PNe observed, normalized to the total amount of galaxy light contained in the MUSE data cubes (found using the surface photometry of de Carvalho et al. 1991), is higher than that

[7] The latter required some extrapolation, as the data extend only $\sim$20″ from the nucleus and are restricted to the galaxy's major axis. However, in the regions of our survey, the galaxy's stellar motions ($\sigma \lesssim 100$ km s^{-1}) are much less than the $\Delta v = 200$ km s^{-1} resolvable by MUSE. Thus, the exact form of our extrapolation is unimportant.

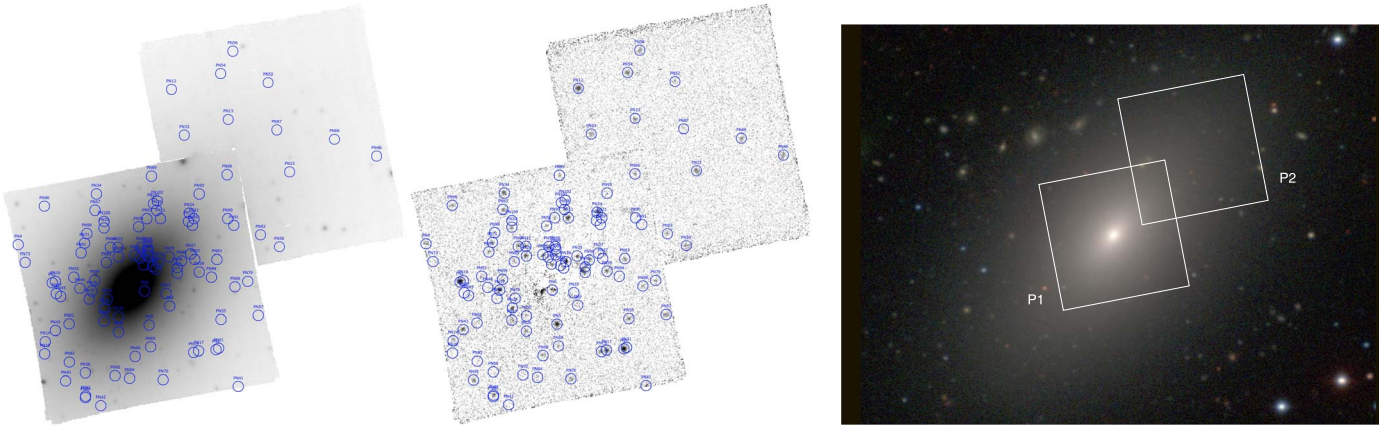

Figure 11. NGC 1351. Left: thumbnail off-band and difference images derived from MUSE data cubes of the galaxy. Our PNe candidates are circled in blue. Right: a broadband image with the MUSE fields outlined in white. (Credit: CGS). A high-resolution image of the off-band and difference images is available online. The animation (available online) begins with the off-band image and then steps through the MUSE layers centered on the galaxy's redshifted [O III] wavelength to show how all emission-line objects, especially the PNe, rise and fall in brightness with wavelength.

(An animation of this figure is available.)

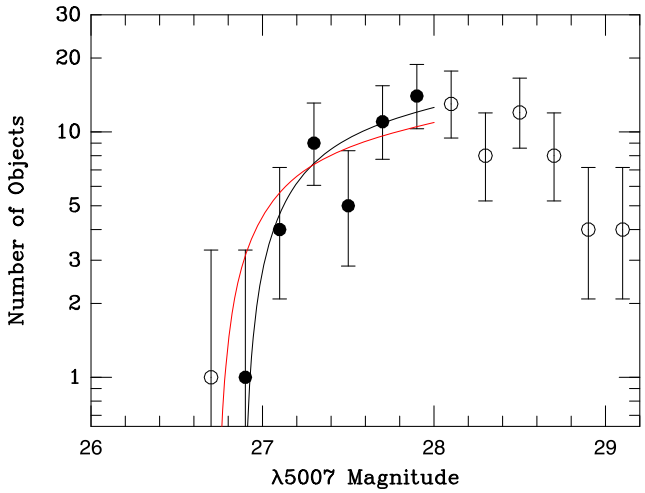

Figure 12. The observed PNLF of NGC 1351 binned into 0.2 mag intervals. The open circles beyond $m_{5007} \gtrsim 28.0$ show data beyond the completeness limit; the open circle at $m_{5007} \sim 26.8$ represents PN1, an object that is 0.2 mag more luminous than the next brightest source. The error bars illustrate 1σ confidence intervals (see Gehrels 1986). The red curve illustrates the most likely fit to Equation (2) when PN1 is included in the sample; the black curve shows the fit when PN1 is excluded. The difference between the values is 0.16 mag. A K-S test excludes PN1 from the sample with 93% confidence.

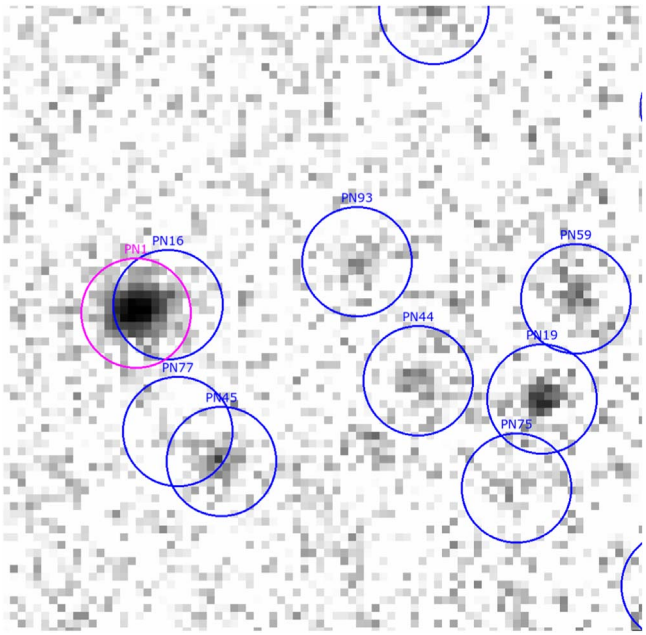

Figure 13. A small region of the MUSE data cube for NGC 1351, showing one wavelength slice centered on [O III] λ5007 at the redshift of the galaxy. Note that PN1 is blended with PN16. The overluminous nature of PN1 may be due to an imperfect deblending of the two sources.

expected for early-type galaxies. This anomaly does not substantially affect the implied distance modulus to the galaxy, since the methodology of Chase et al. (2023) only requires knowledge of the relative amount of light at each position in the MUSE data cube. But it suggests that there is either a zero-point issue associated with the galactic surface photometry or that the stellar population of NGC 1351 is a bit younger than that of most lenticular systems.

5.5. NGC 1366

NGC 1366 is an edge-on S0 galaxy in the Fornax cluster with an absolute magnitude of $M_I = -19.78$ and evidence of a counterrotating core (Morelli et al. 2017). The ESO archive contains a single deep data cube of the galaxy (ESO Archive ID: ADP.2019-10-10T08:04:58.194, PI: L. Morelli, Program ID: 0103.B-0331) with an effective exposure time of 2446 s and an image quality of 1.″12 at 5007 Å.

Our DELF procedure reveals a large amount of high-excitation ([O III] λ5007) line emission in the galaxy's inner $\sim$15″. As can be seen in the diff image in Figure 15, this light has the appearance of a spiral feature that is oriented *perpendicular* to the plane of the disk. Given the velocity structure of this gas (Morelli et al. 2017), it is hard to imagine that this morphology is the result of an outflow similar to that seen in NGC 1052 (Section 5.2). However, the feature does resemble those seen in Illustris TNG100 cosmological simulations of galaxies with counterrotating cores and infalling gas (Khoperskov et al. 2021). Given that NGC 1366 is known to have counterrotation, the models seem to be a plausible explanation for the appearance of the gas.

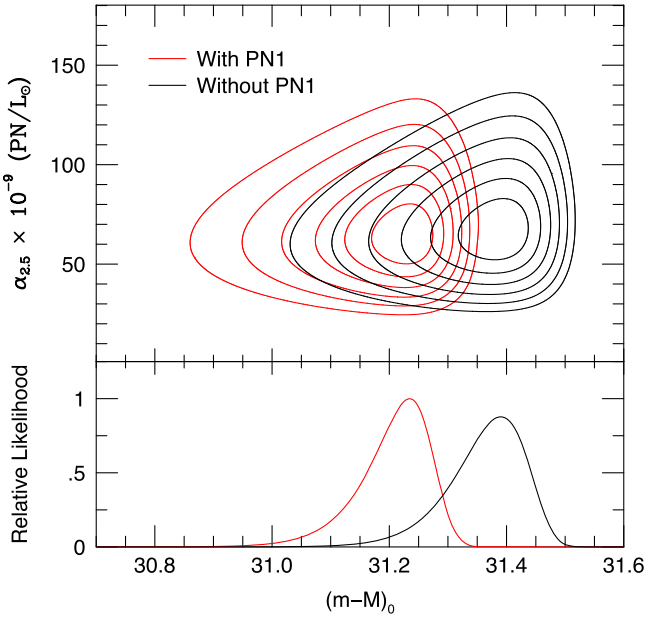

Figure 14. The top panel shows the results of the maximum-likelihood analysis for NGC 1351. The abscissa is the galaxy's true distance modulus; the ordinate is $\alpha_{2.5}$, the number of PNe within 2.5 mag of M^*, normalized to the amount of bolometric light sampled. The red contours, shown at 0.5σ intervals, illustrate the likelihoods when PN1 is included in the sample; the black contours display the same information when PN1 is excluded. The bottom panel marginalizes these data over $\alpha_{2.5}$.

Figure 15 also identifies a number of pointlike [O III] sources superposed on the diffuse emission. Owing to the modest luminosity of the host galaxy and the data cube's poor image quality, we initially detected a set of only 31 PN candidates. Upon further inspection of the spectra, this number was pared down by 12, leaving just 19 objects in our PN sample, and only 13 in the brightest $\sim$1 mag of the luminosity function.

Figure 16 shows the cumulative distribution of PN magnitudes in NGC 1366. Clearly, the distribution is in good agreement with the empirical law of Equation (2). But it is also clear that with only 18 objects in the statistically complete sample, and just 13 in the critical top magnitude of the luminosity function, the exact location of the PNLF cutoff is poorly defined.

We analyzed the galaxy's PNLF using the R-band surface photometry of Morelli et al. (2008) with an assumed $(V-R)$ color of 0.55 (Prugniel & Heraudeau 1998). These data imply that, outside the galaxy's central 10″, where no PNe are detected, the MUSE data cube surveys $V\sim 12.5$ of galaxy light. We also assumed a line-of-sight stellar velocity dispersion of 100 km s^{-1} throughout the region of PN detections; this is consistent with the spectroscopy of Morelli et al. (2017). The results of our analysis are displayed in Figure 17.

With a reddening of $E(B-V)=0.014$, the formal PNLF fit for NGC 1366 gives $(m-M)_0 = 31.39^{+0.10}_{-0.22}$; if we assume that flux calibration, aperture correction, and reddening contribute an additional $\sim$0.06 mag to the error budget, the final distance modulus becomes $(m-M)_0 = 31.39^{+0.11}_{-0.23}$, or $19.0^{+1.0}_{-1.8}$ Mpc. This value is consistent with Fornax cluster membership and is in accord with the I-band SBF distance modulus of $(m-M)_0$=31.62 $\pm$ 0.29 found by Tonry et al. (2001). We note that the value for the PNe per unit luminosity value is slightly low for a galaxy of this type. However, given the small number of PNe detected and the possibility that we are losing objects due to the bright, high-excitation line emission in the galaxy's core, the estimate of α is reasonable.

5.6. NGC 1385

NGC 1385 is an Eridanus cluster barred spiral galaxy (Hubble type SB(s)cd) with publicly available data products in the ESO Archive from the PHANGS-MUSE survey (Emsellem et al. 2022, PI: E. Schinnerer, Program ID: 1100. B-0651). The galaxy is particularly interesting for a distance scale study since it has no TRGB, SBF, or Cepheid measurements, and its Tully–Fisher distances extend over a very wide range, from $\sim$8 Mpc (e.g., Bottinelli et al. 1986; Sorce et al. 2014) to $\sim$50 Mpc (Bottinelli et al. 1984). Figure 18 shows the five pointings in the MUSE archive, which cover most of the galaxy's light. These pointings, along with their exposure times and seeing at 5007 Å, are listed in Table 4.

We note that P1, P4, and P5 were observed twice; however, the combined data cubes are not available in the ESO archive. In addition, the archive also contains two mosaicked data cubes (ESO Archive IDs: ADP.2021-07-16T10:20:56.387, ADP.2021-07-16T10:20:56.381). The cube that we label as A1 was created by merging all of the individual data sets into one cube, including the fields with two visits. The second data cube, A2, also combines all the data, but only after convolving each individual cube to a common PSF with a 0.″77 FWHM. This process is described in Emsellem et al. (2022).

To identify the galaxy's PN candidates, we first examined the individual data cubes (P1–P5), and one by one, found and measured 24, 23, 16, 4, and 19 PN candidates, respectively. We then repeated the photometry in mosaic A2, which has greater depth in the regions P1, P4, and P5, due to the fields' second observation. The improved signal-to-noise ratio (S/N) allowed us to exclude eight of our initial PN candidates as interlopers. Our final sample of candidates therefore contains 78 objects, with 54 being in the top $\sim$1 mag of the luminosity function.

The positions of these PNe are shown in Figure 18. From the figure, it is clear that PN detections within $\sim$30″ of the nucleus and along the galaxy's bright northern arm are severely compromised by the galaxy's high surface brightness and bright line emission. We exclude these regions from our analysis and thus eliminate one additional object (PN9) from our sample.

Figure 19 shows the luminosity function of the remaining PN candidates. Despite all the active star formation and dust present in the galaxy, the bright end of NGC 1385's PNLF is extremely well fit by the empirical law. This is in agreement with expectations: because the scale height of PNe should be larger than that of the galactic extinction, the bright end of the PNLF in large, moderately face-on galaxies should be dominated by objects on the nearside of the galaxy, above the dust layer (Feldmeier et al. 1997; Rekola et al. 2005). There is also no evidence of any overluminous PNe in the system.

Since there are no surface photometry measurements over the face of NGC 1385, we estimated the amount of light underlying each PN and in the entire MUSE data cube using continuum measurements made directly from the MUSE spectra. Also, since NGC 1385 is a disk galaxy seen relatively face-on (inclination angle of $\sim$44°), the line-of-sight velocity dispersion of its stars should be much less than the galaxy's $\sim$136 km s^{-1} rotation speed (Lang et al. 2020). Thus, we can

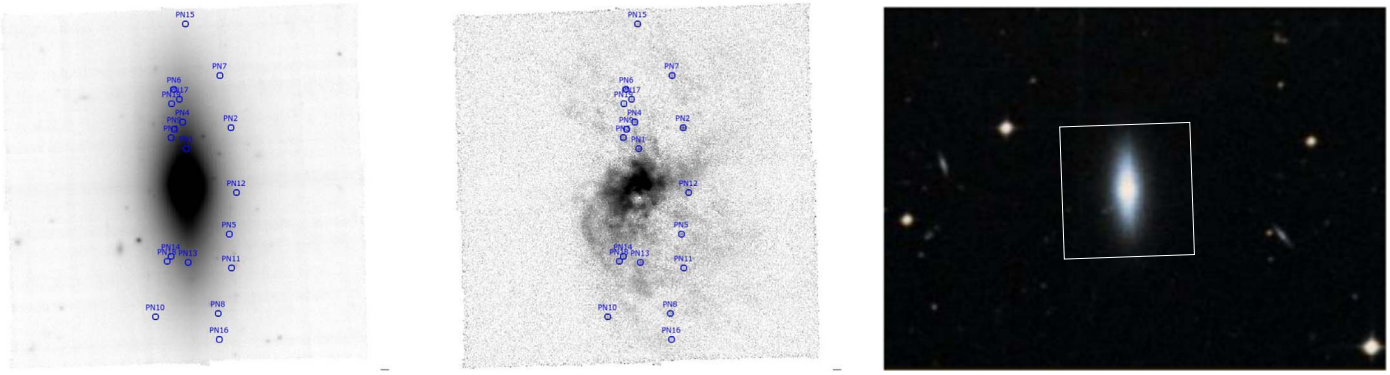

Figure 15. NGC 1366. Left: thumbnail off-band and difference images derived from the MUSE data cube. The PN candidates are circled in blue. Right: a broadband image with the MUSE field outlined in white. (Credit: ESO Digital Sky Survey (DSS)). A high-resolution image of the off-band and difference images is available online. The animation (available online) begins with the off-band image and then steps through the MUSE layers centered on the galaxy's redshifted [O III] wavelength to show how all emission-line objects, especially the PNe, rise and fall in brightness with wavelength.

(An animation of this figure is available.)

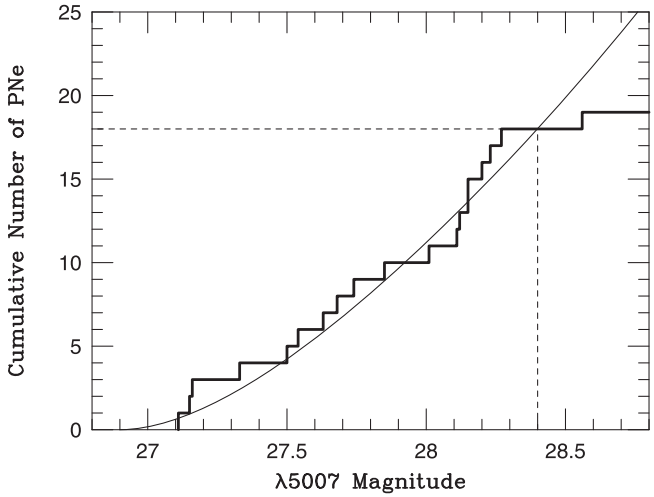

Figure 16. The cumulative luminosity function for PNe in NGC 1366. The dark line represents the observed data; the curve is Equation (2) shifted to the most likely apparent distance modulus of $(m - M)_0 = 31.39$. The dashed line shows the location where the incompleteness begins to affect the PN detections. Data brighter than this are consistent with being drawn from the empirical function.

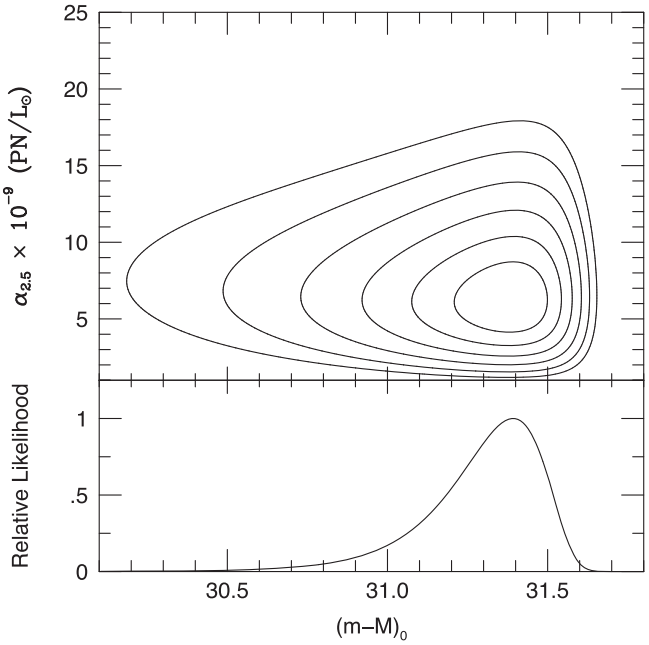

Figure 17. The top panel shows the results of the maximum-likelihood analysis for NGC 1366. The abscissa is the galaxy's true distance modulus, the ordinate is $\alpha_{2.5}$, the number of PNe within 2.5 mag of M^*, normalized to the amount of bolometric light sampled. The contours are drawn at 0.5σ levels. The bottom panel marginalizes these data over the PN per luminosity variable.

expect superposed PNe to be unresolved, and adopt $\sim$50 km s^{-1} as a typical value for the system's line-of-sight velocity dispersion.

Figure 20 shows the result of fitting the observed PNLF to Equation (2). For a Milky Way foreground extinction of $E(B-V) = 0.017$ (Schlafly & Finkbeiner 2011), the fitted distance to NGC 1385 is $(m - M)_0 = 31.99^{+0.06}_{-0.08}$.

Unfortunately, obtaining the true error bars for the NGC 1385's distance is difficult. Pointings P2 and P5 have reasonably bright point sources in the field, and estimates for their aperture corrections are consistent to within 0.03 and 0.04 mag, respectively. However, in fields P1, P2, and P5, the PSF star photometry displayed large uncertainties with formal errors on the aperture corrections as large as 0.25 mag. It is highly unlikely that the true errors are as large as this since the effect would blur out the PNLF cutoff and create a luminosity function that is a poor match for Equation (2) (see Section 5.10). Conservatively, we adopt $\sim$0.1 as the total systematic error associated with our distance measurement. NGC 1385's distance is then $(m - M)_0 = 31.99^{+0.11}_{-0.12}$, or $25.0^{+1.4}_{-1.5}$ Mpc. This places the galaxy well beyond the core of the Fornax cluster and in the mid-range of the Tully–Fisher estimates.

We note that NGC 1385 was included in the recent PNLF study by Scheuermann et al. (2022) that is based on the same data set that we have used. Their analysis resulted in a significantly shorter distance, with $(m - M)_0 = 29.96^{+0.14}_{-0.32}$, or only $9.8^{+0.6}_{-1.5}$ Mpc. Interestingly, the authors caution that their derived distance modulus was subject to a large uncertainty and should be considered an upper limit to the galaxy's true distance. Specifically, they reported only 11 PNe brighter than their completeness limit of $m_{\rm lim} = 28$, with the most luminous PN being brighter than $m_{5007} = 26$. This is not supported by our measurements, as our brightest PN has $m_{5007} = 27.55$.

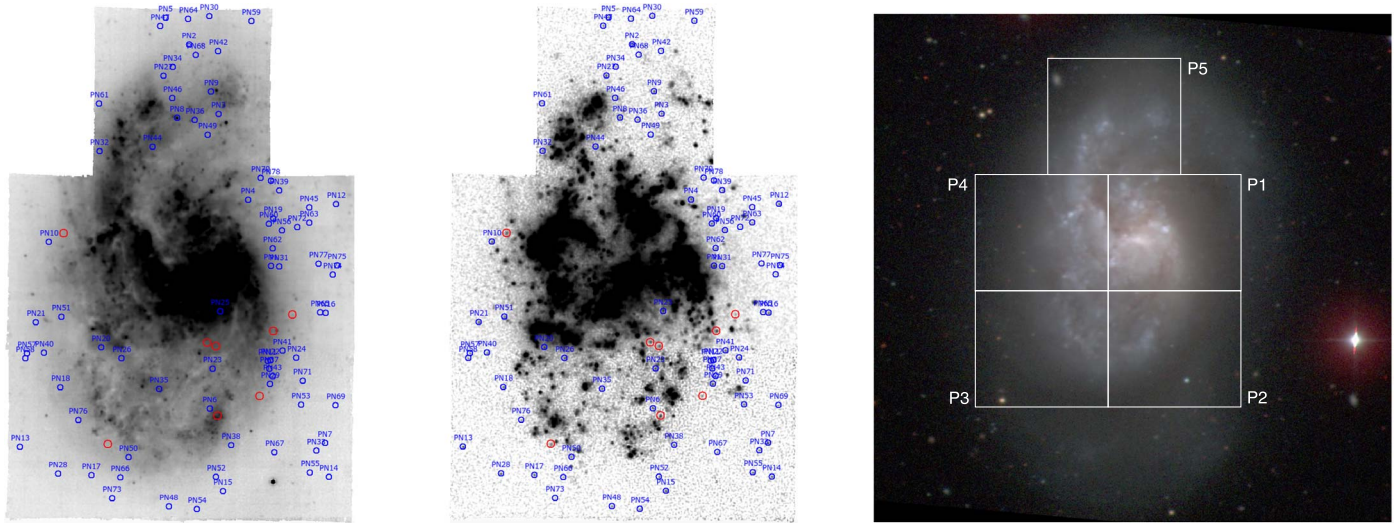

Figure 18. NGC 1385. Left: thumbnail images of an off-band and difference image derived from the MUSE data cubes. Left: thumbnail off-band and difference images derived from five MUSE data cubes. Our PNe candidates are highlighted in blue, while emission-line interlopers are shown in red. Right: a broadband image outlining the MUSE fields. (Credit: CGS). A high-resolution image of the off-band and difference images is available online. The animation (available online) begins with the off-band image and then steps through the MUSE layers centered on the galaxy's redshifted [O III] wavelength to show how all emission-line objects, especially the PNe, rise and fall in brightness with wavelength.

(An animation of this figure is available.)

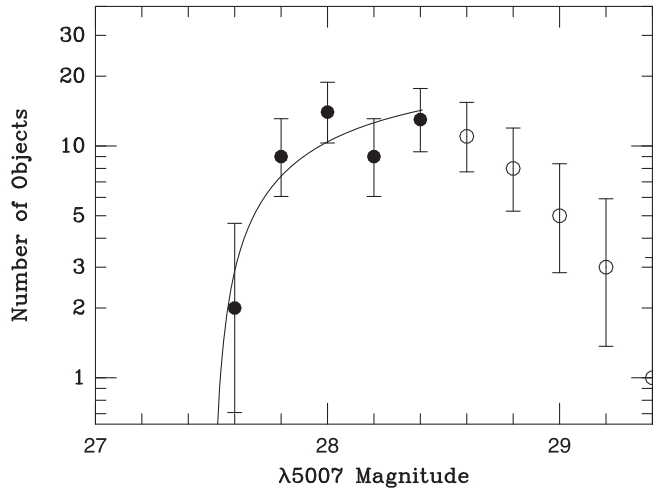

Figure 19. The observed PNLF of NGC 1385 binned into 0.2 mag intervals. The error bars represent 1σ confidence intervals (see Gehrels 1986); the open circles show data beyond the completeness limit. The black curve illustrates the most likely fit to Equation (2).

Table 4
Data Cubes for NGC 1385

Field	Archive ID	Exp Time (s)	Seeing (5007 Å)
P1	ADP.2020-01-11T01:24:00.728	2420	0.″64
P2	ADP.2021-01-29T13:19:05.970	2420	0.″77
P3	ADP.2020-01-28T16:14:42.084	2420	0.″82
P4	ADP.2019-02-13T01:31:18.894	2420	0.″71
P5	ADP.2020-01-27T19:05:08.471	2420	0.″64

Also, the number of PNe contributing to our fit is almost 5 times larger than theirs.

Since the agreement of our PNLF distances for other galaxies in the Scheuermann et al. (2022) sample is quite good,

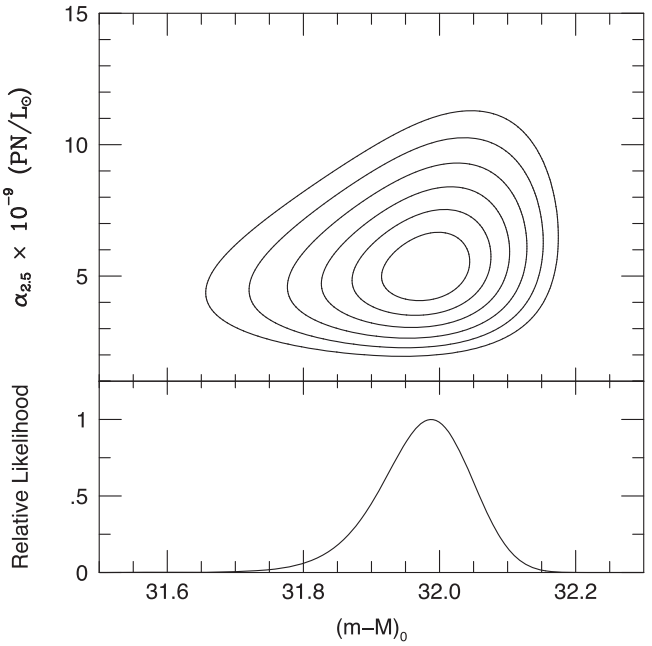

Figure 20. The top panel shows the results of the maximum-likelihood analysis for NGC 1385. The contours are drawn at 0.5σ intervals. The abscissa is the galaxy's true distance modulus; the ordinate is the number of PNe within 2.5 mag of M^*, normalized to the amount of bolometric light sampled. The bottom panel marginalizes over the latter variable.

we have looked into the possible causes of the discrepancy. A detailed account of the comparison is given in Appendix A. In summary, we note the following:

(1) Our sample of 77 [O III] sources with spectra consistent with that of a PN extends ∼0.4 mag deeper than the Scheuermann et al. (2022) data set. This is readily understood from the superior capabilities of the DELF extraction, which typically yields a factor of ∼2 improvement in S/N over other techniques (see

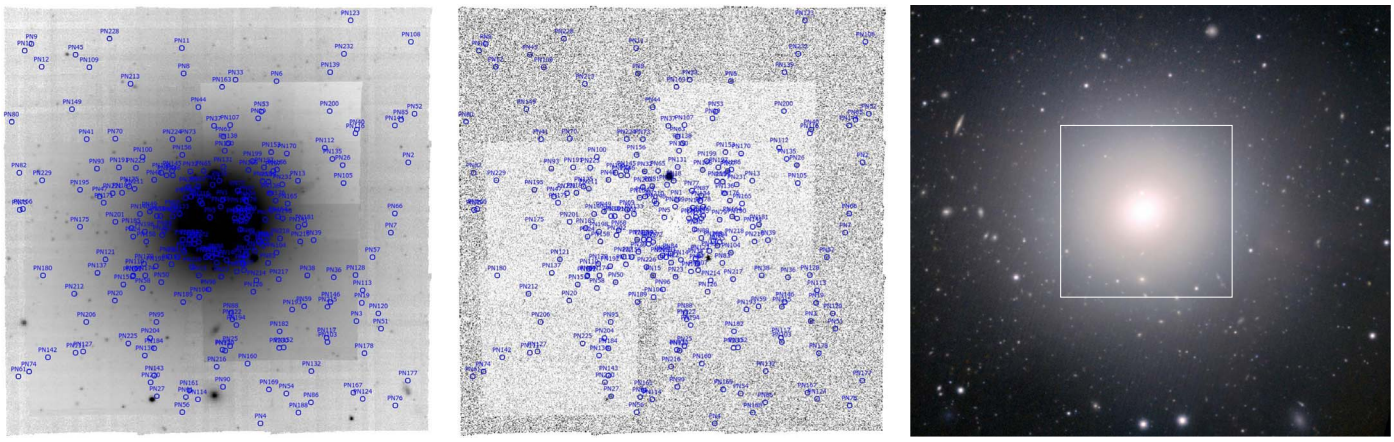

Figure 21. NGC 1399. Left: thumbnail difference and off-band images derived from the MUSE data cube. Our PN candidates are circled in blue. Right: a broadband image with the region of the data cube shown in white. (Credit: ESO). A high-resolution image of the off-band and difference images is available online. The animation (available online) begins with the off-band image and then steps through the MUSE layers centered on the galaxy's redshifted [O III] wavelength to show how all emission-line objects, especially the PNe, rise and fall in brightness with wavelength.

(An animation of this figure is available.)

Paper I). From their list of 11 candidates, only two are confirmed by our analysis.

(2) The majority of the Scheuermann et al. (2022) PN candidates are located within giant H II region complexes. This is problematic due to issues associated with background subtraction. With the exception of the two PNe mentioned above, we classify all these objects as H II regions or SNRs. This explains why two-thirds of their objects have measured magnitudes brighter than our PNLF cutoff. Due to the difficulty of distinguishing H II regions from PNe, our survey largely avoided those regions of the galaxy with the highest star formation rates.

(3) The short distance of 9.8 Mpc is not compatible with the SBF distances of other Fornax/Eridanus group galaxies (see Appendix A, Table 12). In fact, the system's radial velocity and our PNLF distance place NGC 1385 near the center of the Eridanus cloud (Willmer et al. 1989).

(4) The brightest object in the Scheuermann et al. (2022) sample is 1.83 mag more luminous than the brightest PN in our sample. Following the analysis of Soemitro et al. (2023), who examined the PNLF for NGC 300, another disk galaxy with active star formation, if the galaxy is at the distance of Eridanus, then their PN1 would need to be excited by a central star with a luminosity of at least $\log L/L_{\odot} = 4.48$. This is much brighter than the post-AGB evolutionary track of any PN central star (Gesicki et al. 2018).

5.7. NGC 1399 (FCC 213)

NGC 1399, the central cD/giant elliptical galaxy of the Fornax cluster, has been surveyed for PNe as far back as the early 1990s (McMillan et al. 1993; Arnaboldi et al. 1994). Two different MUSE programs have observed the galaxy (ESO Archive ID: ADP.2017-03-27T13:16:27.827, PIs: J. Walcher and S. Zieleniewski, Program IDs: 094.B-0903 and 094.B-0298) and these data have been combined into one large (3.′92 FoV) data cube with a quoted effective integration time of 954 s and an image quality of 0.″81. In fact, according to the ESO archive provenance chain, this is a full-sized mosaic with 295 s exposure times everywhere, plus five 900 s exposures on the central regions that provide field overlap. This coaddition was not seamless: as the processed *off* and *diff* images of Figure 21 show the data suffer from imperfect flat-field corrections and different levels of noise. Nevertheless, our DELF technique allowed us to identify 232 PN candidates over the body of the galaxy.

Surface photometry of NGC 1399 exists from a number of studies (e.g., Franx et al. 1989; Caon et al. 1994; Iodice et al. 2016), and we used these data to determine the amount of *V*-band galactic light at every position in the MUSE data cube. For estimating the line-of-sight velocity dispersion at the position of each PN, we used the spectroscopy of Saglia et al. (2000), who obtained major and minor axis kinematic data over all but the outermost regions of the MUSE survey.

A comparison of the distribution of MUSE PNe and that of the galaxy's light reveals that we are likely missing PNe within 15″ of the galaxy's nucleus. This is not unexpected as the exposure times for this galaxy are relatively short. Consequently, the region's steep surface brightness gradient causes the limiting magnitude for PN detections to change rapidly with position. While we could perform artificial star experiments to model and incorporate the effect into our analysis, it is simpler to just exclude the entire region from our study. This reduces the PNe sample by less than 10% and still leaves over 100 PNe, covering $V \sim 10.3$ mag of galaxy light, in the brightest ∼1 mag of the luminosity function.

Figure 22 shows the observed PNLF of the galaxy. Since the bright end of the function is so well populated, the shape of the PNLF is exquisitely defined. Moreover, despite the large number of PNe, there is no evidence of any overluminous objects. The lack of such objects can be partially explained by the galaxy's mass. NGC 1399 is a central cD galaxy whose line-of-sight velocity dispersion ranges from $\sim$370 km s^{-1} near the nucleus to $\sim$250 km s^{-1} in the outer regions surveyed by MUSE. Consequently, even when two PNe fall onto the same spatial element, there is a good chance that their fluxes can be disentangled via the objects' discordant radial velocities. Overluminous objects caused by PN superpositions should therefore be less common in such an environment, and

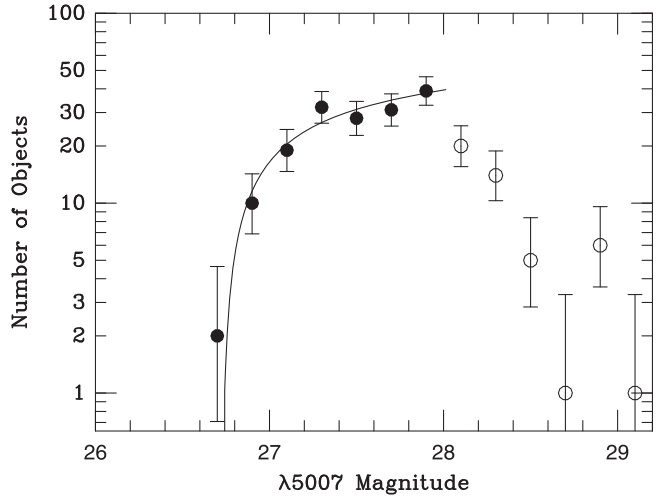

Figure 22. The observed PNLF of NGC 1399 binned into 0.2 mag intervals. The open circles show data beyond the completeness limit; the error bars represent 1σ confidence intervals (see Gehrels 1986). The black curve illustrates the most likely fit to Equation (2).

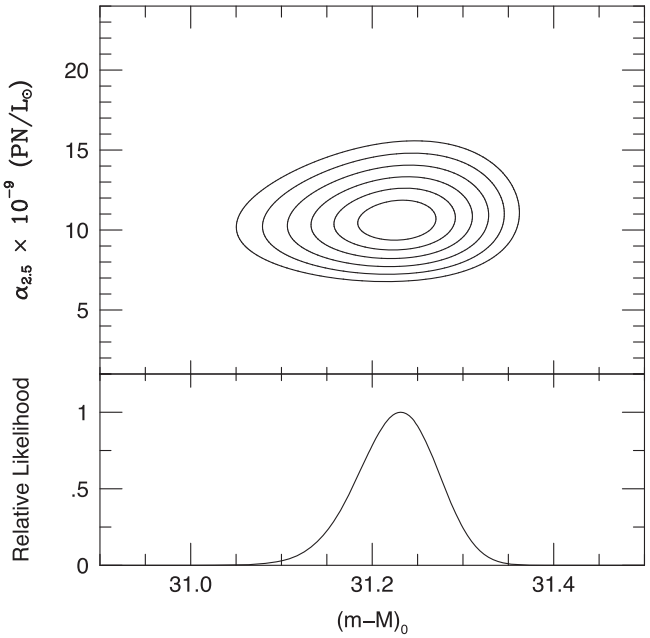

Figure 23. The top panel shows the results of the maximum-likelihood solution for NGC 1399's distance modulus. The abscissa is the galaxy's true distance modulus, the ordinate is $\alpha_{2.5}$, the number of PNe within 2.5 mag of M^*, normalized to the amount of bolometric light sampled. The contours are drawn at 0.5σ intervals. The bottom panel marginalizes over $\alpha_{2.5}$.

agreement between the observed PN distribution and Equation (2) certainly supports this.

Figure 23 shows the results of our maximum-likelihood analysis. If we assume a foreground reddening of $E(B-V)=0.011$ (Schlafly & Finkbeiner 2011), then a fit of Equation (2) to NGC 1399's observed PNLF results in a distance modulus of $(m-M)_0 = 31.23^{+0.04}_{-0.05}$. When folded in with the ∼0.05 mag zero-point uncertainty from the MUSE flux calibration, our determination of the data cube's aperture correction, and the uncertainty in the reddening, the inferred distance becomes $(m-M)_0 = 31.23^{+0.06}_{-0.07}$ or $17.6^{+0.5}_{-0.6}$ Mpc.

Both the distance and PN/luminosity values are almost identical to those measured by McMillan et al. (1993) using interference filter observations with the Blanco 4 m telescope through significantly worse (1.″3) seeing. However, our value is almost 20% shorter than the latest HST-based SBF distance of 21.1 ± 0.7 Mpc from Blakeslee et al. (2010). It is also slightly closer than recent Cepheid and TRGB distances to the Fornax cluster, though not to NGC 1399 itself (e.g., Riess et al. 2016; Jang et al. 2018; Hoyt et al. 2021). However, the uncertainties in these measurements do largely overlap.

5.8. NGC 1404 (FCC 219)

NGC 1404 is another Fornax galaxy, located near the very center of the cluster. For the long-term objective of our study, this E1 galaxy is particularly interesting, as it has hosted two Type Ia SNe, SN 2007on and SN 2011iv, whose distance estimates differ by as much as 14% (Gall et al. 2018). The galaxy is also compelling for technical reasons since a bright foreground star is projected onto the body of the galaxy. This star provides an excellent measure of the field's PSF.

There are four useful data cubes of NGC 1404 in the MUSE archive. Field P1, which includes the galaxy's nucleus, is a 3287 s exposure with 0.″88 seeing at 5007 Å (ESO Archive ID: ADP.2017-12-13T01:47:07.213, PI: M. Sarzi, Program ID: 296.B-5054). The three other exposures are of a halo field (P2), which is located north–northwest of the nucleus along the system's major axis. The exposure times for these three cubes are 1680 s, and their net seeing is 1.″01 at 5007 Å (IDs: ADP.2017-12-05T15:14:58.786, ADP.2017-12-01T13:57:32.491, ADP.2017-12-01T13:57:32.480; same PI and ID as above). As the archive did not provide a combined data cube for P2, we chose to reduce the entire data set anew. The locations of both fields are shown in Figure 24.

Our DELF analysis of NGC 1404's data cubes initially found 179 PN candidates, with the vast majority located in the central field. Further inspection of the candidates' spectra eliminated 53 objects from consideration, either on the basis of classification as interlopers, or as spurious detections that were too faint to meet the detection criteria. This left us with a sample of 126 PNe candidates: 107 in P1, 18 in P2, and one object common to both data cubes. (The two measurements of this object, 27.92 ± 0.05 on P1 and 27.88 ± 0.07 on P2 are in excellent agreement.) Most importantly, ∼64 of the PNe populate the top ∼1 mag of the luminosity function.

Like NGC 1399, NGC 1404 has been well studied photometrically (e.g., Franx et al. 1989; Sparks et al. 1991; Muñoz-Mateos et al. 2009) and kinematically (D'Onofrio et al. 1995; Iodice et al. 2019), allowing us to estimate the amount of light and line-of-sight velocity dispersion at every location in the data cube. Also like NGC 1399, a comparison of the distribution of light and PNe in the galaxy reveals that our survey is incomplete within ∼10″ of the nucleus. The exclusion of this region removes seven PNe from the sample and leaves $V \sim 10.8$ mag of galaxy light in the two data cubes.

Figure 25 shows NGC 1404's PNLF, along with the best-fitting PN luminosity function. The figure illustrates that our PN detections in NGC 1404 do not go as deep as in some other galaxies of Fornax, and faint-end incompleteness sets in only ∼0.8 mag below M^*. Nevertheless, the PNLF cutoff is very well defined, and for a foreground reddening of $E(B-V)=0.010$, the analysis displayed in Figure 26 yields a distance modulus of $(m-M)_0 = 31.37^{+0.04}_{-0.07}$. When combined

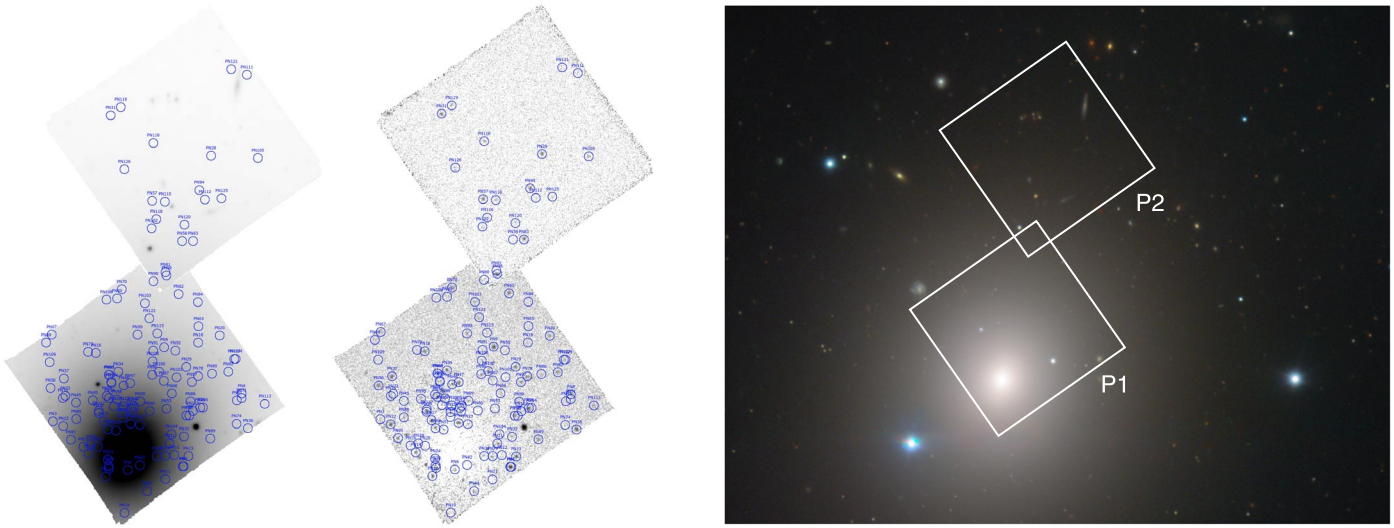

Figure 24. NGC 1404. Left: thumbnail off-band and difference images derived from the MUSE data cubes. The PN candidates are circled in blue. Right: a broadband image with the MUSE survey regions outlined in white. (Credit: ESO). A high-resolution image of the off-band and difference images is available online. The animation (available online) begins with the off-band image and then steps through the MUSE layers centered on the galaxy's redshifted [O III] wavelength to show how all emission-line objects, especially the PNe, rise and fall in brightness with wavelength.

(An animation of this figure is available.)

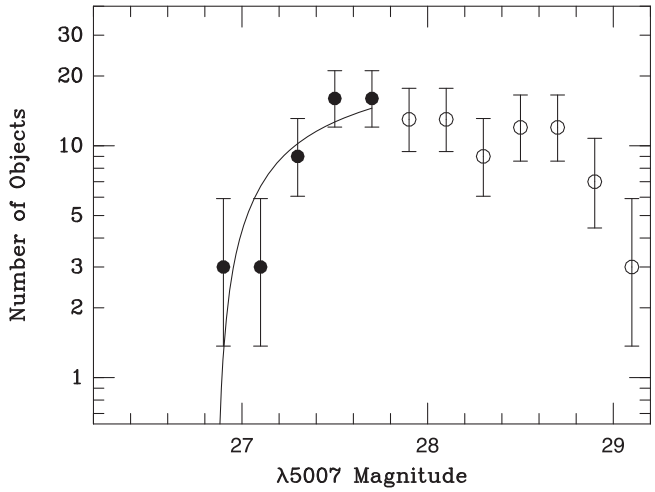

Figure 25. The observed PNLF of NGC 1404 binned into 0.2 mag intervals. The open circles denote data beyond the completeness limit; the error bars represent 1σ confidence intervals (see Gehrels 1986). The black curve shows the most likely fit to Equation (2). Note that the process of binning makes the brightest PNe appear exceptional; in fact, it is only 0.04 mag more luminous than the second brightest object.

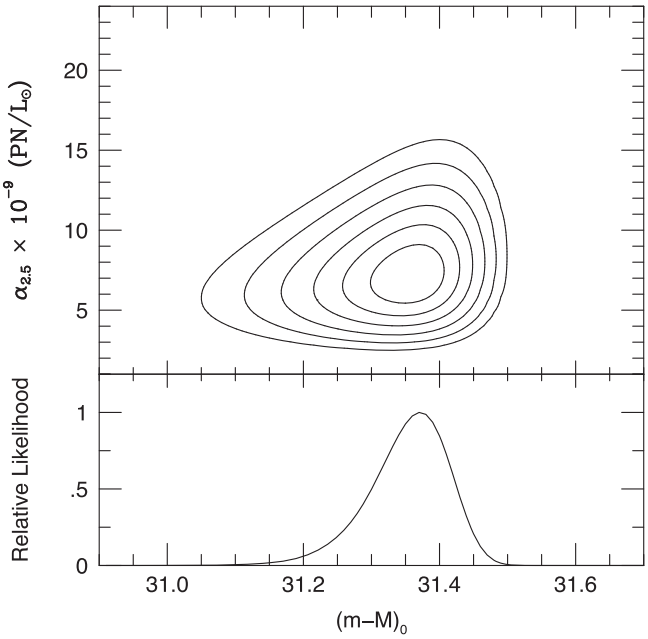

Figure 26. The upper panel shows the results of the maximum-likelihood solution for NGC 1404. The abscissa is the galaxy's true distance modulus, the ordinate is the number of PNe within 2.5 mag of M^*, normalized to the amount of bolometric light sampled, and the contours are drawn at 0.5σ intervals. The lower panel marginalizes over the PN/light variable.

with the ∼3% error on the MUSE flux calibration (Weilbacher et al. 2020), and the very small uncertainties associated with the aperture correction (see Appendix B) and reddening, the final distance modulus becomes $(m-M)_0 = 31.37^{+0.05}_{-0.08}$, or $18.8^{+0.4}_{-0.6}$ Mpc.

Unsurprisingly, as Figure 27 illustrates, our distance is in excellent agreement with the $(m-M)_0 = 31.42 \pm 0.1$ value derived by Spriggs et al. (2020), as the measurements use the same MUSE data cubes and are not systematically different (although the error bars on the DELF photometry are smaller; see Paper I). Our value is also essentially identical to the galaxy's two TRGB distance moduli, $(m-M)_0 = 31.36 \pm 0.04$ (stat)$\pm$0.05 (sys) measured by Hoyt et al. (2021), and 31.29 ± 0.07 derived by Anand et al. (2022). It is, however, significantly more distant than the poorer-seeing PNLF estimate of $(m-M)_0 = 31.15^{+0.07}_{-0.10}$ found by McMillan et al. (1993).

5.9. NGC 1419

NGC 1419 is a small elliptical galaxy in the Fornax cluster, with SBF distances generally ranging from 19–22 Mpc (Blakeslee et al. 2001; Tonry et al. 2001; Blakeslee et al. 2009). The ESO archive contains a single MUSE pointing of the galaxy, with a footprint as shown in Figure 28 (ESO Archive ID: ADP.2018-03-26T15:02:26.469, PI: M.

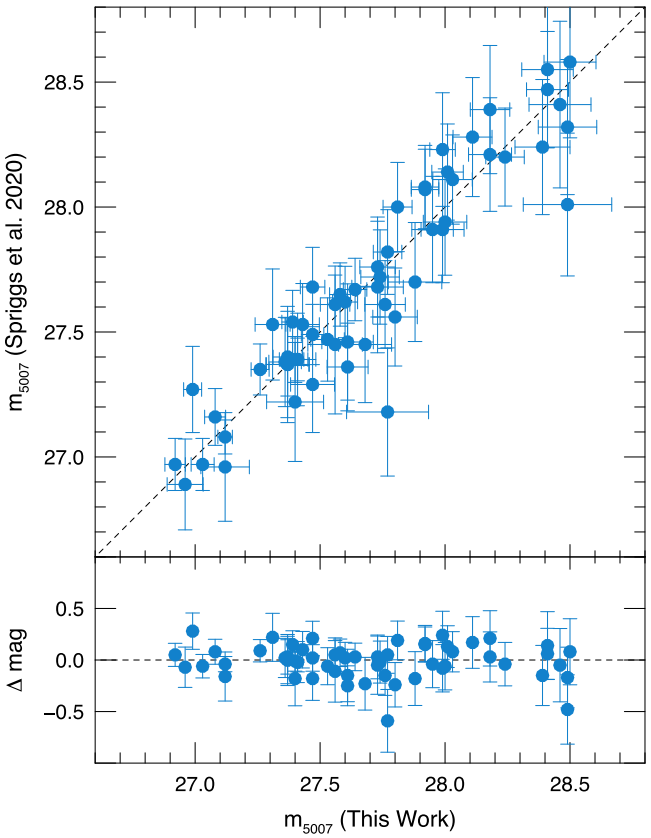

Figure 27. A comparison between our PN photometry for NGC 1404 and that of Spriggs et al. (2020); the error bars for the latter are estimated from the inverse of the quoted peak amplitude to residual-noise level ratio (A/rN). The standard deviation of the distribution is 0.13 mag, and the mean offset between the two data sets (excluding the two outliers) is 0.006 mag.

Sarzi, Program ID: 296.B-5054). This MUSE-DEEP data cube was assembled from two observations, with an effective observation time of 4921 s, and a seeing at 5007 Å of 0.″87. Owing to the low luminosity of the host galaxy (the MUSE data cube encompasses only $V \sim 12.9$ of galaxy light), just 21 PNe were detected, with only ∼12 in the top ∼1 mag of the luminosity function where the data are likely complete. This limits our ability to constrain the system's distance.

Figure 29 shows the cumulative PNLF of the galaxy. As with NGC 1366, the shape of the bright end of the distribution is in good agreement with the empirical law defined by Equation (2). However, the exact magnitude of the PNLF cutoff is not well defined due to the limited PN data set.

We measured the amount of galaxy light underlying the position of each PNe and over the MUSE data cube as a whole using the *B*-band surface photometry of de Carvalho et al. (1991); these data were then converted to *V* by assuming a color of $(B-V) = 0.89$ (Prugniel & Heraudeau 1998). To estimate the line-of-sight velocity dispersion, we used the measurements of Graham et al. (1998) for objects in the inner ∼20″ of the galaxy and adopted 50 km s^{-1} for PNe at larger galactocentric radii.

The results of our analysis are shown in Figure 30. With a reddening of $E(B-V) = 0.011$, our fit to the PNLF gives $(m-M)_0 = 31.39^{+0.10}_{-0.26}$; when we include a ∼0.06 mag error due to the flux calibration, aperture correction, and extinction our final value is $(m-M)_0 = 31.39^{+0.12}_{-0.27}$, or $18.9^{+1.1}_{-2.5}$ Mpc. This value is consistent with membership in the Fornax cluster and is essentially identical to our distance to NGC 1404, but on the low side of the distribution of SBF distances and smaller than the most recent SBF distance of $d = 22.9 \pm 0.9$ Mpc (Blakeslee et al. 2009). Given the known zero-point offset between the PNLF and SBF distance scales, the difference is a bit larger than expected.

5.10. NGC 1433

NGC 1433 is a barred spiral galaxy (Hubble type (R')SB(r) ab), which shows a double ring structure, an AGN, and a bright central region of intense star formation. The galaxy has been observed extensively as part of the PHANGS program (PI: E. Schinnerer, Program ID: 1100.B-0651), from which we have used their nine MUSE pointings. The IDs of these data cubes, along with their exposure times and seeing at 5007 Å are listed in Table 5; their positions are shown in Figure 31.

The identification and measurement of PNe in NGC 1433's were made difficult by two problems: diffuse emission from the system's interstellar gas, and the lack of point sources (i.e., PSF stars) in the field. The former issue increases the random photometric errors of the PN measurements, as the complex morphology and excitation of the emission-line gas results in uncertain background subtractions around the [O III] λ5007 and Hα lines. The latter problem introduces a systematic error into the photometry of each pointing, as without bright PSF stars, it is impossible to accurately determine the aperture correction applicable to our faint-object photometry. When the data from all nine fields are combined, this systematic error then manifests itself as a pseudo-random error, which smooths out and distorts the shape of the PNLF. The net effect of this smoothing is to bias the PNLF results toward smaller distances.

Using the DELF technique we identified almost 500 pointlike [O III] λ5007 sources across NGC 1433's disk; after examining the spectra of these objects, almost half were excluded as interlopers. This left us with 258 PN candidates, with over 120 in the top ∼1 mag of the luminosity function. As the lower panel of Figure 32 illustrates, the luminosity function of these data is very well defined and complete to at least $m_{5007} = 28.2$. However, the bright-end cutoff of the PNLF has a shape that is closer to that of a power law than an exponential. Part of this behavior is due to the existence of two sources that are ∼0.3 mag more luminous than the next brightest planetary. A careful inspection of the DELF-extracted data cube surrounding these sources reveals that their [O III] measurements are likely contaminated by light from the regions' bright and irregularly distributed emission-line gas. However, even if these two bright objects are excluded, the shape of the PNLF's cutoff is still somewhat less abrupt than expected.

The behavior of NGC 1433's PNLF is consistent with the hypothesis that the PN photometry of the galaxy is compromised by the zero-point issues described above. The system's nine non-overlapping data cubes were taken under a range of seeing conditions (from 0.″64–1.″05 seeing), which made placing all the PN candidates on a unified flux scale difficult. This is evidenced by the distribution of PN magnitudes within the fields. Pointing P5 contains no good PSF stars, and the zero-point error associated with the uncertain aperture correction may be as large as 0.1 mag. Not coincidentally the field contains the three brightest PNe in our sample. Pointing P3, which also has a highly uncertain ($\sigma \sim 0.1$ mag) zero-point due to its lack of PSF stars, contains the fourth and fifth brightest PNe. Conversely, the most luminous PNe in P2, a third field

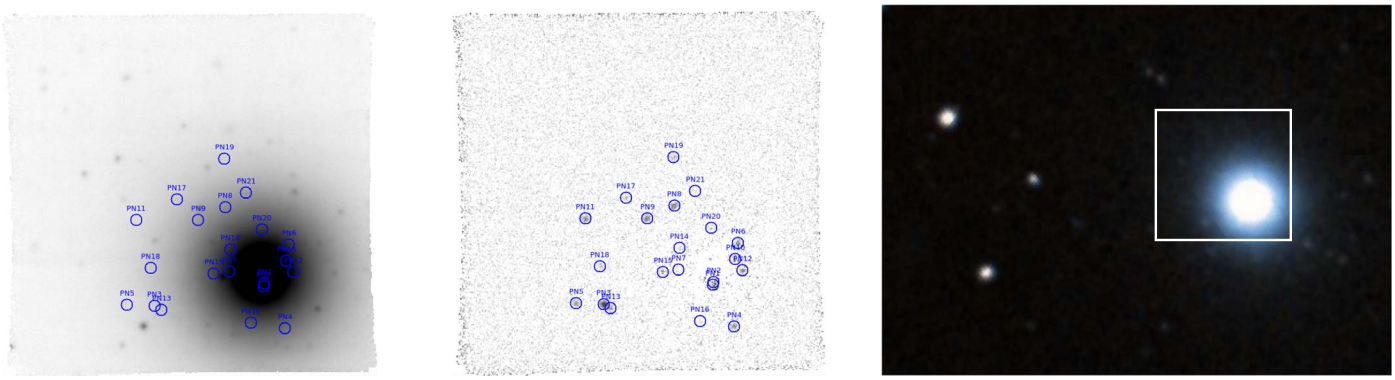

Figure 28. NGC 1419. Left: thumbnail off-band and difference images derived from the MUSE data cube. Right: a broadband image with the location of the MUSE data cube outlined in white. (Credit: DSS). A high-resolution image of the off-band and difference images is available online. The animation (available online) begins with the off-band image and then steps through the MUSE layers centered on the galaxy's redshifted [O III] wavelength to show how all emission-line objects, especially the PNe, rise and fall in brightness with wavelength.

(An animation of this figure is available.)

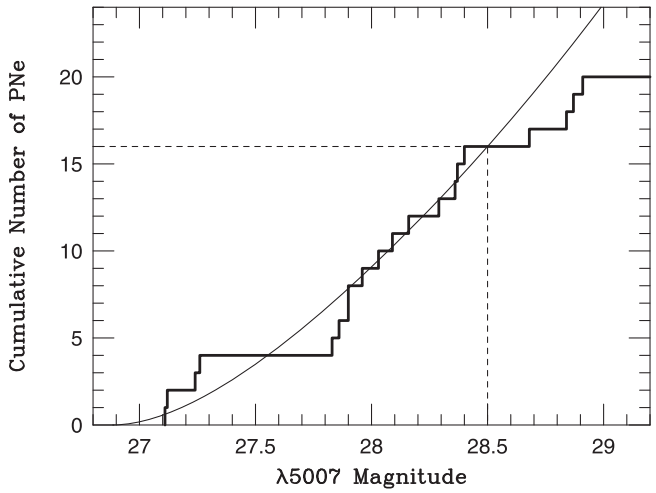

Figure 29. The cumulative luminosity function for PNe in NGC 1419. The dark line represents the observed data; the curve is Equation (2) shifted to the most likely apparent distance modulus of $(m - M)_0 = 31.42$. The dashed line shows where incompleteness begins to affect the detections. Data brighter than this are consistent with being drawn from the empirical function.

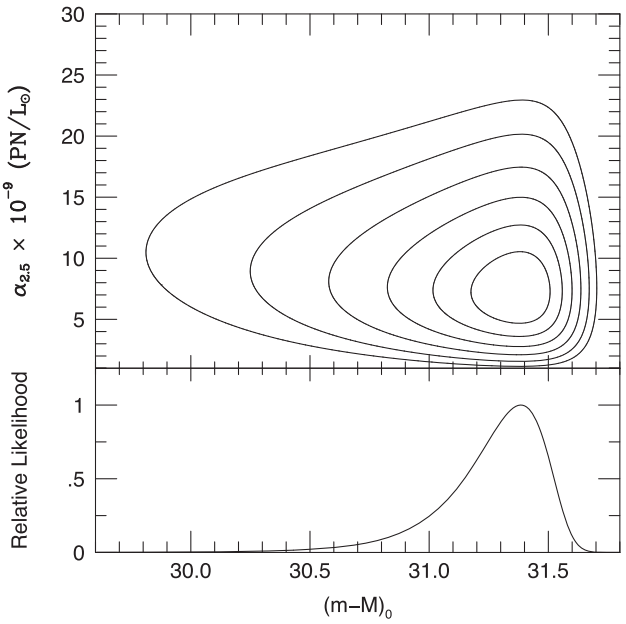

Figure 30. The upper panel shows the results of the maximum-likelihood solution for NGC 1419. The abscissa is the galaxy's true distance modulus, the ordinate is the number of PNe within 2.5 mag of M^*, normalized to the amount of bolometric light sampled, and the contours are drawn at 0.5σ intervals. The lower panel marginalizes over the PN per unit light variable.

with no bright point sources, is 0.3 mag fainter than the brightest PN in P6, a pointing that does have a reliable aperture correction.

Thus, it is quite likely that the bright tail of NGC 1433's PNLF is entirely due to zero-point errors in the PN photometry. If so, there are three ways to handle this type of error. The first is simply to discard the PNe in fields where the aperture correction and/or flux calibration is untrustworthy. This removes a third of the sample, but, as shown in the upper panel of Figure 32, it produces a PNLF more in line with the expectations of Equation (2).

A second possibility is to artificially shift the PNLF's of those MUSE pointings with poor photometric zero-points to match the data acquired from data cubes with robust aperture correction measurements. If the PN samples within the data cubes were larger, this might be a viable methodology. However, since each cube only contains five or six PNe in the top magnitude of the luminosity function, it would be impossible to determine the appropriate shifts with the accuracy needed for coaddition.

Table 5
Data Cubes for NGC 1433

Field	Archive ID	Exp Time (s)	Seeing (5007 Å)
P1	ADP.2019-12-22T01:43:14.831	2580	0.″88
P2	ADP.2019-12-22T01:22:27.745	2580	0.″90
P3	ADP.2019-12-17T22:49:20.671	2580	0.″94
P4	ADP.2019-11-27T01:02:00.695	2580	0.″93
P5	ADP.2017-06-14T09:12:09.412	3840	0.″89
P6	ADP.2019-11-27T02:44:54.831	2580	0.″73
P7	ADP.2020-01-09T22:41:58.291	2580	0.″74
P8	ADP.2020-01-11T02:39:27.620	2580	0.″76
P9	ADP.2020-01-08T07:08:40.807	2580	0.″59

The third way to handle variations in each data cube's zero-point is to increase the random photometric errors assigned to each individual PN. This, of course, is an approximation and

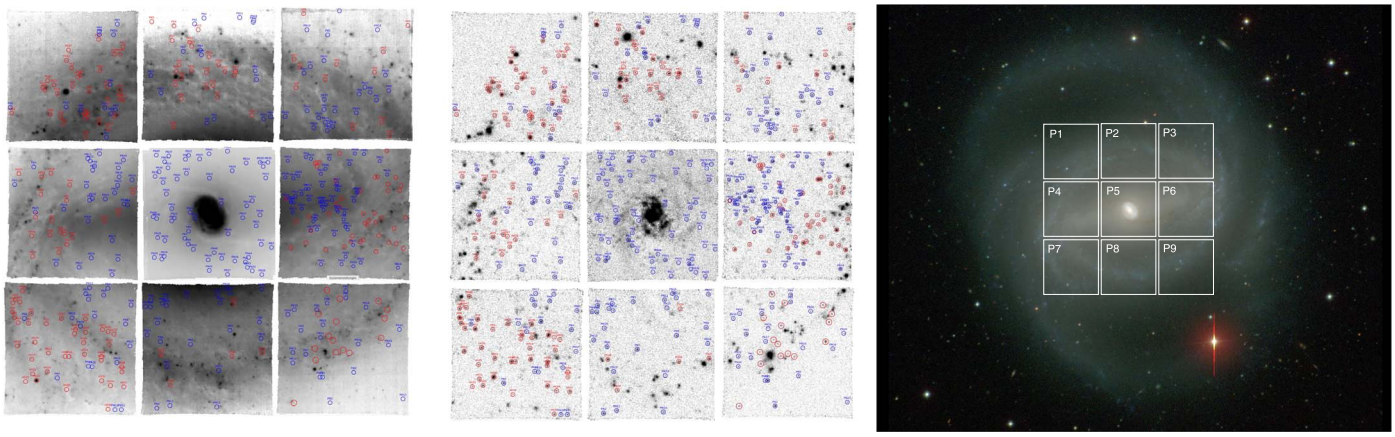

Figure 31. NGC 1433. Left: thumbnail off-band and difference images derived from the MUSE data cubes. Our PNe candidates are highlighted in blue, while emission-line interlopers are shown in red. Note that the numbering of markers is assigned to the individual pointings P1…P9, not to the final sample of the galaxy as a whole. Right: a broadband image of the galaxy with the MUSE fields outlined in white. (Credit: CGS). A high-resolution image of the off-band and difference images is available in online.

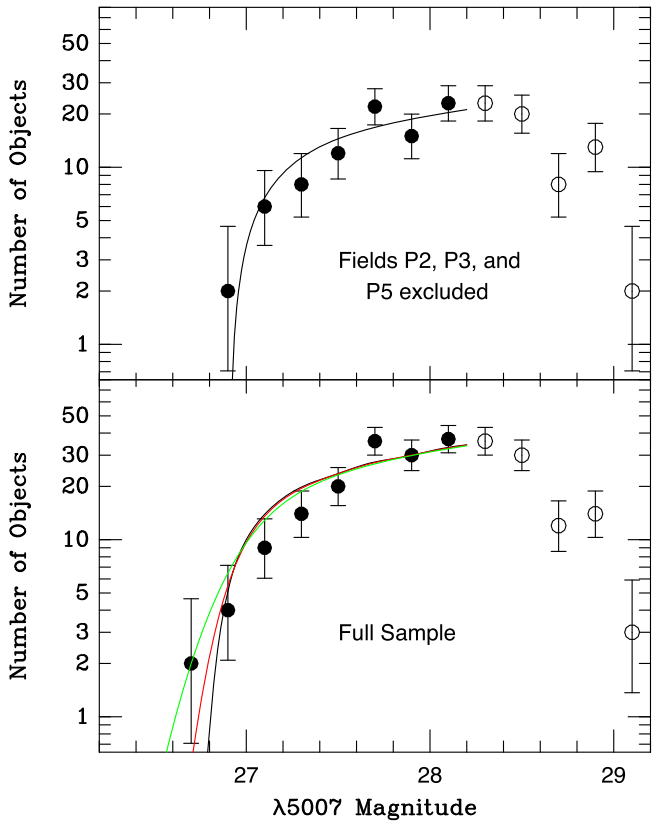

Figure 32. The observed PNLF for NGC 1433 binned into 0.2 mag intervals. Open circles denote data beyond the completeness limit; the error bars are from small number counting statistics (Gehrels 1986). The bottom panel displays the full data set, along with three curves which all assume an apparent distance of $(m - M) = 31.36$, but with different amounts of an additional photometric error added in quadrature (0.0 mag for the black curve, 0.1 mag for red, and 0.2 mag for green). The top panel shows the data when the three fields with poorly known aperture corrections are excluded. The magnitude distribution is a much better match to Equation (2) and implies a most likely apparent distance modulus of $(m - M) = 31.45$.

somewhat arbitrary: the aperture correction errors of each data cube act in a systematic fashion, shifting all the PN magnitudes in the same manner. However, if one assumes that (a) each MUSE pointing contains a similar number of PNe and (b) the distribution of zero-point errors over the nine data cubes is roughly Gaussian, then the expected distortion in the PNLF's shape can be easily modeled and fit to the data in the manner outlined by Chase et al. (2023). For example, the curves shown in the bottom panel of Figure 32 all assume an apparent distance modulus of $(m - M) = 31.35$ and the PNLF of Equation (2). However, while the black curve shows the expected PNLF in the absence of additional errors, the red and green curves show what the curve would look like with an additional 0.1 and 0.2 mag of randomly distributed errors, respectively. These errors, which could either be due to poor PN background subtraction or the effect of imperfect aperture corrections in each of the nine fields, produce a function that adequately represents the observed data.

To derive the best-fit curves shown in Figure 32 we started with the galaxy continuum measurements from the MUSE data cube. While Buta (1986) and Buta et al. (2001) do provide a plot of NGC 1433's azimuthally averaged surface brightness profile, the galaxy's complex two-dimensional morphology, with its bulge, bar, and ring-like structures precludes the use of any simple photometric model. Consequently, we estimated the amount of light underlying each PN directly from stellar continuum measurements on the MUSE data cubes. Excluding the central $\sim 3''$ of the galaxy, where PN detections are difficult, the total amount of V-band light contained in the nine MUSE pointings is $V \sim 10.5$. We also adopted a single number for the galaxy's line-of-sight stellar velocity dispersion. Buta et al. (2001) have shown that in the inner $\sim 30''$ of the galaxy, this number is $\sim 75\ \mathrm{km\ s^{-1}}$, a value significantly smaller than the velocity difference needed to deblend the emission lines of two superposed PNe. Consequently, we simply use this number throughout the galaxy.

Figure 33 uses the entire nine field data sample to illustrate how the inferred distance to NGC 1433 depends on the accuracy of the photometry. If the formal errors of the photometry are accurate, then the galaxy's most likely apparent distance modulus is $31.21^{+0.04}_{-0.04}$, though there is some likelihood that superpositions are biasing the result. However, if we assume that there are additional sources of photometric error, such as those produced by incorrect estimates of the PSF aperture corrections or poor sky subtraction of the galaxy's diffuse emission, then the

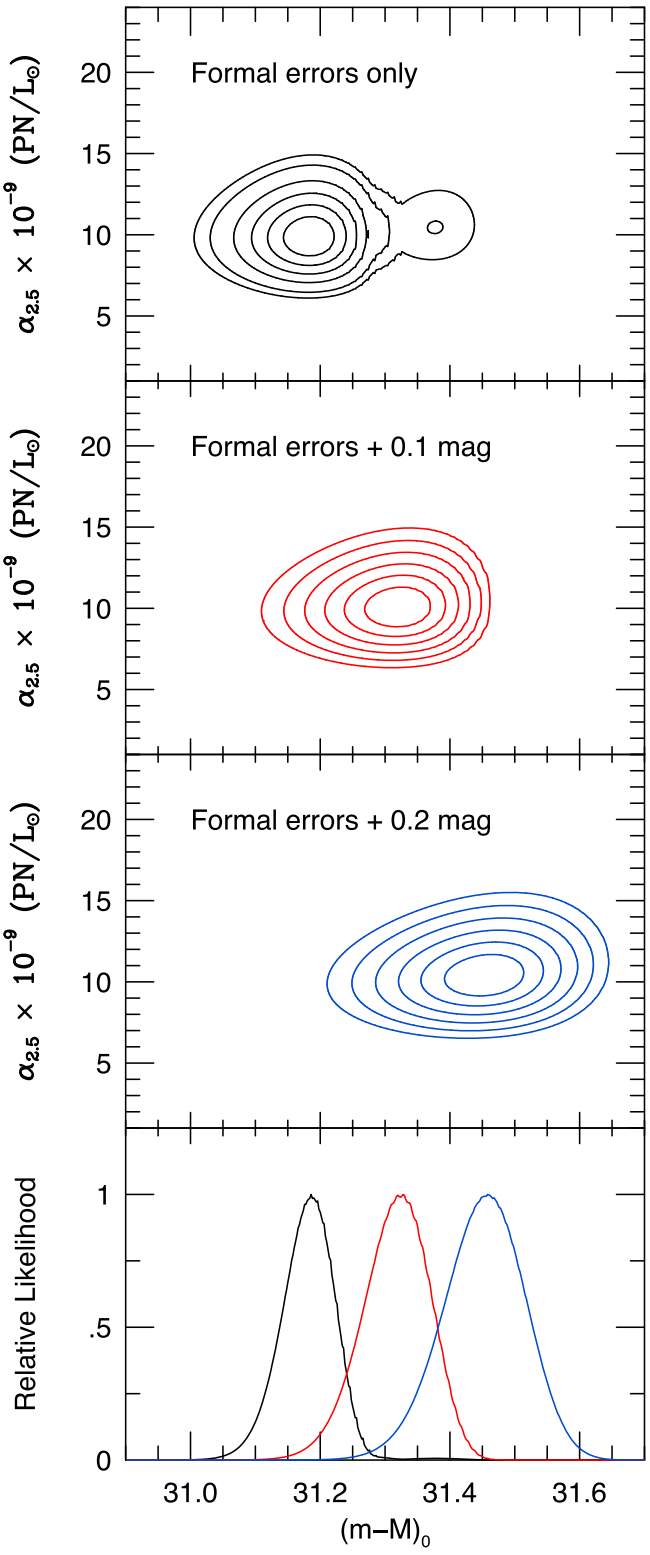

Figure 33. The top three panels show our maximum-likelihood solution for NGC 1433. The abscissa is the galaxy's true distance modulus, while the ordinate for the top three panels is $\alpha_{2.5}$, the number of PNe within 2.5 mag of M^*, normalized to the amount of bolometric light sampled. The contours are drawn at 0.5σ intervals. Three different solutions are shown: one where the errors are solely those reported by the PN photometry, and two others where we assume the existence of additional random uncertainties due to poor background subtraction and our inability to accurately measure each cube's aperture correction. The bottom panel marginalizes these solutions over $\alpha_{2.5}$. Note how the galaxy's inferred distance depends on the photometric precision.

best-fit distances increase to $(m - M) = 31.35^{+0.04}_{-0.06}$ (for $\sigma_{\rm add} = 0.1$ mag) and $(m - M) = 31.49^{+0.06}_{-0.07}$ (for $\sigma_{\rm add} = 0.2$ mag).

To understand the trend seen in Figure 33, consider the basis behind the PNLF method. PNLF distances are defined by measuring the shape of the function's rapid bright-end cutoff. In defining this shape, a single PN near M^* carries more weight than a similar PN at fainter magnitudes—the brighter the PN, the greater its effect on the measured value of M^*. Consequently, random photometric errors will turn into a systematic fitting error, and an underestimate of galaxy distance. The only way to avoid this systematic is to carefully model the effect of errors on the PNLF, either through the application of an Eddington (1913) correction to the binned data, or by fitting the PN magnitudes, not to the expression given by Equation (2), but to the result of a convolution of the fitted function with a kernel that represents the expected amplitude of the errors (Ciardullo et al. 1989).

In the case of NGC 1433, the aperture corrections for pointings P2, P3, and P5 are poorly known, as are their errors. In the absence of this information, magnitude excursions to the bright side of the true value push the resultant distance to smaller values more than those excursions that work the other way. Thus, the PNLF's best-fit distance modulus is underestimated.

A confirmation of this effect comes from the PNLF solution when objects from the three fields with poorly determined aperture corrections, P2, P3, and P5, are removed from the analysis. For these higher-quality data, the distance modulus for an assumed $E(B - V) = 0.008$ is $(m - M)_0 = 31.42^{+0.04}_{-0.06}$. If we then assume a nominal uncertainty of 0.06 mag for the flux calibration and aperture correction, then the distance to the galaxy becomes $(m - M)_0 = 31.42^{+0.07}_{-0.08}$, or 19.2 ± 0.7 Mpc.

Our result for NGC 1433 is essentially identical to that of Scheuermann et al. (2022), who use the same MUSE data cube to identify 90 PNe in the galaxy and derive a distance modulus of $(m - M)_0 = 31.39^{+0.04}_{-0.07}$ $(18.94^{+0.39}_{-0.46})$ Mpc. We support their explanation of the conflict between our PNLF distance and the TRGB result of ∼9 Mpc (Sabbi et al. 2018): confusion between RGB and AGB stars. The PNLF of Figure 32 rules out a distance modulus that would be smaller by as much as 1.6 mag: PNe that bright are simply not seen in this galaxy.

5.11. NGC 1512

NGC 1512 is a barred spiral galaxy, classified SB(r)a, with both a traditional outer ring and an inner disk that encompasses a UV-bright nucleus with intense star formation. As the galaxy is relatively inclined ($i \sim 72°$), it has been the target of a myriad of Tully–Fisher investigations, all of which place the system between ∼11 and 15 Mpc away (see Tully et al. 2009). A TRGB analysis derived from multiwavelength HST photometry agrees with this assessment, assigning a distance at the near end of this range (11.6 Mpc; Sabbi et al. 2018). A grid of nine MUSE pointings obtained by the PHANGS program (PI: E. Schinnerer, C.M. Carollo, IDs: 1100.B-0651, 099.B-0242) covers the galaxy and is available in the ESO archive. These pointings are listed in Table 6 and shown in Figure 34.

Since there is little to no surface photometry available for NGC 1512, we used continuum measurements from the MUSE IFUs to estimate the amount of galaxy light falling onto the nine data cubes and at the position of each PN. Also, since NGC 1512 is a disk galaxy, we did not attempt to model the

Table 6
Data Cubes for NGC 1512

Field	Archive ID	Exp Time (s)	Seeing (5007 Å)
P1	ADP.2019-02-05T06:15:31.835	2580	0.″82
P2	ADP.2018-03-02T17:54:29.654	3225	1.″75
P3	ADP.2018-03-08T17:26:28.765	2580	0.″73
P4	ADP.2019-02-05T06:15:31.827	2580	0.″81
P5	ADP.2017-12-12T10:52:12.342	3600	0.″82
P6	ADP.2018-03-08T18:22:48.347	2580	0.″76
P7	ADP.2019-02-12T01:24:29.983	2580	1.″27
P8	ADP.2019-02-12T01:24:30.018	2580	1.″10
P9	ADP.2019-02-12T01:24:29.997	2580	0.″89

system's line-of-sight velocity dispersion, as we expect this number to be much less than the minimum velocity separation that can be deblended by the MUSE spectrograph. In our analysis, we adopted 50 km s^{-1} for this value.

PN detections within an isophotal radius of $\sim$13′ of NGC 1512's nucleus are extremely difficult, due to the region's high surface brightness and bright diffuse emission, so we eliminated the region from our analysis. Also, poor seeing precluded faint point-source detections in fields P2 and P7, so these areas were also excluded from consideration. That left us with $V \sim 11$ mag of galactic light hosting 210 PN candidates found by our DELF analysis. Over 60 of these objects are in the top $\sim$1 mag of the luminosity function. Figure 35 displays the object's PNLF.

As Figure 35 illustrates, the bright end of NGC 1512's PNLF is very well defined, with a cutoff magnitude of $m_{5007} \sim 27$. However, there is one slight ambiguity: the shape of the PNLF, as defined by the PNe with $m_{5007} > 27$, suggests a PNLF cutoff that is very close to $m^* \sim 26.9$. Yet the brightest PN in the galaxy (PN1) is $\sim$0.1 mag brighter than this threshold. In other words, the object appears slightly overluminous compared to the apparent PNLF cutoff. One potential explanation for this brightness is a PN superposition.

This possibility is summarized in Figure 36. Because the region upon which PN1 is superposed is relatively bright ($\mu_V \sim 21$), the likelihood that the object is composed of two superposed sources is moderately high. But still, the hypothesis is disfavored: the best-fit solution considers PN1 to be a single object and yields a distance modulus of $(m - M)_0 = 31.30^{+0.04}_{-0.04}$, or 18.2 ± 0.3 Mpc (for an $E(B-V) = 0.01$). Yet if PN1 is a single, ordinary PN, the quality of the fit is rather poor, and a K-S test can rule out the null hypothesis with 86% confidence. Conversely, if PN1 is a superposition of two objects, the preferred solution is $(m - M)_0 = 31.43 \pm 0.04$; not coincidentally, this is identical to the distance of $31.43^{+0.03}_{-0.04}$ ($19.3^{+0.3}_{-0.4}$ Mpc) which is derived when PN1 is excluded entirely from the sample. In this case, the fit to Equation (2) is excellent and the K-S statistic is very small at $D_n = 0.062$. We therefore prefer the latter value for the distance.

Like NGC 1433, the PNLF of NGC 1512 is compromised by uncertainties in the zero-point errors of some of the data cubes. Specifically, pointings P3, P6, and P8 show an unusual wave-like pattern in the aperture correction versus wavelength relation and/or have noise estimates which may point to an issue in the data reduction process. Fortunately, unlike NGC 1433, the PNe of these data cubes do not dominate the bright end of the luminosity function: the second and sixth brightest PNe are in P6, while P3 and P8 contribute very little to the definition of the PNLF's cutoff. Since we estimate that the flux calibration and aperture correction errors for the remaining fields are no greater than 0.05 mag, we adopt this number as the systematic component of our error budget. Thus, if we assume a foreground reddening of $E(B-V) = 0.01$, our final distance to the galaxy is $(m - M)_0 = 31.43^{+0.06}_{-0.06}$ ($19.3^{+0.5}_{-0.6}$ Mpc).

Our result is slightly larger than the distance modulus of $(m - M)_0 = 31.27^{+0.07}_{-0.11}$ found by Scheuermann et al. (2022) from the same data cube, albeit with a much smaller sample (43) of PNe. However, it is significantly larger than the value of $\sim$11.7 Mpc found from the analysis of UV and optical HST images taken as part of the Legacy Extragalactic UV Survey (Sabbi et al. 2018). As noted for NGC 1433, the TRGB distance is much smaller than both PNLF distance estimates and probably for the same reason discussed above, i.e., confusion between the TRGB and that of the AGB.

5.12. NGC 2207/IC 2163

NGC 2207 and IC 2163 are a pair of interacting spiral galaxies in the early stages of a merger. The larger system, NGC 2207, is classified SAB(rs)bc pec and has a total B magnitude of 10.8; IC 2163 is a barred spiral of type SB(rs)c pec with $B = 11.4$ (de Vaucouleurs et al. 1991). Both galaxies exhibit robust star formation and are subject to a relatively large amount of foreground extinction ($A_V = 0.238$; Schlafly & Finkbeiner 2011).

There are no TRGB or Cepheid distances to the system, and estimates from the Tully–Fisher relation (13–17 Mpc; Bottinelli et al. 1984, 1986; Russell 2002; Theureau et al. 2007) are discordant with that determined from SN Ia 1975A (33–50 Mpc; Arnett 1982; Davis et al. 2021). Thus, a PNLF distance to the galaxies would be interesting. However, if the SN-based distances are correct, then it would be a real challenge to measure a PNLF solely from the MUSE archival data.

Three MUSE data cubes of the NGC 2207/IC 2163 system exist in the ESO archive; these data are summarized in Table 7. Field P1, which is centered on the nucleus of NGC 2207 was surveyed as part of Program 0102.D-0095 (PI: J. Anderson); data for field P3 (which covers most of IC 2163) and P2 (which connects P1 and P3) were obtained through Program ID: 0100.B-0116 (PI: C.M. Carollo). As can be appreciated from the difference image in Figure 37, the system's copious diffuse emission, coupled with the data set's relatively short exposure times and only moderate image quality, made PN detections challenging. Nevertheless, the two galaxies are luminous enough so that, if the system were at the distance implied by the Tully–Fisher measurements, then a large number of PN candidates would be observable.

Our initial examination of the MUSE data cubes identified 112 pointlike [O III] sources in the two galaxies. However, after screening the objects' spectra for evidence of strong Hα (typical of an H II region) and emission from [S II] and [N II] (the signature of an SNR), only three of the PN candidates survived. These potentially true PNe are all near the detection limit of the survey and have [O III] magnitudes of $m_{5007} = 28.77 \pm 0.13$, 29.70 ± 0.28, and 29.91 ± 0.33.

If the brightest of the objects is indeed a PN with an absolute magnitude near M^*, then the implied distance to the galaxy is close to $\sim$40 Mpc, in agreement with the analysis of SN 1975A. Scaling from Paper I's survey of NGC 474, an elliptical galaxy at a similar distance, a proper PNLF study of the system

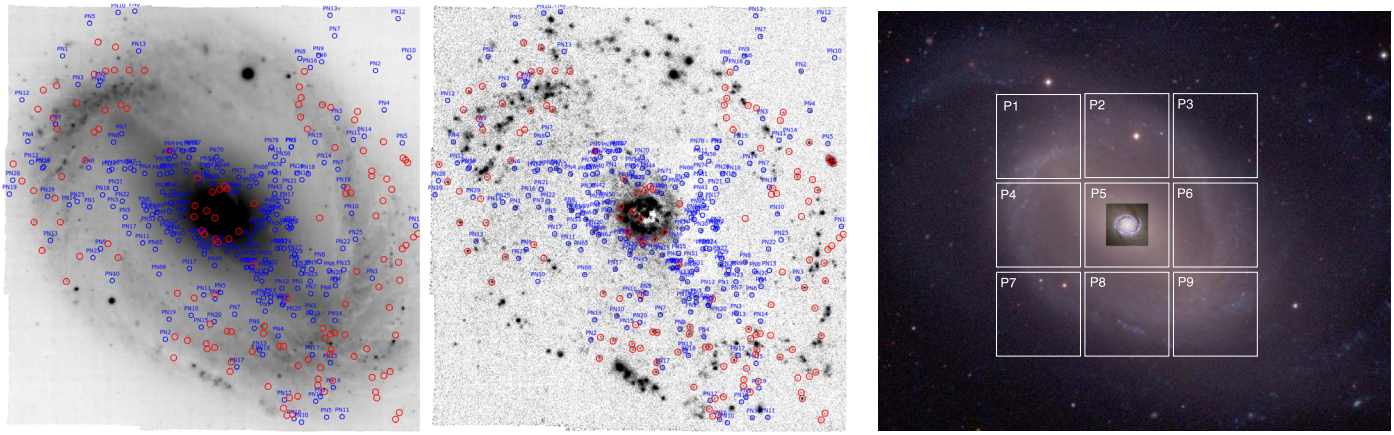

Figure 34. NGC 1512. Left: thumbnail off-band and difference images derived from the MUSE data cubes. The PN candidates are highlighted in blue, while the emission-line interlopers are shown in red. The numbering of markers is assigned to the individual pointings P1–P9. Right: broadband image of the galaxy, including a high-resolution insert of the nucleus from HST. The MUSE data cubes are outlined in white. (Credit: CGS and NASA/ESA/Hubble/LEGUS.) A high-resolution image of the off-band and difference images is available online. The animation (available online) begins with the off-band image and then steps through the MUSE layers centered on the galaxy's redshifted [O III] wavelength to show how all emission-line objects, especially the PNe, rise and fall in brightness with wavelength. (An animation of this figure is available.)

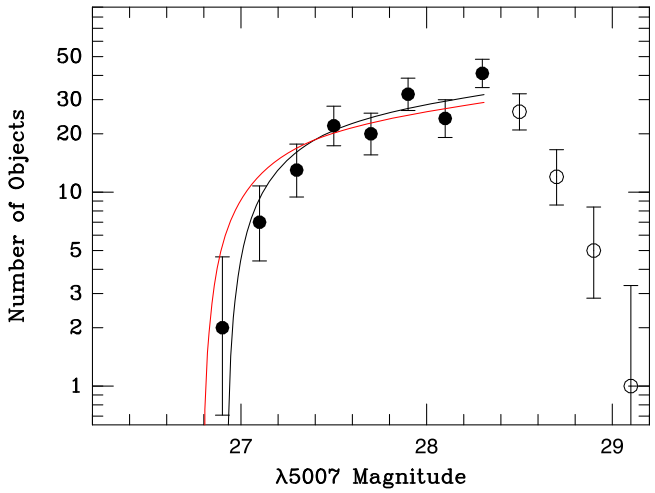

Figure 35. The observed PNLF for NGC 1512 binned into 0.2 mag intervals. Open circles denote data beyond the completeness limit; the error bars are from small number counting statistics (Gehrels 1986). The red curve shows the most likely fit to Equation (2) when PN1 is included in the analysis; the black curve shows the solution when PN1 is assumed to be made up of a superposition of two sources (or is excluded from the analysis altogether).

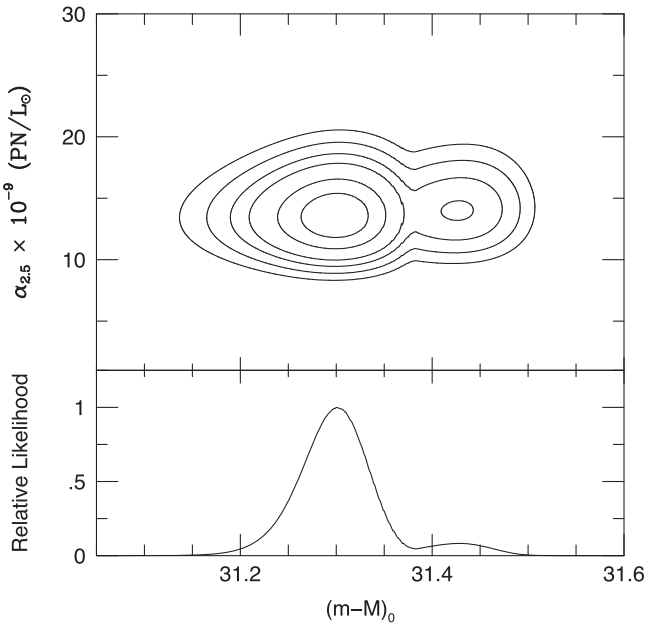

Figure 36. The top panel shows the results of the maximum-likelihood analysis for NGC 1512. The abscissa is the galaxy's true distance modulus, the ordinate is $\alpha_{2.5}$, the number of PNe within 2.5 mag of M^*, normalized to the amount of bolometric light sampled. The contours are drawn at 0.5σ intervals. The bottom panel marginalizes over $\alpha_{2.5}$. Note the bimodal solution: there is a non-negligible probability that PN1 is a superposition of two objects.

would likely require at least ∼5 hr of MUSE exposure time with ∼0.″6 seeing. With the present data, all we can say is that the PN observations are inconsistent with the galaxies' Tully–Fisher distances.

5.13. NGC 3501

NGC 3501 is an edge-on spiral, with an uncertain Hubble type of Scd. The galaxy has more than a dozen Tully–Fisher distance estimates in the literature, all within the range of 19.5–26.5 Mpc. However, the viewing angle presents an obvious challenge to standard candles such as Cepheids and the PNLF, and no TRGB distances have been published. Nevertheless, it has been shown that [O III] observations in the halos of edge-on systems can overcome the issues associated with galaxy orientation and produce reliable PNLF distances (e.g., Ciardullo et al. 1991; Jacoby et al. 1996). So MUSE has the potential to obtain a PNLF distance to the galaxy.

Table 7
Data Cubes for NGC 2207/IC 2163

Field	Archive ID	Exp Time (s)	Seeing (5007 Å)
P1	ADP.2019-03-06T02:54:12.126	2238	0.″88
P2	ADP.2018-04-05T08:26:13.265	3338	0.″66
P3	ADP.2018-04-05T08:26:13.281	2892	0.″84

As depicted in Figure 38, the one NGC 3501 MUSE data cube in the ESO archive (ID: ADP.2017-10-16T11:12:01.527, PI: F. Pinna, Program ID: 098.B-0662) consists of the combination of two pointings. The effective exposure time

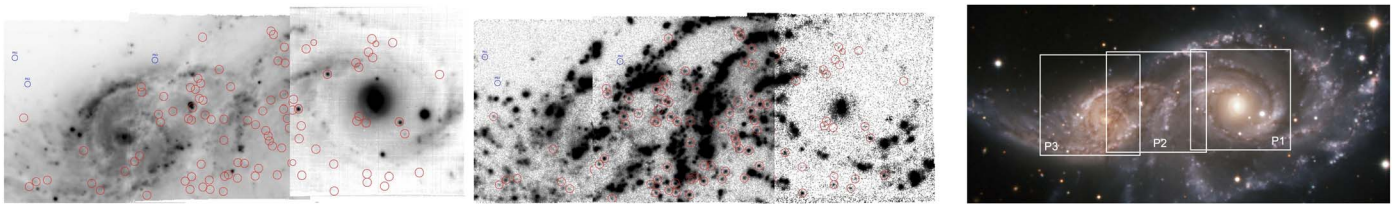

Figure 37. NGC 2207/IC 2163. Left: thumbnail off-band and difference images derived from the MUSE data cubes. The majority of pointlike [O III] sources are interloping objects (red markers); there are only three PN candidates (blue markers) present in the field. Right: a broadband image with the MUSE pointings outlined in white. (Credit: ESO). A high-resolution image of the off-band and difference images is available online.

for these data is quoted as 9600 s, but the image quality of the observation is quite poor, 1.″51. Nevertheless, the DELF technique did allow us to detect six of the system's brightest PNe, from an initial list of 17 candidates. Such a sparse sample is not suitable for a PNLF analysis, though it can be used to place limits on a galaxy's distance.

It is worth noting that, although the magnitudes of the detected PNe range from $27.69 \leqslant m_{5007} \leqslant 28.47$, the difference between the brightest and second brightest PN is 0.54 mag. This gap may simply be due to the sparsity of the sample. However, a careful examination of the [O III] line of the brightest PN hints at the possibility that the object is actually composed of a marginally resolved pair of sources; if so, the two objects are of comparable brightness and have a separation of ∼0.″4 with a position angle of 125° (Figure 39). Unfortunately, the poor image quality does not allow us to draw any definite conclusions about the source.

As with NGC 2207, we can estimate a crude upper limit to NGC 3501's distance using the magnitudes of the brightest PNe. If we believe that the brightest [O III] source is a superposition of two objects and adopt the second brightest object as our indicator, then, for a foreground reddening of $E(B-V) = 0.02$, the upper limit on the galaxy's distance is ∼38 Mpc. Alternatively, if we believe the [O III] flux from PN1 comes from a single PN, then the upper limit drops to ∼33 Mpc. Either way, these estimates are well beyond the system's Tully–Fisher values. We emphasize that this estimate is for an upper limit on the distance, so it is still consistent with other measurements. The only firm conclusion we can draw is that, under more favorable observing conditions, MUSE should be able to yield an accurate PNLF distance to the galaxy.

5.14. NGC 4038/39

The Antennae galaxy (NGC 4038/NGC 4039) is the closest, and therefore the prototypical, example of a major merger, and is well known for its spectacular antennae-like tidal tails (hence its name) and vigorous starburst activity. A PNLF study of the Antennae is particularly interesting, both because of an earlier controversial distance determination for SN 2007sr (Schweizer et al. 2008), and because it has been the focus of both TRGB and Cepheid observations. In principle, NGC 4038/39 can serve as a checkpoint for four different distance indicators, although the PNLF and SN Ia methods have ties to the Cepheid and/or TRGB scales and thus, are not fully independent.

NGC 4038/39 has been observed extensively with MUSE to study the ionization mechanism of the DIG (Weilbacher et al. 2018). As a result, there are numerous data cubes available in the ESO Archive (PI: P. Weilbacher, Program IDs: 093.B-0023, 095.B-0042). However, we chose to optimally re-reduce all the cubes with the most recent version of the MUSE pipeline (Weilbacher et al. 2020); this process removed many of the artifacts (such as Hα saturation and high sky-line residuals) present in the prior reduction. The re-reduction also allowed us to produce a set of 13 independent data cubes without the complication of changing aperture corrections in the regions of field overlap. These fields are listed in Table 8 and illustrated in Figure 40.

Our DELF analysis found 234 PN candidates scattered over the 13 fields, with almost a hundred in the top ∼1 mag of the luminosity function. In general, the spatial distribution of these PNe does not follow that of the light: in the regions of intense star formation and high obscuration, PN detections are difficult, and little effort was made to perform a comprehensive search in those areas. However, the large number of PNe found between and beyond the regions of star formation creates a very well-defined PNLF. This function is shown in Figure 41.

As is illustrated in the figure, the distribution of observed PN magnitudes in the Antennae galaxy is generally well fit by the empirical luminosity function described by Equation (2). But there is one exception: PN1, which is 0.14 mag more luminous than the second and third brightest objects, appears slightly too bright for the best-fit curve. Moreover, it is difficult to argue that the PN's [O III] flux is due to a superposition of two sources, as the location upon which the object is projected is not especially bright. Specifically, in terms of underlying surface brightness, the position of PN1 barely falls in the top one-third of the sample. But its existence forces the best-fit curve toward smaller distances.

The effect of PN1 is quantified in Figure 42, where we fit Equation (2) to the observed distribution of PN magnitudes with and without PN1. For the analysis, we assumed that the line-of-sight velocity dispersion of the galaxy's stars is $\sim 150\,\mathrm{km\,s^{-1}}$ throughout the MUSE survey region. Given the complexity of the system and the lack of any spatially resolved stellar radial velocity measurements, this was the simplest assumption we could make. Similarly, due to the irregular isophotes of the galaxy, our estimates for the amount of galaxy luminosity underlying the position of each PN were made from the MUSE spectra themselves, rather than any published surface photometry. These data imply that, after excluding those regions of the galaxy where PN detections were impossible, the 13 pointings shown in Figure 40 contain $V \sim 10.8$ mag of galaxy light.

Figure 42 confirms that, due to the large number of PNe in the top ∼1 mag of the luminosity function, the formal errors of the PNLF fits are quite small. If PN1 is excluded, the distance modulus of the system (for an $E(B-V) = 0.04$) is $(m-M)_0 = 31.86^{+0.03}_{-0.04}$, or 23.6 ± 0.4 Mpc. In other words, the statistical error for the distance is less than 2%. However, if PN1 is included, then the Antennae galaxy's most likely distance modulus decreases by 0.048 mag, a value that is greater than the statistical error of the fit. The fit with PN1 is

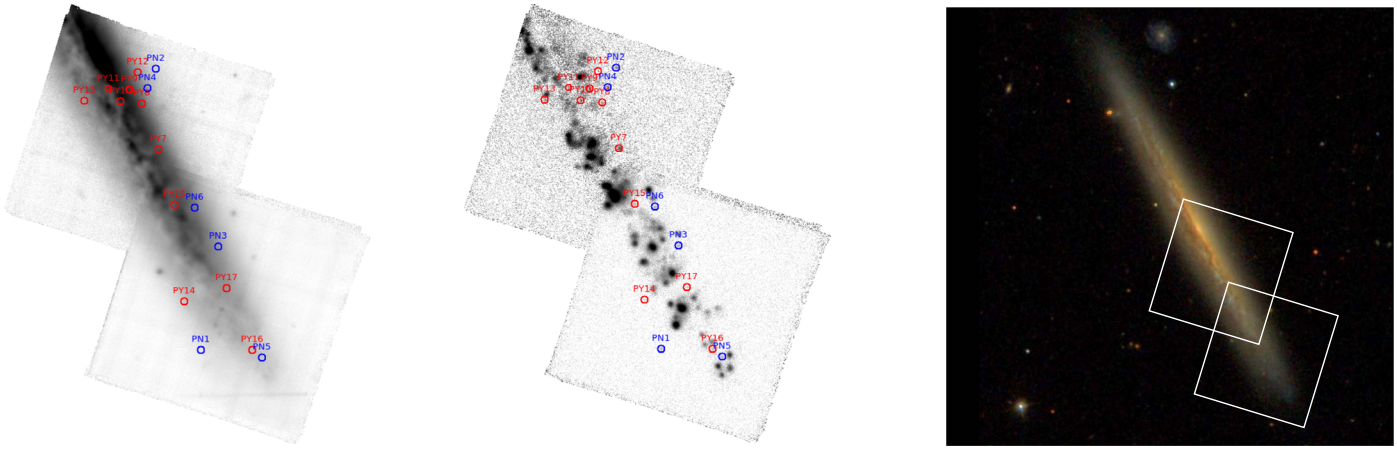

Figure 38. NGC 3501. Left: thumbnail off-band and difference images derived from the MUSE data cubes. Right: a broadband image with the locations of the MUSE fields outlined in white. (Credit: SDSS DR14). A high-resolution image of the off-band and difference images is available online. The animation (available online) begins with the off-band image and then steps through the MUSE layers centered on the galaxy's redshifted [O III] wavelength to show how all emission-line objects, especially the PNe, rise and fall in brightness with wavelength.

(An animation of this figure is available.)

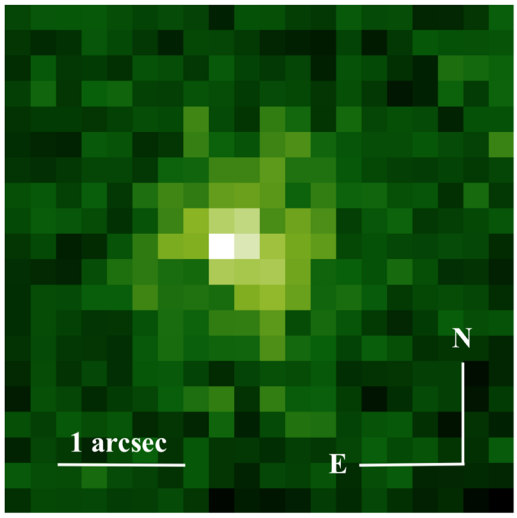

Figure 39. A possible overluminous PN in NGC 3501. The PN may be a superposition of two [O III] emission-line sources with a separation of 0.″4, but the poor (1.″51) image quality precludes a definitive statement.

Table 8
Data Cubes for NGC 4038/39

Field	Archive ID	Exp Time (s)	Seeing (5007 Å)
C01	ADP.2017-03-28T13:08:20.713	4951	0.″74
C02	ADP.2017-03-28T13:08:20.697	5013	0.″59
C03	ADP.2017-03-28T13:08:20.689	4811	0.″62
C04	ADP.2017-03-28T13:08:20.681	4985	0.″59
C05	ADP.2017-03-28T13:08:20.705	5117	0.″84
C06x	ADP.2016-06-15T08:55:13.262	2578	1.″35
C09	ADP.2017-05-24T12:39:01.277	2584	0.″81
C10	ADP.2016-09-29T05:21:54.086	2592	0.″86
C11a	ADP.2017-05-24T11:10:28.457	2498	0.″98
C11b	N/A[a]	2523	0.″78
C12a	N/A[a]	2700	0.″88
C12c	N/A[a]	2700	0.″75
C12e	N/A[a]	2700	0.″60

Note.
[a] Not available in a public archive, own data reduction (see the text).

slightly worse than that without the object, but not so much that it can be deemed inconsistent with the shape of Equation (2). Since both solutions are easily allowed by the K-S statistic, we prefer keeping PN1 in the data set. The distance is then $(m-M)_0 = 31.82^{+0.03}_{-0.04}$, or 23.1 ± 0.4 Mpc, where the uncertainties represent only the internal errors of the fits.

Since the Antennae system was observed using 13, sometimes overlapping MUSE pointings, the analysis of the systematic component of the distance determination's error budget is complicated. Most of the PNe that occupy the brightest 0.25 mag of the PNLF lie in fields C10, C5, C9, and C1. None of these fields have any anomalies in the aperture correction estimates: formally, the uncertainties in their aperture corrections are 0.029, 0.010, 0.045, and 0.001 mag, respectively. Conversely, the C4 pointing contains no suitable pointlike object for an aperture correction measurement; the best we could do is stack the field's brightest PNe and determine the aperture correction for [O III] λ5007 as explained in Paper I. This procedure likely has an uncertainty of $\sim$0.05 mag. For pointing C11b, which also contains no useful PSF stars, we took a different tack: since the seeing of the data cube was extremely similar to that of pointing C1, we simply used the latter's aperture correction in our analysis. Fortunately, the PNe contained in the pointings with the poorest aperture correction measurements do not contribute significantly to the PNLF's bright-end cutoff. We, therefore, adopt $\sim$0.06 mag as the combined zero-point uncertainty due to the MUSE data cube's flux calibration and aperture correction.

Our final distance to NGC 4038/39 is $(m-M)_0 = 31.82^{+0.07}_{-0.07}$ (or $23.1^{+0.7}_{-0.8}$ Mpc) for an $E(B-V) = 0.04$. This distance is statistically identical to the SN Ia-based value of $(m-M)_0 = 31.74 \pm 0.27$ (Schweizer et al. 2008), and is only slightly larger (but still consistent with) the system's TRGB distances, which fall near 31.67 ± 0.05 (Jang & Lee 2015; Freedman et al. 2019). Compared to the system's Cepheid distances, our value is much larger than the discordant estimate of 31.29 ± 0.11 by Riess et al. (2016) but is in reasonable agreement with the measurements of $(m-M)_0 = 31.55 \pm 0.06$ (Fiorentino et al. 2013) and 31.615 ± 0.117 (Riess et al. 2022). These results suggest that PN1 does belong in the sample, and the 0.14 mag offset between PN1 and PN2 is merely a statistical

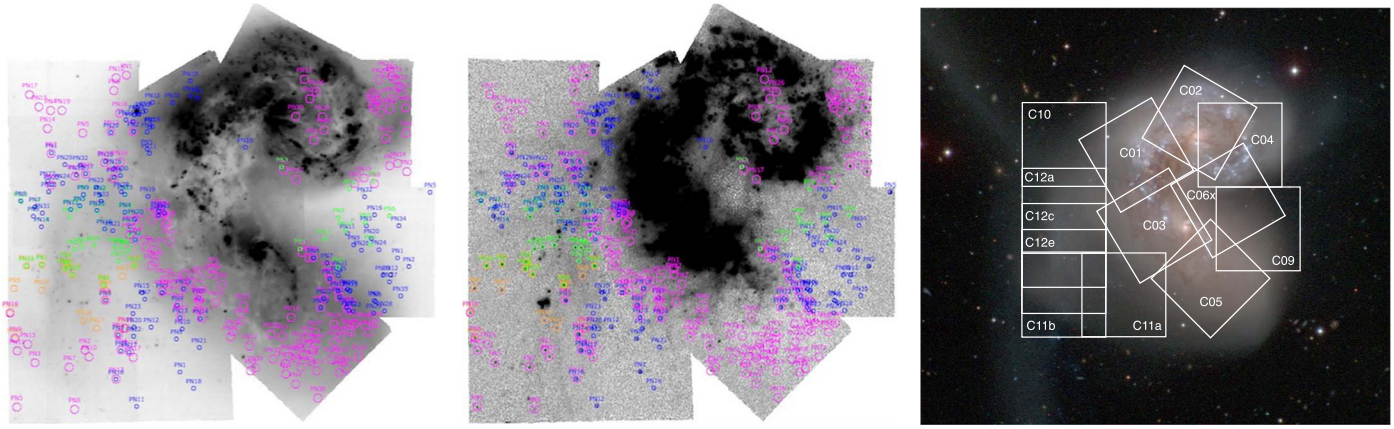

Figure 40. NGC 4038/39. Left: thumbnail off-band and difference images based on the 13 MUSE data cubes. The PN candidates are circled, with the colors of the individual pointing (C01–C12e). Right: a broadband image with the positions of the data cubes outlined in white. (Credit: CGS). A high-resolution image of the off-band and difference images is available online. The animation (available online) begins with the off-band image and then steps through the MUSE layers centered on the galaxy's redshifted [O III] wavelength to show how all emission-line objects, especially the PNe, rise and fall in brightness with wavelength.

(An animation of this figure is available.)

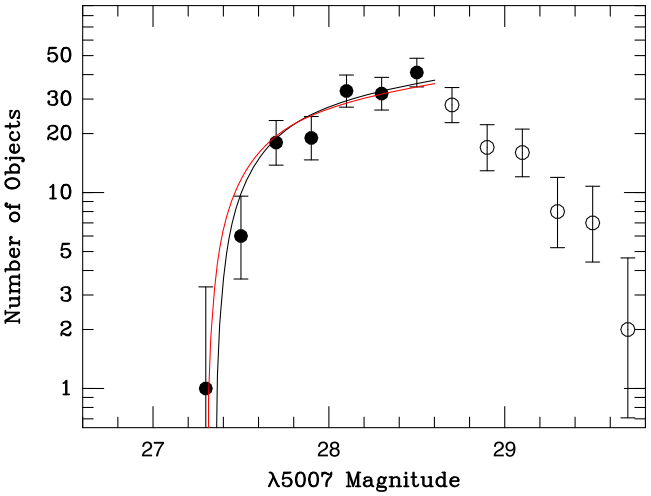

Figure 41. The observed PNLF for the Antennae galaxy binned into 0.2 mag intervals. Open circles denote data beyond the completeness limit; the error bars are from small number counting statistics (Gehrels 1986). The red curve shows the best fit to Equation (2) when PN1 is included in the analysis; the black curve shows the best fit when this one object is excluded. The two distance moduli differ by 0.048 mag.

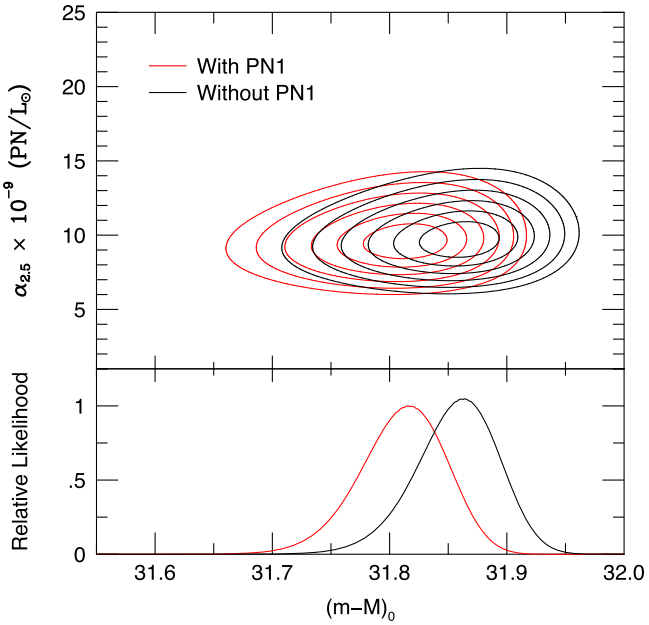

Figure 42. The top panel shows the results of the maximum-likelihood solution for the Antennae galaxy. The abscissa is the galaxy's true distance modulus, the ordinate is $\alpha_{2.5}$, the number of PNe within 2.5 mag of M^*, normalized to the amount of bolometric light sampled. The contours are drawn at 0.5σ intervals. The red contours are for the analysis that includes PN1, while the black contours show the likelihoods without the object. As the marginalization in the bottom panels shows, the difference in the solutions is ∼0.05 mag.

fluke, possibly due to the zero-point differences between the different MUSE pointings.

One final issue to keep in mind is that some of the dust associated with the NGC 4038/39's starburst regions may have been forced outward over the body of the galaxy by the tidal forces associated with the interaction. In such a scenario, this dust could extinct some of the PNe and cause an overestimate of the galaxy's distance. The fact that our PNLF distance to the system is slightly larger than those produced by the TRGB and Cepheid techniques lends support for this internal extinction hypothesis.

5.15. NGC 4365

The giant E3 elliptical galaxy NGC 4365 is the central member of Virgo's W′ group, roughly 6 Mpc behind the system's central core (Blom et al. 2014). The galaxy is a popular target for studies of extragalactic globular clusters, and it has been analyzed kinematically with the aid of the Planetary Nebula Spectrograph (Pulsoni et al. 2018). The published SBF distances to the galaxy span the range of $16.9 < D < 24.4$ Mpc, with the latest SBF measurement placing the galaxy at 23.1 Mpc (Blakeslee et al. 2009).

There is a single MUSE data cube of NGC 4365 in the ESO archive (ID: ADP.2016-06-07T11:11:26.095, PI: L. Coccato, Program ID: 094.B-0225). The exposure, which is centered on the galaxy's nucleus (see Figure 43), has an exposure time of 2343 s, and an image quality of 0.″76 at [O III] λ5007.

Our DELF analysis initially found 115 pointlike [O III] sources in the MUSE data cube; however, upon closer inspection of their spectra, 51 were excluded as either spurious objects (i.e., too faint to meet the detection criteria) or some

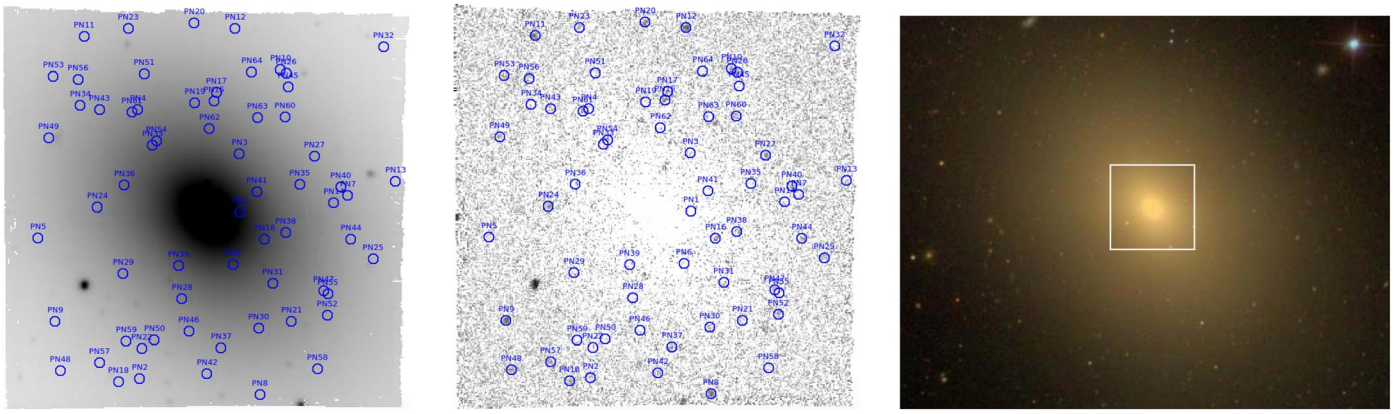

Figure 43. NGC 4365. Left: thumbnail off-band and difference images derived from the MUSE data cube. The blue circles show the positions of the PN candidates. Right: a broadband image with the MUSE field outlined in white. (Credit: SDSS DR14). A high-resolution image of the off-band and difference images is available online. The animation (available online) begins with the off-band image and then steps through the MUSE layers centered on the galaxy's redshifted [O III] wavelength to show how all emission-line objects, especially the PNe, rise and fall in brightness with wavelength.

(An animation of this figure is available.)

type of interloper. That left us with 64 PN candidates, with ∼50 in the top ∼1 mag of the PNLF.

As illustrated in Figure 43, only five of these detections were made in the galaxy's central ∼12″, an area that contains ∼35% of the light falling on the MUSE frame. This is not unexpected, as faint-object detections are severely incomplete against a bright, rapidly varying background. We therefore eliminate the region and its PNe from the analysis.

Interestingly, one of the excluded objects is PN1, a source that is 0.37 mag brighter than any other PN candidate in the galaxy. PN1 is located just 5.″1 from NGC 4365's nucleus, on an isophote with an R-band surface brightness of 17.2 mag arcsec^{-2} (Lauer 1985). If we assume a color of $(V-R)=0.60$ (Buta & Williams 1995) and a distance of 24 Mpc (Blakeslee et al. 2009), then Equations 3, 4, and 5 of Chase et al. (2023) imply that there is a ∼30% chance that the observed [O III] flux is formed from the emission of multiple sources. In fact, a careful inspection of the narrowband images made from the MUSE data cube reveals that the position of PN1 shifts slightly (by 0.″34) between the wavelengths of 5021.5 and 5024.0 Å. This supports the hypothesis that the [O III] flux of PN1 is produced by multiple superposed sources. Thus, the extreme luminosity of the source is not surprising and further justifies its rejection in the PNLF analysis.

The luminosity function of PNe outside the central 12″ of NGC 4365 is shown in Figure 44. The function is very well defined and shows no obvious deviation from the empirical law of Equation (2): the PN number counts decline rapidly to zero at magnitudes brighter than $m_{5007}\sim 27.2$, and there is no evidence for the existence of any overluminous objects. Although the data are only complete over the brightest ∼0.8 mag of the luminosity function, the data produce a very precise measure of distance.

To fit the PN magnitudes of Figure 44, we used the surface photometry of Lauer (1985) and Michard & Simien (1988), and the kinematic data of Foster et al. (2016) to estimate the amount of galaxy light and the line-of-sight velocity dispersion at every location in the data cube. The former measurements imply that the MUSE survey contains $V\sim 10.8$ of galaxy light; the latter quantities range from ∼225–207 km s^{-1}. (Both values exclude the central 12″ of the galaxy.) We then applied the algorithms of Chase et al. (2023) to derive the likelihood

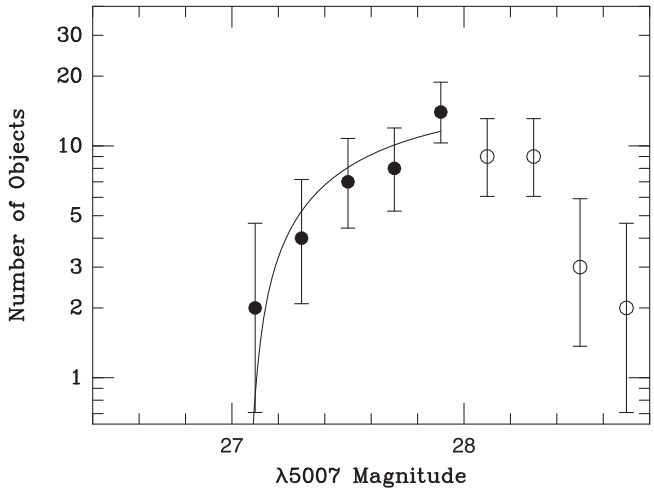

Figure 44. The observed PNLF for NGC 4365 binned into 0.2 mag intervals. Open circles denote data beyond the completeness limit; the error bars reflect the small number counting statistics (Gehrels 1986). The black curve shows Equation (2) shifted by the best-fit apparent distance modulus of $(m-M)=31.61$.

contours of Figure 45. Assuming a foreground reddening of $E(B-V)=0.02$, the resultant distance modulus to the system is $(m-M)_0 = 31.55^{+0.05}_{-0.08}$.

The systematic component of NGC 4365's error budget is quite low, as the data cube contains a bright and well-behaved PSF star. (The formal error on the aperture correction is just 0.002 mag.) If we assume a nominal 3% error due to the MUSE data cube's flux calibration, then the distance modulus to the galaxy becomes $(m-M)_0 = 31.55^{+0.06}_{-0.09}$ or $20.4^{+0.6}_{-0.8}$ Mpc. This value is on the low end of the range of SBF results, but consistent with the known zero-point offset between the two distance scales, which can be as high as 15% (Ciardullo et al. 2002).

5.16. NGC 4418

NGC 4418 (also known as NGC 4355 and IRAS 12243-0036) is a lenticular galaxy (Hubble type S0/a), with unusually luminous IR emission and mid-IR silicate absorption features that indicate a bright, but deeply obscured nucleus. The nature

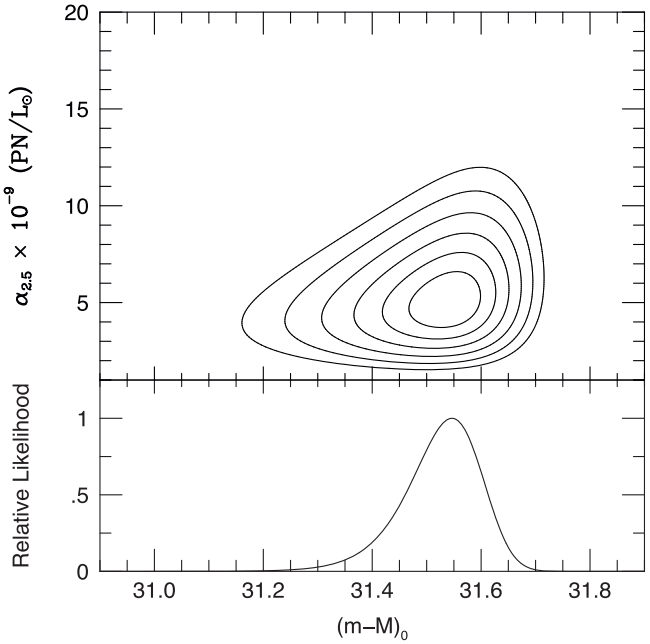

Figure 45. The upper panel shows the results of the maximum-likelihood solution for NGC 4365. The abscissa is the galaxy's true distance modulus, the ordinate is the number of PNe within 2.5 mag of M^*, normalized to the amount of bolometric light sampled, and the contours are drawn at 0.5σ intervals. The lower panel marginalizes over the PN/light variable.

of the nuclear region (starburst or AGN) is unclear, but evidence from radio data suggests the presence of a compact super-star cluster with intense star formation (Varenius et al. 2014). The only distances available to the system come from a single Tully–Fisher analysis, which places the galaxy ∼22 Mpc away (Theureau et al. 2007).

One promising MUSE-DEEP data cube exists in the ESO archive (archive ID: ADP.2020-02-13T10:53:27.677, PI: F. Stanley, Program ID: 0104.B-0668); these data have an exposure time of 5999 s, an image quality of 0.″89 at 5007 Å, and a position centered on the galaxy's nucleus (see Figure 46). Our examination of the DELF images created from the data cube resulted in a sample of 56 PN candidates, of which 47 survived spectral examination.

The locations of NGC 4418's PN candidates are shown in Figure 46. Within the 11″ semimajor axis isophote, there are no PN candidates; this reflects the effect that the region's high surface brightness has no PN detections. The PNLF of the objects outside this radius is shown in Figure 47.

NGC 4418's PNLF is not as well populated as some of the other galaxies in this study. The data start to become incomplete ∼0.7 mag down the PNLF, and there are only ∼24 PN detections brighter than this limit. Consequently, stochasticity is an issue. For example, PN1 is 0.27 mag brighter than any other planetary. In galaxies with a well-populated PNLF, such a gap might be indicative of an anomaly. Here, it is perfectly consistent with expectations. In fact, a K-S test prefers a fit that includes PN1.

NGC 4418 has no published surface photometry, nor are there any measurements of the disk's line-of-sight velocity dispersion. We compute the former using continuum measurements from the MUSE spectra; after excluding the galaxy's inner ∼11″, we estimate that $V \sim 13.6$ of light is contained in the survey region. For the latter we adopt 75 km s^{-1} throughout the galaxy; this number is much less than the minimum velocity separation needed to deblend two sources and is consistent with expectations for the velocity ellipsoid of a disk galaxy.

Figure 48 displays the likelihood contours for NGC 4418. The distortion of the lowest-level contours reflects the possibility that PN1 may be a superposition: the galaxy continuum underlying the PN is relatively bright and the object is the most luminous PN in the sample. However, as the marginalized probability curve in the lower panel of the figure indicates, the possibility has almost no effect on the most likely distance to the galaxy: for a foreground reddening $E(B-V) = 0.02$ (Schlafly & Finkbeiner 2011) we obtain $(m-M)_0 = 32.59^{+0.07}_{-0.10}$. When we include the small systematic component to the error budget (as shown in Figure 46, the error on the aperture correction error is minimal due to the presence of a bright field star), the distance modulus becomes $(m-M)_0 = 32.59^{+0.07}_{-0.10}$, or $32.9^{+1.2}_{-1.5}$ Mpc. This places the galaxy among the most distant objects ever studied by the PNLF technique, and well beyond the galaxy's Tully–Fisher estimate. The observation demonstrates what is now possible with the MUSE instrument.

We do note that, since the galaxy is a bright IR source, it is possible that some of the emitting dust could be distributed across the face of the galaxy. So some of the PNe may be attenuated by this component. In that case, our PNLF distance would be an overestimate. Assuming that this is not the case, the galaxy provides an opportunity for direct measurement of the Hubble constant, as the system is distant, relatively isolated, and has an unusually bright field star projected onto its body for a precise measure of the aperture correction (see Section 6.4).

5.17. NGC 4472 (M49)

The E2 giant elliptical NGC 4472 is the brightest galaxy in the Virgo cluster and is at the center of the Virgo B subclump. Previous PNLF measurements have placed this galaxy at a distance of 13.9 Mpc (Jacoby et al. 1990), 14.4 Mpc with a new calibration from the HST key project (Ferrarese et al. 2000), and 18.1 Mpc (Hartke et al. 2017). NED lists 22 SBF distances for the system, ranging from 14.3–17.8 Mpc.

There are a total of nine relatively shallow MUSE data cubes of NGC 4472 in the ESO archive (Program ID: 095.B-0295 PI: J. Walcher) that are provided as three mosaics; each combines three MUSE pointings in one cube. We list these data in Table 9 and show their locations in Figure 49. Despite the short exposure times, we managed to identify and measure 81 of the galaxy's PN candidates with the DELF technique.

Figure 50 displays the PNLF of the objects. In the figure, we have excluded the PNe in the central ∼40″ of the galaxy, since, as Figure 49 illustrates, the limited depth of the data made PN detections in this high surface brightness region difficult. Even outside this radius, the PN luminosity function is not especially deep, as the data only extend ∼0.7 mag fainter than PNLF's bright-end cutoff. This is just deep enough to determine a robust distance to the galaxy.

To determine the amount of light underlying the location of each PN, we used the surface photometry of Cohen (1986); outside the 40″ radius, the total amount of galaxy light falling onto the MUSE data cubes is $V \sim 9.5$ mag. The stellar velocity dispersion, as a function of galactic radius, was taken from Veale et al. (2017). For the PNe being analyzed here, this quantity ranges from ∼230 to ∼255 km s^{-1}. Effectively, this means that even if two PNe are spatially colocated on the same

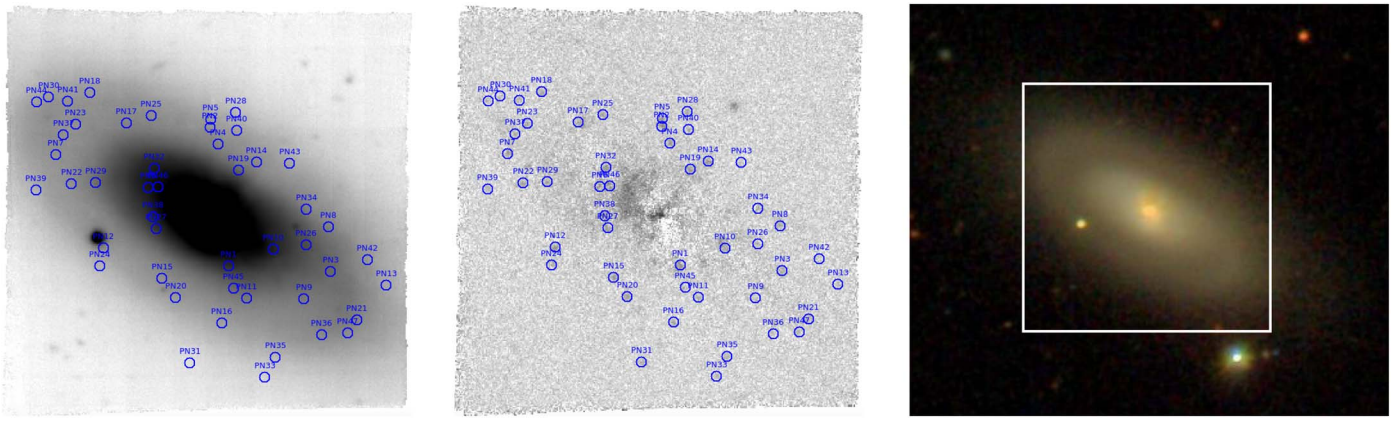

Figure 46. NGC 4418. Left: thumbnail off-band and difference images derived from the MUSE data cube. The blue circles show the positions of our PN candidates. Right: a broadband image with the location of the MUSE data cube outlined in white. (Credit: SDSS DR14). A high-resolution image of the off-band and difference images is available online. The animation (available online) begins with the off-band image and then steps through the MUSE layers centered on the galaxy's redshifted [O III] wavelength to show how all emission-line objects, especially the PNe, rise and fall in brightness with wavelength.

(An animation of this figure is available.)

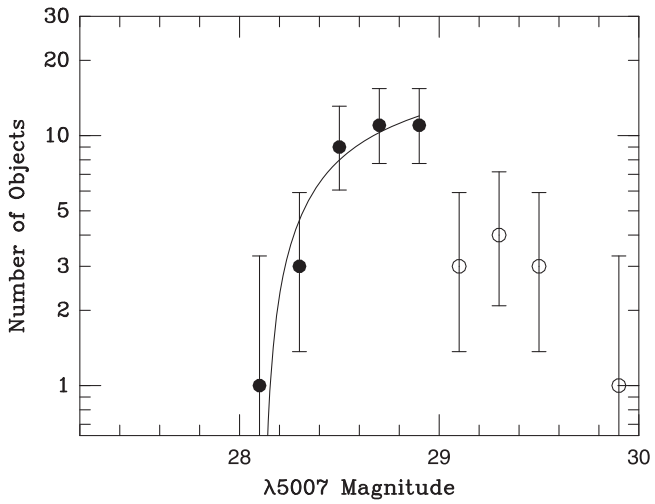

Figure 47. The observed PNLF for NGC 4418 binned into 0.2 mag intervals. Open circles denote data beyond the completeness limit; the error bars show the small number counting statistics (Gehrels 1986), and the curve shows Equation (2) shifted by the best-fit apparent distance modulus of $(m - M) = 32.66$.

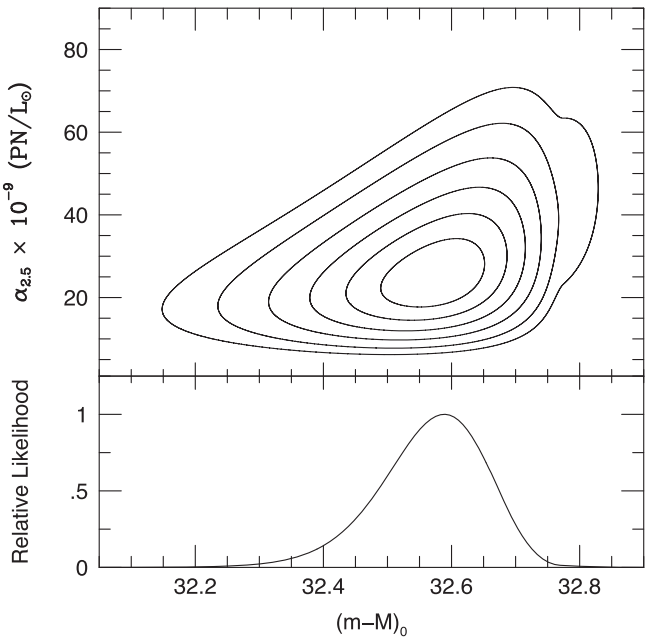

Figure 48. The top panel shows the results of the maximum-likelihood solution for NGC 4418. The abscissa is the galaxy's true distance modulus, the ordinate is $\alpha_{2.5}$, the number of PNe within 2.5 mag of M^*, normalized to the amount of bolometric light sampled. The contours are drawn at 0.5σ intervals. There is a slight possibility that the galaxy's brightest PN candidate is the superposition of two sources; this is reflected in the *bump* in the outermost likelihood contour.

location on the sky, there is better than a 50% chance that the flux from the two objects can be disentangled via their differing radial velocities. This is consistent with a visual inspection of Figure 50: our PNLF displays no evidence for any superposed or overluminous objects.

The aperture correction error for this data set is particularly difficult to assess. The $3' \times 3'$ region surveyed by MUSE is composed of three mosaics, and each mosaic consists of data from three MUSE pointings. Consequently, assumptions must be made as to whether the aperture correction derived from any given star is applicable to the faint sources found in other regions of the same mosaic. Moreover, the short exposure time means that the data are rather shallow, leading to low S/N measurements. Mosaic M1 does contain one very bright star that yields a formal aperture correction error of 0.001 mag, and the photometry of two other stars in the field yields corrections that are consistent with that from the bright star. At least in the M1 mosaic, the zero-point error appears to be dominated by the uncertainty of the MUSE flux calibration, rather than our ability to define the point-source aperture correction.

Table 9
Data Cubes for NGC 4472

Field	Archive ID	Exp Time (s)	Seeing (5007 Å)
M1	ADP.2016-06-21T00:50:22.928	626	0.″72
M2	ADP.2016-07-11T13:38:27.884	623	0.″82
M3	ADP.2016-06-21T00:31:05.332	621	0.″93

In contrast, M2 covers the high surface brightness region around NGC 4472's nucleus, where faint pointlike sources are difficult to measure. In this mosaic, the formal aperture

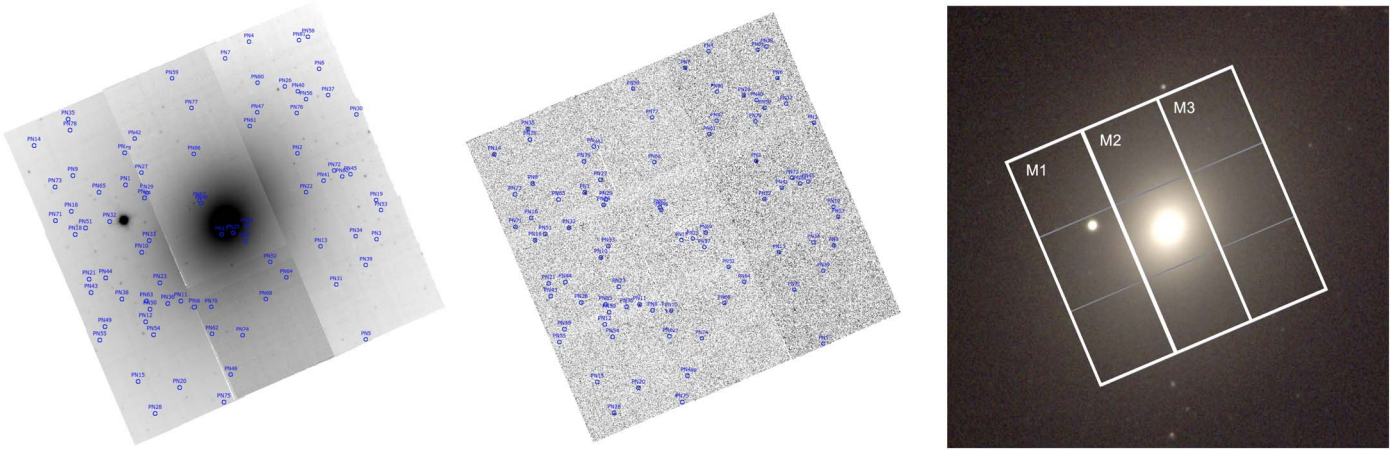

Figure 49. NGC 4472. Left: thumbnail off-band and difference images derived from the MUSE data cubes. The blue circles denote the PN candidates. Right: a broadband image with the MUSE data cubes outlined in white. (Credit: NOIRlab/NSF/AURA). A high-resolution image of the off-band and difference images is available online. The animation (available online) begins with the off-band image and then steps through the MUSE layers centered on the galaxy's redshifted [O III] wavelength to show how all emission-line objects, especially the PNe, rise and fall in brightness with wavelength.

(An animation of this figure is available.)

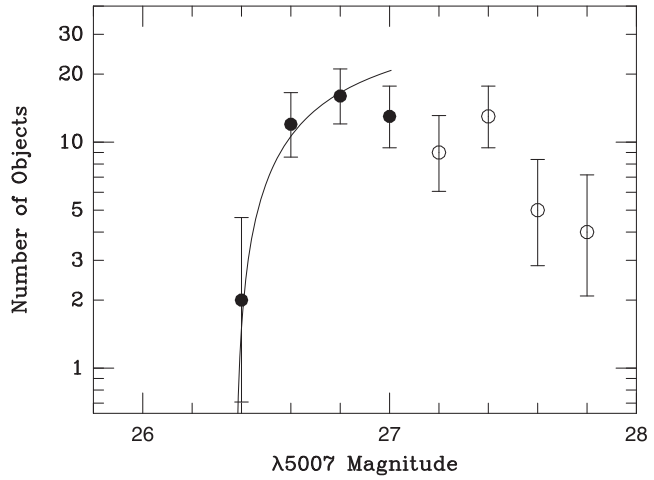

Figure 50. The observed PNLF for NGC 4472 binned into 0.2 mag intervals. Open circles denote data beyond the completeness limit; the error bars illustrate the uncertainties of small number counting statistics (Gehrels 1986). The curve shows Equation (2) shifted by the best-fit apparent distance modulus of $(m - M) = 30.91$.

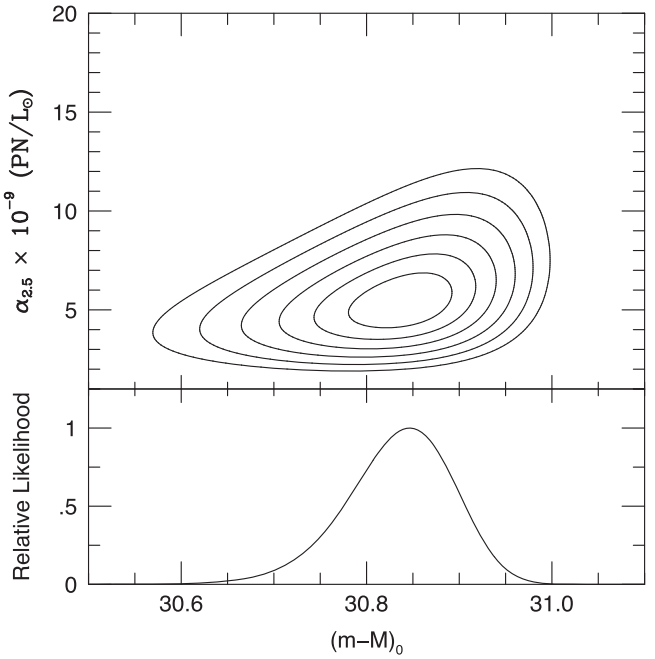

Figure 51. The top panel shows the results of the maximum-likelihood solution for NGC 4472. The abscissa is the galaxy's true distance modulus, the ordinate is $\alpha_{2.5}$, the number of PNe within 2.5 mag of M^*, normalized to the amount of bolometric light sampled. The contours are drawn at 0.5σ intervals. The bottom panel marginalizes this distribution over the PN/light variable.

correction errors may be as large as 0.17 mag. M3 lies somewhere in the middle: our value for the aperture correction seems to be reasonably accurate, although the measurement largely depends on one well-measured object.

Of the brightest 50 PNe in our sample, only three are contained in M2, and none are among the brightest 16 objects. This suggests that our estimate of the aperture correction may be underestimated. However, as pointed out in Section 5.10, such an error will likely not affect our derived distance to the galaxy. We therefore conservatively assign 0.06 mag as the zero-point error of our PNLF measurements.

The results of our PNLF fit to NGC 4472 are shown in Figure 51. Despite the limited depth of the survey, which restricted the number of PNe in our statistically complete sample to 43, the data are very well fit to the curve of Equation (2). Our distance modulus to NGC 4472 for $E(B - V) = 0.02$ is therefore $(m - M)_0 = 30.85^{+0.08}_{-0.09}$, or $14.8^{+0.5}_{-0.6}$ Mpc.

For comparison, the almost two dozen SBF distances derived for the galaxy give slightly larger values ($30.78 \leqslant (m - M)_0 \leqslant 31.25$) with the most recent value of $(m - M)_0 = 31.12$ falling on the high side of the interval (Blakeslee et al. 2009). This offset is consistent with the historical difference between the two distance methods. Somewhat curiously, there are no TRGB distance measurements to the galaxy.

Our MUSE-based measurement of $14.8^{+0.3}_{-0.4}$ Mpc is slightly more distant, but still consistent, with the first PNLF distance to the galaxy (Jacoby et al. 1990): when scaled to today's zero-point, those authors inferred a value of 14.3 ± 0.4 Mpc. However, our new value is significantly smaller than the

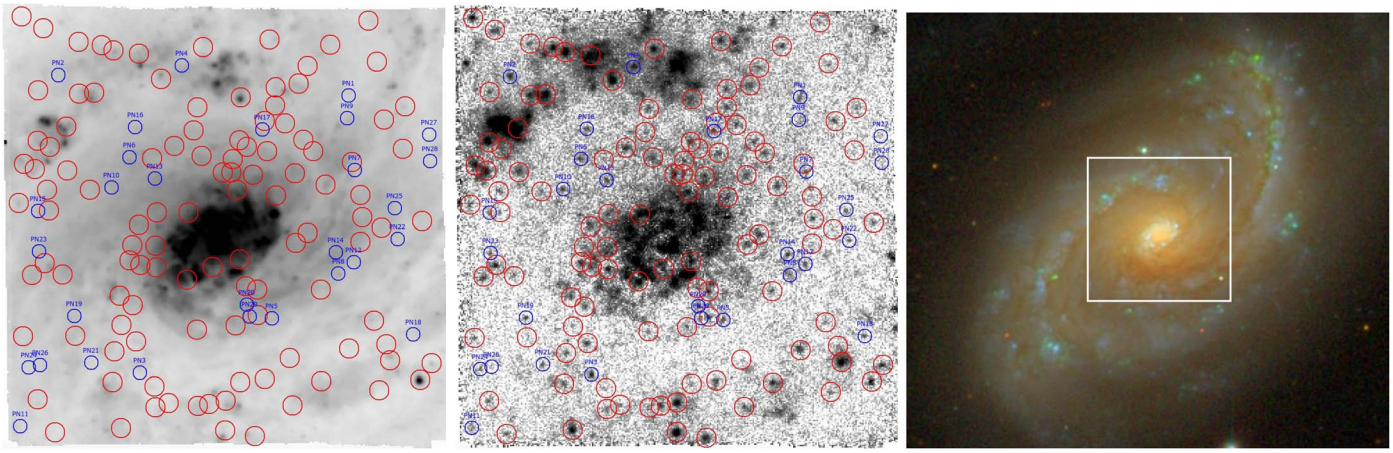

Figure 52. NGC 5248. Left: thumbnail off-band and difference images derived from the MUSE data cube. The PN candidates are circled in blue; likely H II and other interlopers are shown in red. Right: a broadband image with the location of the MUSE field outlined in white. (Credit: SDSS DR14). A high-resolution image of the off-band and difference images is available in online. The animation (available online) begins with the off-band image and then steps through the MUSE layers centered on the galaxy's redshifted [O III] wavelength to show how all emission-line objects, especially the PNe, rise and fall in brightness with wavelength.

(An animation of this figure is available.)

results of Hartke et al. (2017), who used PN observations from Subaru's Suprime Cam to derive a distance of 18.1 ± 0.6 Mpc. These on-band/off-band data extend much deeper than the MUSE spectra (to $m_{5007} = 28.8$), contain many more (624) PNe, and extend over a much wider field of view than the MUSE observations. We hypothesize that about half the discrepancy is due to a metallicity gradient, with the Hartke et al. (2017) observations principally sampling the bluer outer envelope of the galaxy, while MUSE (and the Jacoby et al. 1990 study) are drawn from the system's inner regions. In a metal-poor environment, a PNLF shift of ∼0.2 mag toward fainter values is possible (see, for example, Dopita et al. 1992).

5.18. NGC 5248

NGC 5248 is a barred SAB(rs)bc galaxy projected within the Virgo III group, east of the Virgo cluster core. The galaxy's distance is uncertain: while the system has been measured using the Tully–Fisher relation, the results span a wide range of values, from ∼10 Mpc (e.g., Bottinelli et al. 1984; Sorce et al. 2014) to ∼22 Mpc (Ekholm et al. 2000). Given the complexity of the region, none is preferred.

Due to its prominent bar and nuclear ring, the galaxy has been targeted by MUSE as part of the TIMER survey (Gadotti et al. 2019). Neumann et al. (2020) have used these data to create Hα maps of the galaxy's central ring/bar region with the goal of exploring the area's star formation rate history. These authors consider NGC 5248 to be peculiar with respect to other galaxies of its type, with strong star formation in a very large nuclear disk and attached spiral-like features.

We retrieved the archival MUSE-DEEP data cube (ESO Archive ID: ADP.2017-06-14T09:12:09.276, PI: D. Gadotti, Program ID: 097.B-0640) obtained from two observations with an effective exposure time of 3411 s, and 0.″76 seeing at 5007 Å. This pointing is centered on the galaxy's nucleus and includes the system's nuclear ring, two spiral arms, and a number of prominent dust lanes (see Figure 52). Our difference image confirms the presence of strong emission lines throughout the field, and out of an initial sample of 143 candidates, 114 had to be rejected as H II regions or SNRs (the red circles in the figure). The final sample of PN candidates therefore contains only 29 objects, with 15 being in the top magnitude of the luminosity function.

NGC 5248's cumulative PNLF is plotted in Figure 53. There are two immediate features to note. The first is the luminosity of PN1, which is 0.42 mag brighter than the next brightest object. For galaxies with larger numbers of PNe, such a difference would be highly improbable. Considering NGC 5248's sparsely populated PNLF, though, the possibility that PN1 is normal cannot be discounted.

The second important property of the distribution is the depth of the survey. If PN1 is overluminous, i.e., if PN1's luminosity is not well described by the luminosity function defined by Equation (2), then the statistically complete sample of PNe only extends ∼0.5 mag down the PNLF. While this lack of depth does not preclude a PNLF distance from being obtained, it does lessen the reliability of the result.

Given the complex morphology of NGC 5248's inner regions, we did not attempt to derive the galaxy's brightness distribution from the literature; instead, we used the information contained within the MUSE data cube to estimate the continuum brightness at the location of each PN. Similarly, since the line-of-sight velocity dispersion in the inner regions of the galaxy is much smaller than MUSE's spectral resolution (e.g., Fabricius et al. 2012; Rosado-Belza et al. 2020), we simply assume $\sigma = 75$ km s^{-1} throughout the region.

As stated above, the only previous distance estimates for this galaxy come from the Tully–Fisher relation. Only one of these determinations places the galaxy beyond 17 Mpc (Ekholm et al. 2000), and most prefer distances on the nearside of Virgo (e.g., Bottinelli et al. 1984; Theureau et al. 2007; Sorce et al. 2014). Our PNLF values are clearly inconsistent with such a location; they agree more with the larger distances.

If we include PN1 in our PNLF analysis, then for an $E(B-V) = 0.02$, our maximum-likelihood analysis yields a distance modulus of $(m - M)_0 = 31.37^{+0.06}_{-0.13}$, while assigning less than a 0.4% probability that the overluminous PN is a blend of two sources. However, if we accept that the object is not the result of a superposition and adopt the galaxy's most likely distance modulus, then a K-S test excludes the possibility that the observed PNe are drawn from the distribution defined by Equation (2) at the 99% confidence level. Alternatively, if

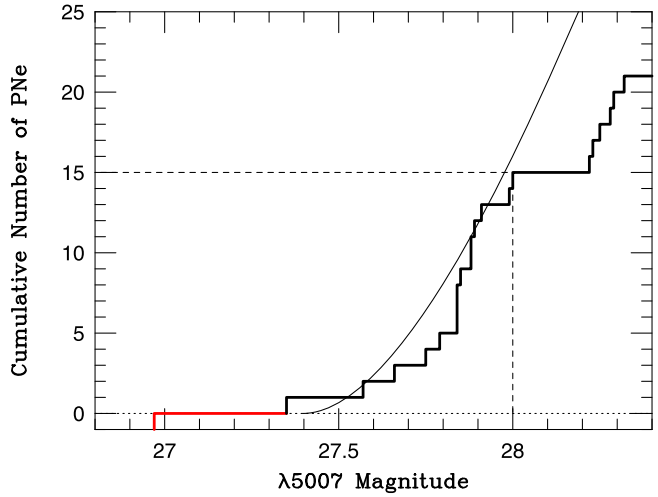

Figure 53. The cumulative luminosity function for PNe in NGC 5248. The dark line shows the observed data and the curve is Equation (2) shifted to the most likely apparent distance modulus of $(m - M)_0 = 31.93$. The dark red line shows PN1 and the dashed line denotes where incompleteness begins to affect the detections. Data brighter than this are consistent with being drawn from the empirical function. A K-S test excludes the inclusion of PN1 at the 99% confidence level.

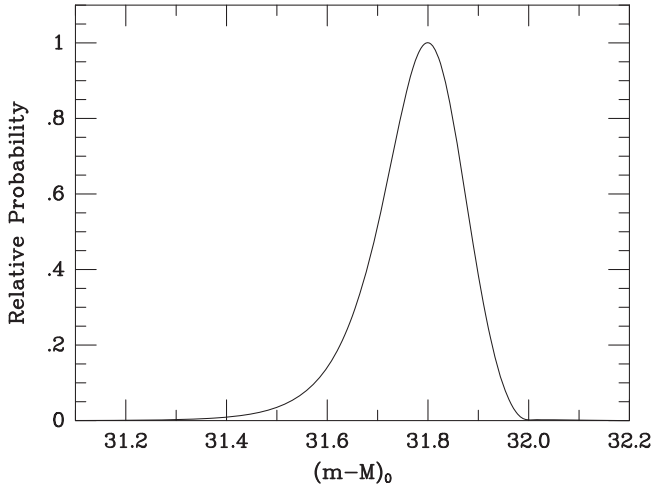

Figure 54. The results of the maximum-likelihood analysis for NGC 5248. The abscissa is the galaxy's true distance modulus, the ordinate the relative likelihood of the solution. PN1 has been excluded from the analysis. This distance is consistent with the Tully–Fisher-based estimate of Ekholm et al. (2000).

we remove PN1 from the sample, then the distance to NGC 5248 increases to $(m - M)_0 = 31.80^{+0.07}_{-0.10}$, and the hypothesis that the PNe are drawn from the empirical function cannot be refuted. On that basis, we adopt the larger distance to the galaxy. The distribution of likelihoods for this assumption is shown in Figure 54.

Since the MUSE data cube of the galaxy contains a bright star, the error associated with the photometric aperture correction is very small, formally 0.005 mag. Thus, the systematic component of the error budget is dominated by the ∼0.03 mag uncertainty in the MUSE flux calibration. Our derived distance to the galaxy is then $(m - M)_0 = 31.80^{+0.08}_{-0.11}$, or $22.9^{+0.8}_{-1.1}$ Mpc.

5.19. NGC 6958

NGC 6958 is an isolated early-type galaxy, classified as S0 according to Sandage & Bedke (1994) and Laurikainen et al. (2010), but misclassified as a cD by de Vaucouleurs et al. (1991). Thater et al. (2022) used MUSE data of the galaxy to measure the mass of its supermassive black hole via stellar kinematics. Their study also used the dynamical scaling relations for early-type galaxies to place the system at a distance of 35 ± 8 Mpc. If this is correct, then a PNLF measurement would be challenging. On the other hand, it would also offer us an opportunity to apply the technique outside the Local Supercluster in a region where the Hubble flow is relatively unperturbed (see Section 6.4).

We retrieved the data cube of a science verification observation from the ESO Archive (ID: ADP.2017-11-09T16:25:30.895, PI: D. Krajnovic, Program ID: 60.A-9193). The metadata for the observation lists an exposure time of 1906 s and a seeing of 0.″96. However, we have sometimes found discrepancies between the recorded metadata and our own PSF analysis, and indeed, Thater et al. (2022) measured the data cube's PSF FWHM to be 0.″75 at 5000 Å, and ⩽0.″6 at wavelengths longward of 7400 Å. Unfortunately, this adaptive optics-supported observation was secured under poor weather conditions, so the data were not optimal.

Despite this shortcoming, we were able to detect 64 PN candidates with our DELF technique. Further inspection confirmed that 28 had spectra consistent with that of a PN. The fact that more than half of the initial candidates appear to be either H II regions or SNRs (red circles in Figure 55) supports the classification of the galaxy as a lenticular, rather than a cD system. Furthermore, the difference image reveals rotation or outflow of the diffuse emission component.

Figure 56 shows the PNLF of NGC 6958. Clearly, the data are limited: despite the bin size being increased to 0.25 mag, no interval contains more than seven objects. Similarly, as the data only extend ∼0.5 mag down the luminosity function, the shape of the exponential cutoff is ill-defined, which means the PNLF technique may be susceptible to systematic errors. Most importantly, even for the brightest objects, the photometric uncertainties associated with the PN measurements are greater than 0.15 mag. In other words, the S/N of even the brightest detections is only ∼7. Thus, incompleteness may be non-negligible, even at the brightest magnitudes.

Nevertheless, we fit the data to Equation (2), as per the previous galaxies. Since NGC 6958 has no published surface photometry or kinematic measurements, we used the MUSE continuum spectroscopy for the former and adopted 75 km s^{-1} for the line-of-sight stellar velocity dispersion. As a lenticular system with an inclination of ∼45°, the latter value is a reasonable estimate for the stellar kinematics. We also excluded all data from the central ∼11″ of the galaxy, where the surface brightness was too bright for PN detections. This left us with $V \sim 12.2$ of galaxy light to study.

Figure 57 shows the results of our analysis. Two issues stand out. The first is that, for the best-fit solutions, $\alpha_{2.5}$, the PN per unit light ratio, is lower than any other galaxy considered in this study. This suggests that we are missing PNe, even at the bright end of the luminosity function. In such a situation, the PNLF tends to overestimate distance. The second issue is that our distance determination is not very precise, with the 3σ error contours extending over almost two magnitudes in distance modulus. Again, this is due to the small number of PN detections and the limited depth of the survey.

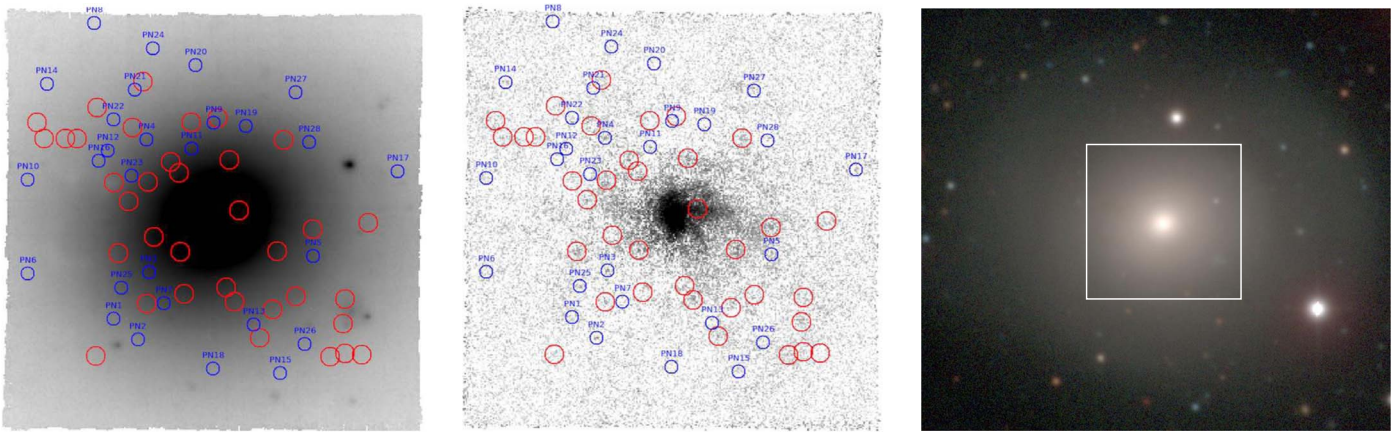

Figure 55. NGC 6958. Left: thumbnail off-band and difference images derived from the MUSE data cube. Blue circles show the positions of the PN candidates; the red circles denote H II regions and other interlopers. Right: a broadband image with the location of the MUSE pointing outlined in white. (Credit: CGS). A high-resolution image of the off-band and difference images is available online. The animation (available online) begins with the off-band image and then steps through the MUSE layers centered on the galaxy's redshifted [O III] wavelength to show how all emission-line objects, especially the PNe, rise and fall in brightness with wavelength.

(An animation of this figure is available.)

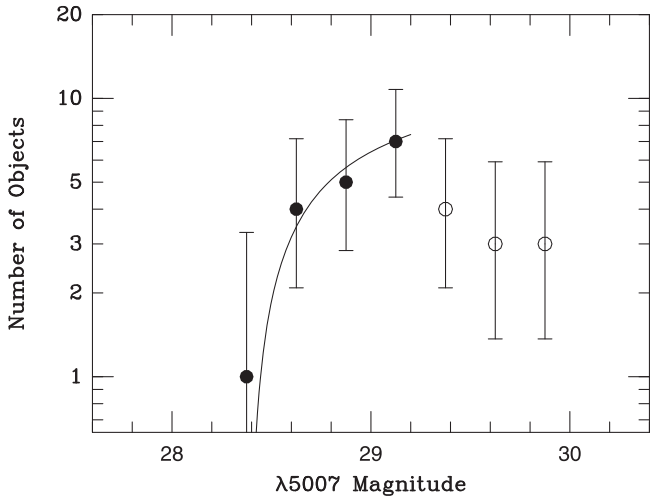

Figure 56. The observed PNLF for NGC 6958 binned into 0.25 mag intervals. Although incompleteness likely affects our entire survey, we only consider PNe brighter than $m_{5007} = 29.2$ in our fit. Fainter objects are denoted by open circles. The error bars illustrate the uncertainties of small number counting statistics (Gehrels 1986). The curve shows Equation (2) shifted by the best-fit apparent distance modulus of $(m - M)_0 = 32.80$.

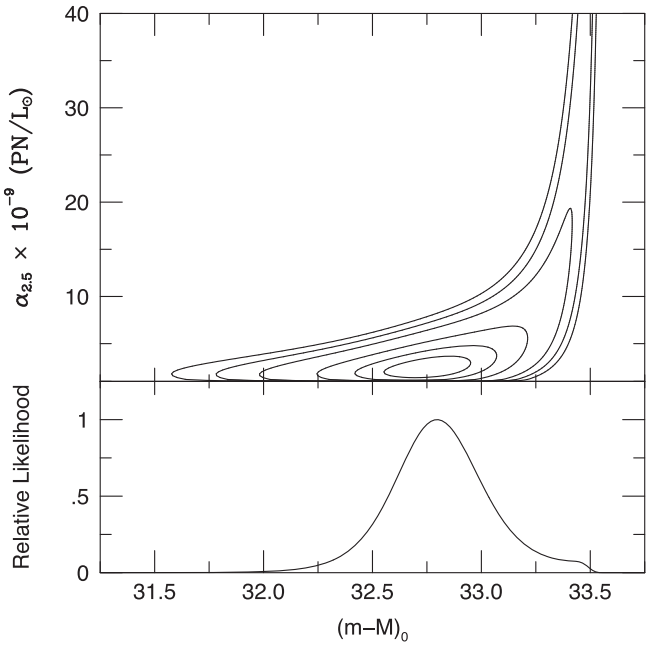

Figure 57. The top panel shows the results of the maximum-likelihood solution for NGC 6958. The abscissa is the galaxy's true distance modulus, the ordinate is $\alpha_{2.5}$, the number of PNe within 2.5 mag of M^*, normalized to the amount of bolometric light sampled. The contours are drawn at 0.5σ intervals. The bottom panel marginalizes this distribution over the PN/light variable. The low value of $\alpha_{2.5}$ is most likely due to incompleteness in our survey.

Formally, our distance to the system is $(m - M)_0 = 32.80^{+0.24}_{-0.21}$ ($36.2^{+4.3}_{-3.3}$ Mpc) for a foreground reddening of $E(B - V) = 0.04$. Perhaps fortuitously, this value is nearly identical to the Tully–Fisher distance of 36.4 Mpc published by Theureau et al. (2007). Nevertheless, it is fair to conclude that with better image quality and longer exposure times, this object would be well within reach of the PNLF technique. Although our distance exhibits larger errors than usual and may be a slight overestimate due to the underpopulated bright end of the PNLF, it is one of the few targets in this study with a very good aperture correction star. Thus, it is a good candidate for a future program for a PNLF measurement of the Hubble constant (see Section 6.4).

5.20. MCG-06-08-024 (FCC 090)

MCG-06-08-024, also listed as FCC 090, is an early-type dwarf galaxy in the Fornax cluster with a Hubble classification of SA0 (Figure 58). It is known from ALMA observations to harbor a disturbed gas reservoir with a molecular gas tail (Zabel et al. 2020). Distance estimates from the globular cluster luminosity function and SBFs range from 17–20.5 Mpc, consistent with the system being a Fornax cluster member. We note that FCC 090 is not listed in the sample of 21 Fornax early-type galaxies whose PNLF was studied by Spriggs et al. (2021); hence, it could be an interesting test case to probe the superior sensitivity of our technique. However, as a dwarf galaxy, we would not expect the galaxy to contain a large population of PNe.

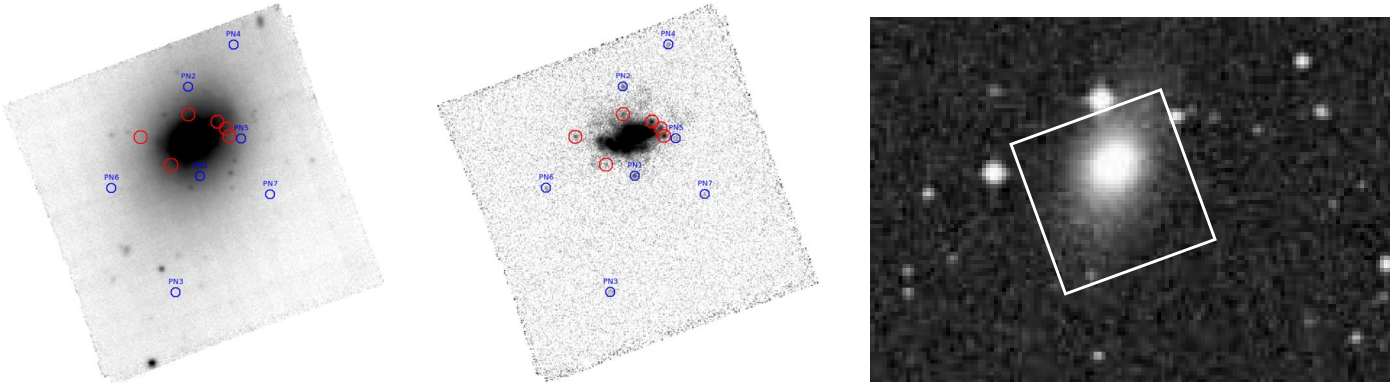

Figure 58. MCG-06-08-024. Left: thumbnail off-band and difference images derived from the MUSE data cube. The blue circles show PN candidates; the red markers show interloping objects. Right: a broadband image outlining the location of the MUSE field. (Credit: ESO DSS1.) A high-resolution image of the off-band and difference images is available online. The animation (available online) begins with the off-band image and then steps through the MUSE layers centered on the galaxy's redshifted [O III] wavelength to show how all emission-line objects, especially the PNe, rise and fall in brightness with wavelength.

(An animation of this figure is available.)

We examined a MUSE-DEEP data cube (ESO Archive ID: ADP.2018-03-26T15:02:26.516, PI: M. Sarzi, Program ID: 296.B-5054) created from two exposures with a total effective exposure time of 4821 s and 0.″67 seeing. From an original list of 13 pointlike [O III] sources, six were eliminated based on their spectra. The two brightest objects, with $m_{5007} = 27.96$ and 28.54, have magnitudes that are roughly 1 mag fainter than the PNLF cutoff of other Fornax cluster galaxies. This precludes us deriving a useful distance estimate but it does allow us to place an upper limit on the system's distance of $<$30.8 Mpc.

6. Discussion

6.1. Distance Comparisons

With few exceptions, our PNLF distances agree very well with those of other PNLF results. We already have commented on one major disagreement with the Scheuermann et al. (2022) distance to NGC 1385 and a milder disagreement with the Hartke et al. (2017) measurement of NGC 4472.

A summary of our distances and those based on other methods is given in Table 10. Unfortunately, there is limited overlap between our heterogeneous set of galaxies culled from the MUSE archive and systems with reliable distances found by other techniques. NGC 4038/39 is the only galaxy in our sample with a Cepheid distance, and our PNLF analysis yields a distance that is 10%–27% larger, depending on which Cepheid value is selected (Riess et al. 2011; Fiorentino et al. 2013; Riess et al. 2016, 2022); we note, though, that the most recent Cepheid result yields the least disagreement. That is, the difference between the PNLF and Cepheid distances is similar to that of the Cepheid distances against themselves. Consequently, it is difficult to make any conclusions from the discrepancy.

A comparison of the distance to the six galaxies with TRGB measurements is equally problematic. The PNLF distance to the edge-on spiral NGC 253 is ∼54% greater than that found from the system's red giants; however, the sparseness of the luminosity function (less than 10 objects within 1 mag of M^*) and the possible effects of internal extinction, weaken confidence in the PNLF result. Conversely, for the more face-on spirals of NGC 1433 and 1512, the factor of ∼2 discrepancies between the PNLF and TRGB distances (Sabbi et al. 2018) is likely due to the galaxies' large population of AGB stars and the misidentification of the RGB tip. As for the three remaining galaxies, NGC 1404 (Hoyt et al. 2021), NGC 4038/9 (Jang & Lee 2015), and Paper I's measurement of NGC 628 (Sabbi et al. 2018) the two distance methods agree within +0.5%, +7%, and +8%, respectively, where the PNLF distances are always larger. This more encouraging result is consistent with previous TRGB–PNLF comparisons (e.g., Ciardullo 2012, 2022).

The richest area for a PNLF comparison is with the SBF method where we have 10 galaxies in common, eight in this paper and two in Paper I. On average, the PNLF distances are smaller by −6%, a systematic that has been known for decades and has usually been attributed to the effect of internal extinction in the calibrating galaxies (Ciardullo et al. 1993, 2002). Briefly stated, the PNLF and SBF respond to undetected attenuation in opposite ways: distances from the PNLF are underestimated, while those from the SBF are overestimated (due to the color term associated with the fluctuation magnitude). Since both methods are calibrated in the bulges of nearby spirals, but then applied to elliptical and lenticular systems, any internal attenuation in the calibration galaxies that is not present in the program systems will lead to a systematic offset in the distance scales. Notably, the −6% offset is less than that found in the older studies, lowering the requisite amount in attenuation in spiral bulges to less than $E(B-V) = 0.01$ mag.

Scheuermann et al. (2022) presented another approach to comparing PNLF distances to other methods in their Figure 9. In comparison to Cepheids and TRGB, their PNLF distances tended to be too large by ∼7%, but with significant scatter, due in large part to limited repeatability within each of those methods.

While it is premature to declare that the PNLF compares as well to other premium distance techniques as they do to each other, the results are quite promising. For the PNLF to be validated further, it is essential to obtain MUSE data cubes taken with absolute photometry of faint point sources in mind. This means (a) choosing fields with foreground stars bright enough to define the observation's PSF and aperture correction, (b) observing when the atmospheric seeing is good enough to support faint PN identifications, (c) ensuring that each data cube is taken under the best photometric conditions, and (d)

Table 10
PNLF Galaxy Distances

Galaxy	Number of PNe[a]	$(m-M)_0$	PN Distance (Mpc)	Other Distance (Mpc)	Notes
NGC 253	34/10	$28.66^{+0.12}_{-0.28}$	$05.4^{+0.3}_{-0.6}$	3.5 ± 0.1 (TRGB)	Possible dust within the galaxy
NGC 1052	86/50	$31.26^{+0.07}_{-0.08}$	$17.9^{+0.3}_{-0.6}$	18.0 ± 2.4 (SBF)	…
NGC 1326	55/20	$31.00^{+0.09}_{-0.13}$	$15.9^{+0.6}_{-0.9}$	…	Overluminous PN rejected
NGC 1351	102/45	$31.39^{+0.04}_{-0.08}$	$19.0^{+0.4}_{-0.7}$	19.2 ± 0.6 (SBF)	Overluminous PN rejected
NGC 1366	22/13	$31.39^{+0.11}_{-0.23}$	$19.0^{+1.0}_{-1.8}$	21.1 ± 3.0 (SBF)	…
NGC 1385	78/54	$31.99^{+0.11}_{-0.12}$	$25.0^{+1.4}_{-1.5}$	…	…
NGC 1399	232/164	$31.23^{+0.06}_{-0.07}$	$17.6^{+0.5}_{-0.6}$	21.1 ± 0.7 (SBF)	…
NGC 1404	124/64	$31.37^{+0.05}_{-0.08}$	$18.8^{+0.4}_{-0.6}$	18.7 ± 0.6 (TRGB), 20.4 ± 0.6, 20.2 ± 0.6 (SBF)	…
NGC 1419	21/12	$31.39^{+0.12}_{-0.27}$	$18.9^{+1.1}_{-2.5}$	22.9 ± 0.9 (SBF)	…
NGC 1433	258/160	$31.42^{-0.08}_{+0.07}$	$19.2^{+0.7}_{-0.7}$	…	Two overluminous PNe included
NGC 1512	210/144	$31.43^{+0.06}_{-0.06}$	$19.3^{+0.5}_{-0.6}$	11.7 ± 1.1 (TRGB)	Overluminous PN rejected
NGC 2207	3/0	…	<40	…	…
NGC 3501	6/0	…	<38	…	
NGC 4038/9	228/154	$31.82^{+0.07}_{-0.07}$	$23.1^{+0.7}_{-0.8}$	21.6 ± 0.5 (TRGB)	Antennae galaxies
…	…	…	…	18.1 ± 0.9, 20.4 ± 0.6, 21.0 ± 1.2 (CEPH)	…
NGC 4365	64/30	$31.55^{+0.06}_{-0.09}$	$20.4^{+0.6}_{-0.8}$	23.1 ± 0.8 (SBF)	
NGC 4418	47/24	$32.59^{+0.07}_{-0.10}$	$32.9^{+1.2}_{-1.5}$	…	Overluminous PN included
NGC 4472	67/43	$30.85^{+0.08}_{-0.09}$	$14.8^{+0.5}_{-0.6}$	15.9 ± 1.0 (SBF)	SBF is an average of 22 values in NED
NGC 5248	29/15	$31.80^{+0.08}_{-0.11}$	$22.9^{+0.8}_{-1.1}$	…	Overluminous PN rejected
NGC 6958	28/15	$32.80^{+0.24}_{-0.21}$	$36.2^{+4.3}_{-3.3}$	…	…
MCG-06-08-024	7/0	…	<30.8	…	…

Note.
[a] Given as the total number of PNe/approximate number of PNe contributing to distance.

including enough galaxy luminosity such that, with the proper exposure time, at least 30 PNe will be detected in the top 1 mag of the luminosity function.

In addition, the PNLF technique can benefit from additional methodological improvements that we summarize in 7.

6.2. Contamination of the PNLF

In Paper I, we described several classes of objects that could be confused with PNe and the ways in which MUSE spectra can be used to reject them from our PN samples. The possible interlopers that were discussed included SNRs, H II regions, and background galaxies. Not mentioned in the discussion was another possible source of *overluminous PNe* that can cause confusion. As first noted by Jacoby et al. (1996), Wolf-Rayet (W-R) nebulae (Nazé et al. 2003) can possibly contaminate the PNLF in star-forming galaxies. Because some of these high-mass nebulae are excited by very luminous O-stars with temperatures of ∼100,000 K (similar to the central stars of PNe), their spectra can be indistinguishable from PNe (Chu 2016). Yet the [O III] luminosities of these PN mimics can be nearly 10 times brighter than M^*. Figures 1(b) and 4(b) of Esteban et al. (1994) show spectra of two W-R nebulae in M33. At large distances, these objects can appear pointlike and can contaminate the PNLF.

Fortunately, in many cases, this source of confusion should not be a problem. Specifically,

1. In classic E/S0 galaxies, Pop I objects such as W-R nebulae are unlikely to exist.
2. In star-forming galaxies closer than ∼20 Mpc, the continuum from the nebula's exciting O-star (M_V as luminous as −7) can be bright enough to detect (Nazé et al. 2003; Kehrig et al. 2011). Additionally, in good seeing, the nebulae will generally be large enough ($r > 20$ pc) to be spatially resolved.
3. In systems where W-R nebulae are relatively rare, the objects will likely either be much more luminous than the PNLF cutoff, and be identifiable as outliers, or fainter than M^* and have a negligible effect on the PNLF distance. It is only when W-R nebulae are marginally brighter than M^* in star-forming galaxies beyond Virgo and Fornax that they can influence the PNLF maximum-likelihood fit. In such galaxies, the line diagnostics of W-R nebulae will place them on the border between H II regions and PNe, and thus make them hard to distinguish from true PNe. Among the galaxies in this study, PN1 in NGC 5248 is a possible candidate for a W-R contaminant.

There may also be unusual emission-line sources, such as the ultraluminous X-ray source in Holmberg-II (Lehmann et al. 2005) and the black hole in the NGC 4472 globular cluster RZ 2109 (Zepf et al. 2008) that could be mistaken for PNe. At the distance of NGC 1385 ($d \sim 25$ Mpc), these objects, which are as bright or brighter than M^*, would have $m_{5007} \sim 24$–25. Fortunately, such objects are rare and can have spectral features that discriminate them from PN. Thus, they are unlikely to be a problem.

6.3. Shape of the PNLF

PNLF distances rely on fitting the apparent magnitude distribution of PNe within a galaxy to some assumed form for the distribution of absolute PN magnitudes. This paper uses the expression first proposed by Ciardullo et al. (1989) as a

Table 11
Combined PNLF

Galaxy	$M_{\rm lim}$	Total PNe	PN with $M < M_{\rm lim}$
NGC 628	−3.19	202	90
NGC 1052	−3.74	87	39
NGC 1326	−3.26	55	39
NGC 1351	−3.43	102	45
NGC 1380	−3.22	112	78
NGC 1385	−3.65	78	40
NGC 1399	−3.27	232	163
NGC 1404	−3.70	126	38
NGC 1433[a]	−3.25	258	95
NGC 1512	−3.16	210	144
NGC 4038/9	−3.40	228	152
NGC 4365	−3.71	64	30
NGC 4418	−3.86	47	24
NGC 4472	−3.91	81	39

Note.
[a] PNe from Pointings P2, P3, and P5 have been excluded, due to their poorly determined aperture corrections.

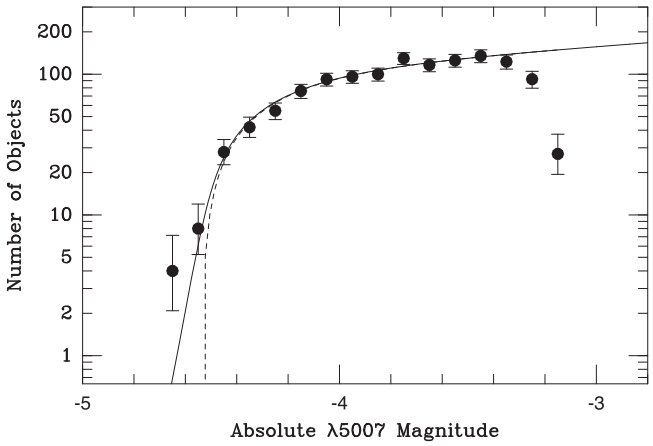

Figure 59. The combined PNLF from the 14 galaxies listed in Table 11. The PNe's absolute magnitudes have been computed using each system's most likely apparent distance modulus. The dashed line shows our assumed empirical PNLF (Equation (2)); the solid curve gives the expected PNLF when accounting for the formal errors of each galaxy's distance determination. (The effect of field-to-field aperture correction errors for those galaxies observed with multiple MUSE pointings is not included in the analysis.)

template, but other forms of the function are possible (e.g., Longobardi et al. 2013; Valenzuela et al. 2019). The better we can define the true shape of the PNLF, the better the results of the fit.

To that end, it is instructive to sum the absolute [O III] magnitudes of all the galaxies in this survey to produce a single *grand* PNLF. In theory, such an analysis could lead to an improved expression for the shape of the PNLF cutoff: by reducing the errors introduced by counting statistics, subtle deviations from Equation (2) could become apparent. On the other hand, any error associated with the conversion of apparent to absolute magnitude will propagate into the summed PNLF; such errors include the formal uncertainties of the galaxy distance determinations, the field-to-field zero-point errors for systems with more than one MUSE data cube, and any population-dependent change in the PNLF's shape. These errors will all work to soften the abruptness of the function's bright-end cutoff, (slightly) flatten the PNLF's power-law slope, and smooth over possible high-frequency features in the distribution.

Table 11 lists the galaxies analyzed in this paper that have well-defined PNLFs. Also listed in the table are NGC 628 (Paper I) and NGC 1380 (Paper I and Chase et al. 2023), both of which also have high-quality DELF measurements. Included in the table are our estimates for the galaxies' absolute λ5007 magnitudes for 90% completeness (assuming their most likely PNLF distances), the total number of PNe detected, and the number of PNe above the completeness limit. These data are coadded into the single PNLF shown in Figure 59.

Before discussing the luminosity function, it is imperative to be aware of the nuances involved in performing this coaddition. The solid curve attempts to model the effect of distance uncertainties in the data set by smoothing our adopted PNLF (Equation 2) by kernels derived from the galaxies' likelihood contours. While the resultant model is a better fit to the coadded PNLF, there is still a slight overdensity of objects brighter than M^*, and there are a number of other factors that are not included in the analysis. For example, zero-point errors caused by uncertain MUSE flux calibrations, aperture corrections, foreground dust, and possible metallicity dependencies will not affect the coaddition for galaxies observed in a single MUSE pointing. However, these zero-point issues will distort the PNLF's shape in systems observed via a mosaic of MUSE frames (see Section 5.10). The propagation of that error into the summed PNLF is not being modeled.

Similarly, a simple coaddition does not account for the presence of PN superpositions, i.e., two (or more) pointlike [O III] sources projected onto the same resolution element of the detector. When blends are present, they can distort the shape of the PNLF and produce a distance solution that is bimodal; the likelihood contours shown in Figure 36 provide one such example.

In this study, we have minimized the effect of blends by excluding PNe within a few arcsecs of the parent galaxy's nucleus. As a result, even when possible super-M^* objects were detected, the likelihood that they were caused by blends was relatively low (see Figures 10, 36, and 48). However, while the probability of such an occurrence in any one galaxy may be small, the likelihood of a superposition being present somewhere in the data set is significant. The curve shown in Figure 59 does not account for this possibility.

Another effect not modeled is the effect of dust within the target galaxies. Internal reddening in late-type galaxies may distort the shape of PNLF by effectively subdividing the PN population into multiple components: some extincted and some not. Models suggest that the effect of this bifurcation (or trifurcation) on the PNLF distances is minor (e.g., Feldmeier et al. 1997; González-Santamaría et al. 2021; Guo et al. 2021), but in highly inclined or interacting systems, it may have an effect.

Finally, it is important to note that our coaddition is only sensitive to changes in the PNLF's shape among different galaxy populations. Any process that shifts the location of the PNLF cutoff, but not the function's shape, will not be detected by the analysis. In other words, Figure 59 only shows that the shape of the bright end of the PNLF depends very little on the type of galaxy being observed; it does not provide any information about whether, for example, the PNLF of spiral galaxies are systematically brighter than those of early-type systems.

The PNLF of Figure 59 consists of 1016 objects brighter than their galaxies' completeness limits. Overall the data follow the prediction based on Equation (2) curve extremely well. The two noticeable deviations are a possible slight overestimate of the number of PNe with $M_{5007} = -3.85$ and a clear underestimate of objects with magnitudes brighter than M^*.

The latter feature is critical for fitting the PNLF, but the significance of the feature is difficult to determine. As pointed out above, the curve showing the expected PNLF does not include a number of effects such as PN superpositions and zero-point differences in a mosaic of MUSE pointings. These issues could easily produce the high-luminosity tail seen in Figure 59.

Another possible cause of the PNLF's high-luminosity tail is contamination by non-PNe. Line diagnostics are very efficient at eliminating objects such as H II regions and SNe remnants from the PN sample. Still, some interlopers may slip through, including nebulae produced by W-R stars (see Section 6.2). A careful investigation of the super-M^* objects shown in Figure 59 is beyond the scope of this paper but clearly needs to be done.

Of course, the high-luminosity tail of Figure 59 may be real. Davis et al. (2018) showed that the true [O III] luminosities of PNe in M31's bulge extend well beyond M^*. They argue that the observed bright-end cutoff of the PNLF is a product of the dust produced during the AGB phase: the more massive the core, the more massive and dusty the envelope, and the greater the circumnebular extinction. This hypothesis is consistent with the results of Ciardullo & Jacoby (1999), who found a steep correlation between the core mass of a PN and its self-extinction. If this is true, then the viewing angle may affect the observed brightness of a distant PN; for instance, a favorable orientation (e.g., along a PN's polar axis) may result in less attenuation and a brighter apparent magnitude. Consequently, an extremely luminous PN, when viewed at just the right angle, may be recorded as overluminous. In this cartoon model, the bright-end tail seen in Figure 59 is intrinsic to the PNLF itself, and Equation (2) must be modified to include the existence of these objects.

6.4. *Measuring* H_0 *with PNe*

The PNLF method has been improved significantly with VLT/MUSE and the DELF techniques. With a sufficient sample of well-observed and well-selected galaxies, the method can help deliver a measurement of H_0, either directly via distances to galaxies in the relatively unperturbed Hubble flow, or by calibrating SN Ia luminosities in the spirit of the Cepheid and TRGB approaches.

The zero-point of the PNLF distance scale, though, cannot be tied to stars in the Milky Way. Thus, their distances are not completely independent of the results of other methods (e.g., Cepheids, eclipsing binaries). However, the PNLF works in all types of large galaxies, from the latest Pop I systems to the reddest elliptical galaxies, and the technique can reach systems outside the Local Supercluster that are ill-suited for Cepheid, TRGB, and/or SN Ia studies. Moreover, the requisite data can be acquired quickly and efficiently from the ground, without the need for expensive space-based observations. Thus, a PNLF measure of H_0 can offer a unique perspective on the robustness of other results.

A PNLF program to measure H_0 would have to target galaxies that:

1. are relatively isolated, in order to minimize the effect of peculiar motions on the estimation of the Hubble flow. The larger the galaxy group, the larger the number of PNLF distances that would be needed to obtain a true measure of the system's Hubble velocity and distance.
2. have distances exceeding ∼30 Mpc to reduce the effects of flows within the local volume of space.
3. have absolute V-band magnitudes of $M_V \lesssim -19.5$ (i.e., V absolute luminosities of at least $\sim 5 \times 10^9 L_\odot$). Any PNLF study must survey at least this amount of light to ensure that the top ∼1 mag of the PNLF is sufficiently populated to deliver a precision measure of the PNLF cutoff. In practice, a target galaxy must be brighter than this, since (a) observations from a limited-field instrument such as MUSE will likely not cover the entire galaxy, and (b) PNe projected in the highest surface brightness regions of the system will be difficult to detect.
4. have moderately bright point sources in the field to enable a precise measurement of the photometric aperture correction. Foreground Milky Way stars are ideal, but for systems beyond ∼30 Mpc, bright globular clusters will suffice.

In addition, although the PNLF can be applied to galaxies of all Hubble types, the early-type systems are most easily analyzed, as their PN samples will not be severely contaminated by interlopers such as H II, SNRs, and W-R nebulae. Uncertainties associated with internal extinction would also not be an issue.

With those caveats in mind, of the 23 galaxies analyzed in this paper and Paper I, only six are potentially useful for an H_0 study, and only two have distances greater than 30 Mpc: NGC 6958, which is poorly measured by the present observations, and NGC 4418. At face value, the H_0 values found from these two objects are 69.2 ± 11.0 and 75.0 ± 9.6 km s^{-1}, respectively; their weighted average is 74.2 ± 7.2 km s^{-1} Mpc^{-1}. Note that because the quoted errors are dominated by the uncertain (∼10%) contribution of peculiar motions to the galaxies' recessional velocities, the error on H_0 can be reduced to <4% with a larger sample (∼25) of galaxies.

It should be stressed that most of the galaxies mentioned in this paper were not observed in a manner optimal for distance scale studies. NGC 4418 happened to have a bright foreground star present in its MUSE data cube, but most of the systems discussed in this paper do not. It is also possible that some of the galaxies were observed during nights of uneven transparency. And most notably, the effect of metallicity shifts on the PNLF has not been considered. For H_0 studies, we expect this last effect to be negligible: although the PNLF cutoff is known to fade slightly in populations with sub-LMC metal abundances (e.g., Ciardullo & Jacoby 1992; Dopita et al. 1992; Schönberner et al. 2010), such systems are not generally the target of a PNLF investigation. As pointed out above, the PNLF cutoff is not well defined in systems fainter than $M_V \sim -19.5$. According to the mass–metallicity relation for local galaxies (e.g., Tremonti et al. 2004), this basically ensures that any system measured well enough to be useful for a study of the Hubble constant will be in the regime where metallicity effects are minimal.

The fact that our H_0 result is very similar to current best estimates in the Hubble tension literature is encouraging, but likely fortuitous. Clearly, in order to advance the use of the PNLF for distance scale studies, we need a larger sample of

galaxies that meet the criteria listed above, and this means new targeted observations are necessary.

7. Summary

We selected a heterogeneous sample of 20 galaxies from the VLT/MUSE archive to study the utility and accuracy of the PNLF as a tool for determining extragalactic distances. By combining the spectrophotometric capabilities of MUSE with the photometric procedures of Paper I and the fitting algorithms of Chase et al. (2023), we were able to test our ability to obtain precision distances to galaxies spanning a wide range of morphologies and star formation rates. For star-forming systems, MUSE measurements of the PNLF are quite effective unless the star formation is extreme. Although the comparison samples are small, the results for early-type galaxies are similarly encouraging, as PNLF measurements are as consistent with other well-accepted methods (4%–8%) as those methods are with each other.

Of our 20 galaxies:

1. 16 yielded fair-to-excellent PNLFs from which we were able to derive galactic distances with quantifiable uncertainties.
2. Three did not contain enough PNe for a sufficient sampling of the PNLF. For these systems, we could only derive upper limits to their distances.
3. One is highly affected by internal extinction. For this object, we could only derive an upper limit to the distance.

In nearly all the disappointing cases, the quality of the results was limited by inadequate sample sizes, due to poor seeing or short exposure times. In summary, we derived well-constrained distances for 10 galaxies, useful distances for six galaxies, upper limits to three galaxies, and a likely overestimated distance due to internal dust for one galaxy.

In creating our galactic PNLFs, we examined the spectrum of each pointlike [O III] source and used the procedures described in Paper I to remove H II regions, SNRs, and background Lyα emitting galaxies from the PN sample. This approach worked quite well, and greatly reduced the systematic errors that could arise from the inclusion of non-PN contaminants.

Our investigation also examined the effect of possible PN superpositions on our galactic distances (Chase et al. 2023). In theory, the blending of two bright PNe into a single emission-line source can lead to PNLF solutions that underestimate the true distance to a galaxy and produce a systematic bias in the technique's distance scale. In practice, because our present study already excluded each galaxy's highest surface brightness regions from the analysis, the effect of superpositions on the current data set was minor: in all cases the most likely distance modulus was unaffected, and in only one case was the PDF distorted enough to produce a bimodal solution. However, since the likelihood of a PN superposition goes as the square of the distance, it will be important to include this effect in future PNLF studies.

Two of the galaxies analyzed in this study have distances large enough to reduce their expected peculiar motions to less than 10% of their Hubble flow velocity. For these objects, we calculated a Hubble constant independent of the SN Ia calibration. Our results are encouraging, and with 25–30 more galaxies, the PNLF could provide an additional way to examine the current tension in the Hubble constant. Perhaps even more importantly, the PNLF allows a rare opportunity to cross check other distance techniques (e.g., Cepheids, TRGB, SBF) that are used to calibrate SN Ia, enabling another path for measuring H_0 through the PNLF.

Consequently, we look forward to future observations that are structured specifically for PNLF distance measurements that extend into the Hubble flow. Those observations will require:

1. reasonably bright aperture correction reference stars in the MUSE field of view,
2. good-to-excellent image quality (i.e., $<0\farcs75$), and
3. exposure times and field coverage sufficient to identify $\sim$50 PNe in the top $\sim$1 mag of the PNLF. Effectively, this means sampling $M_V \lesssim -19.5$ of galaxy light.

There is progress to be made on the shape of the PNLF as well. The MUSE observational data are so good that we need to devise a more applicable reference PNLF than the one defined 35 yr ago from PN photometry of M31's bulge. After shifting all usable PNLFs to a common distance and stacking them, we see that this higher fidelity combined PNLF fails to match the old reference PNLF in critical ways. In particular, the distribution presents some evidence that the phenomenon of overluminous PNe may be real. Most objects previously classified as overluminous have either been dismissed as PN contaminants or identified as the likely product of poor photometry. However, the easiest (but not the only) way to explain the behavior of the bright end of the coadded PNLF is to modify the shape of the luminosity function's bright-end tail.

In a future era of Extremely Large Telescopes with MUSE-like IFSs, the PNLF's distance range, which is now limited by photon collection rates, will increase by a factor of 2 or 3. The accuracy of the PNLF technique will then become limited by a different set of systematic errors (e.g., photometric zero-point, the near-field calibrations of the luminosity function, and the population dependence of the PNLF cutoff). At that point, though, cosmic velocity errors will be proportionally smaller so that fewer galaxies will need to be observed to achieve a given precision.

Acknowledgments

We thank You-Hua Chu for helpful discussions concerning the spectra of W-R nebulae. This work was supported by the NSF through grant AST2206090. Based on data obtained from the ESO Science Archive Facility with DOIs https://doi.org/10.18727/archive/41 and https://doi.org/10.18727/archive/42. This work has made use of the SIMBAD database, operated at CDS, Strasbourg, France, and of NED, which is operated by the Jet Propulsion Laboratory, California Institute of Technology, under contract with the National Aeronautics and Space Administration. The Institute for Gravitation and the Cosmos is supported by the Eberly College of Science and the Office of the Senior Vice President for Research at the Pennsylvania State University.

Appendix A
Notes on NGC 1385

A.1. The Issue

Distances derived using the PNLF method have generally been highly consistent across authors, reflecting only the stated

errors in the measurements. Thus, the discrepancy between the distance to NGC 1385 derived in this paper and that found by Scheuermann et al. (2022) is very unusual and warrants exploration. We first consider whether NGC 1385's properties are consistent with membership in the Eridanus cluster 20–25 Mpc away. We then look in detail at the PN photometric results to uncover any clues.

A.2. Cluster Member Distances and Kinematics in Eridanus

The plausibility of NGC 1385's distance determined in this work, compared to the much lower Tully–Fisher values from the literature, and the distance derived by Scheuermann et al. (2022), can be assessed through its probable membership in the Eridanus cluster. Table 12 compares the two PNLF distances to SBF measurements of Eridanus cluster members. Our distance of 25.0 Mpc is consistent with cluster membership, and the galaxy's radial velocity of 1499 km s^{-1} is close to the mean of the cluster (see Figure 5 of Willmer et al. 1989). Based on these data, the Scheuermann et al. (2022) distance, which is less than half our value, would seem implausible.

A.3. Detection and Photometry of PN Candidates in NGC 1385

A composite of the [O III] images for the five MUSE pointings, labeled P1–P5, is shown in Figure 60. Our detections are indicated with blue markers, and the PNe are numbered individually for each pointing, starting with PN1. Point sources that were rejected as either H II regions or SNRs are marked with red circles without labels. PNe from the sample of Scheuermann et al. (2022) are plotted in magenta and their SNRs are shown in orange. For the following detailed comparison, it is useful to remember that our brightest PN has an [O III] magnitude of $m_{5007} = 27.55$.

Pointing P1. Our work yielded 24 pointlike [O III] sources with spectra consistent with that of a PN; these sources have a brightness range between $27.55 \leqslant m_{5007} \leqslant 29.54$ mag. In contrast, Scheuermann et al. (2022) find only three objects in the field that they classify as PNe; their [O III] magnitudes are $m_{5007} = 26.52$, 26.65, and 27.25. The three identifications are detailed below.

PN6. Our analysis suggests that the data reduction processes used by the ESO Archive are slightly different from those employed by Scheuermann et al. (2022), and this results in a small astrometric offset between the two data sets. Thus, we strongly suspect that the object that Scheuermann et al. (2022) refer to PN6 as an unlabeled source in Figure 60, which has a red marker within the magenta marker (arrow). This places the Scheuermann et al. (2022) source 0.″80 east and 0.″93 north of our position. We classify the object as an unresolved, high-excitation H II region, as its [S II] line ratio diagnostic is at the low-density limit.

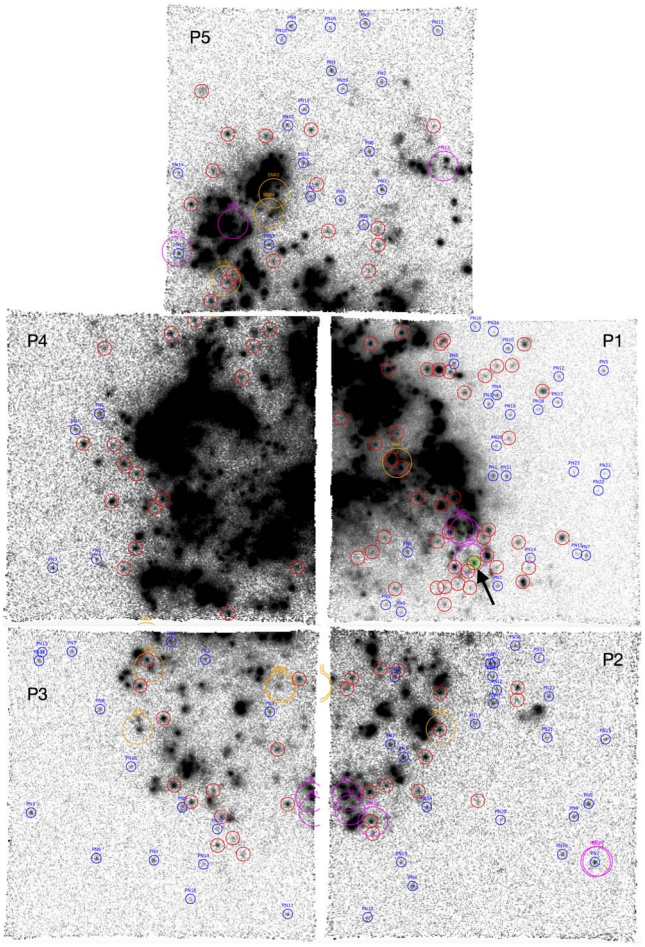

Figure 60. Composite [O III] on-band map of NGC 1385 with pointings P1–P5 identified. Our PN candidates are circled in blue and labeled; red circles without labels are objects classified as H II regions or SNRs. PNe and SNRs identified by Scheuermann et al. (2022) are shown in magenta and orange, respectively.

PN7. The object is located in a giant H II complex, and we classify its spectrum as that of an H II region.

PN11. Like PN7, the object is located in a giant H II complex, and based on its spectrum, we classified it as an H II region.

In summary, we classify none of Scheuermann et al. (2022) objects as PNe. Conversely, none of our 24 DELF-detected PNe are reported by Scheuermann et al. (2022).

Table 12
Distances of Eridanus Cluster Galaxies

Galaxy	Type	v_{rad} (km s^{-1})	Distance (Mpc)	Method
NGC 1385	SBc	1499	25.0	PNLF (this work)
NGC 1385	SBc	1499	9.8	PNLF (Scheuermann et al. 2022)
NGC 1297	SAB(s)0	1386	28.6	*I*-band SBF (Tonry et al. 2001)
NGC 1332	S0	1619	22.9	*I*-band SBF (Tonry et al. 2001)
NGC 1395	E2	1717	24.1	*I*-band SBF (Tonry et al. 2001)
NGC 1407	E0	1779	25.1	F814W SBF (Cantiello et al. 2005)
NGC 1426	E4	1443	24.1	*I*-band SBF (Tonry et al. 2001)
NGC 1439	E1	1667	26.7	*I*-band SBF (Tonry et al. 2001)

Pointing P2. We find 23 [O III] sources with spatial and spectral properties consistent with those of PNe. The brightnesses of these objects range between $27.58 \leqslant m_{5007} \leqslant 29.14$. In contrast, Scheuermann et al. (2022) report five PNe with magnitudes of $m_{5007} = 25.72$, 26.47, 27.63, 27.90, and 27.97 mag. These Scheuermann et al. (2022) identifications are as follows.

PN1. This object, which is located within a giant H II complex, is extremely bright in [O III], but its [S II] lines indicate a low-density nebula. If the object were a PN, it would be 1.83 mag (5.4 times) brighter than our next brightest planetary. Moreover, if the galaxy were at the distance of the Eridanus cluster, the luminosity of the PN would imply a central star luminosity of $\log L/L_{\odot} = 4.48$, which is well above any reasonable post-AGB evolutionary track. We conclude that this object cannot be a PN.

PN5. This source, which is projected on a complex background, is brighter in Hα than it is in [O III] and thus violates the Herrmann et al. (2008) criterion for [O III]-bright PNe. As indicated by the [S II] doublet, the object does have a high nebular density. Nevertheless, it is not classified as a PN.

PN16. The [S II] lines of this source are half the strength of Hα. It is an SNR.

PN17/PN19. The coordinates of these two sources are almost identical. As we find no evidence for a superposition of two point sources, neither in terms of separation in wavelength nor in terms of an elongated image, we conclude that it is a single object. We agree with Scheuermann et al. (2022) that it is a PN (our PN2).

Pointing P3. We find 16 PN candidates in the brightness range between $27.76 \leqslant m_{5007} \leqslant 29.19$. Scheuermann et al. (2022) report no detections in this field.

Pointing P4. We find four PN candidates in the brightness range between $27.44 \leqslant m_{5007} \leqslant 28.32$ mag. Scheuermann et al. (2022) report no detections in this field.

Pointing P5. We find 19 PN candidates in the brightness range between $27.56 \leqslant m_{5007} \leqslant 29.09$. Scheuermann et al. (2022) find three PNe candidates with brightnesses of $m_{5007} = 27.07$, 27.37, and 27.97. Specifically, the Scheuermann et al. (2022) identifications are as follows:

PN10. The spectrum of this object clearly supports its classification as an H II region.

PN13. Like PN10, the spectrum of this object is consistent with that of an H II region.

PN18. We agree that this object is a PN. However, our photometry yields a magnitude that is ∼1 mag fainter than that quoted by Scheuermann et al. (2022), i.e., $m_{5007} = 28.84 \pm 0.28$.

A.4. Summary

The brightest PNe in a galaxy are the most important objects for deriving a PNLF distance. After a careful review of the brightest PNe reported by Scheuermann et al. (2022), we find that our photometry and spectroscopy do not support those objects' classifications as PNe. Consequently, we are unable to reproduce the short (9.8 Mpc) distance to the galaxy.

Appendix B
Notes on Aperture Correction Uncertainties

Uncertainties associated with the detector calibration, atmospheric extinction, flux calibration, dust attenuation, population metallicity, and photon statistics all affect the precision of a PNLF measurement. However, one of the most important terms in the error budget of a PNLF distance determination is the observation's aperture correction. The MUSE IFS is capable of delivering a photometric precision of 0.04 mag (see Section 3 and Figure 6 of Paper 1). However, to reach this level of accuracy, it is imperative that a bright point source—typically a foreground star—be present within the MUSE science field of view. Without such a star, the relative magnitudes produced by small-aperture photometry cannot be scaled to the objects' true brightness, at least to the precision necessary for competitive extragalactic distance determinations.

This field star prerequisite is rarely met when data are taken for another purpose. Consequently, aperture corrections performed on archival MUSE data cubes must often be based on faint, pointlike sources whose true nature is unclear. This limits the precision of the measurements. If the objects are truly pointlike, the shot noise associated with the photometry will be non-negligible (though, in principle, the noise can be reduced by the square root of the number of PSF standards). However, if the faint pointlike sources are actually marginally resolved—for instance, if they are actually globular clusters associated with a nearby target galaxy—then the aperture corrections for the point-source PNe will be overestimated. This issue can be particularly vexing in early-type galaxies, where the system's globular clusters may be the best (or only) pointlike sources in the field. Moreover, it is possible that different stellar populations with different colors can introduce wavelength-dependent effects into the aperture corrections, as speculated in Paper 1. Finally, a spatially variable background of unresolved stars in the environment of faint pointlike sources can potentially introduce a systematic error that is also wavelength dependent. Thus, without the presence of a bright point source in the field, a truly useful error estimate is difficult to obtain.

In order to illustrate the issue, we consider two Fornax cluster elliptical galaxies observed with MUSE using similar exposure times under similar seeing conditions. One, NGC 1404 has a bright point source projected in the field (2MASS J03385017-3535311, $G = 16.2$ mag). The other, NGC 1351 has none. Thus, their aperture corrections have very different degrees of reliability, and the overall precision of their derived distances is quite different.

The top panel of Figure 61 shows continuum images of NGC 1404 and 1351 formed from the coaddition of the 40 MUSE data cube layers between 4968 and 5018 Å. These are the layers used to determine the cube's aperture correction, as the region is close enough in wavelength to the redshifted [O III] line so that the wavelength dependence of seeing can be ignored. By coadding 40 layers, we increase the S/N over that for the [O III] λ5007 line alone.

The encircled objects in the figure are the pointlike sources chosen to define the field's PSF. Table 13 lists these sources, along with their equatorial coordinates and our derived quantities for the objects' FWHM, total flux, and inferred aperture correction. The latter three values were derived by fitting a Gaussian to the objects' radial profiles via the Levenberg–Marquardt least-squares algorithm.

To estimate the robustness of these values, we repeated the FWHM measurements all along the MUSE spectra, thereby obtaining the FWHM of the stars versus wavelength. The middle panels of Figure 61 show the results of these fits, while the bottom panel displays the residuals from a best-fit second-

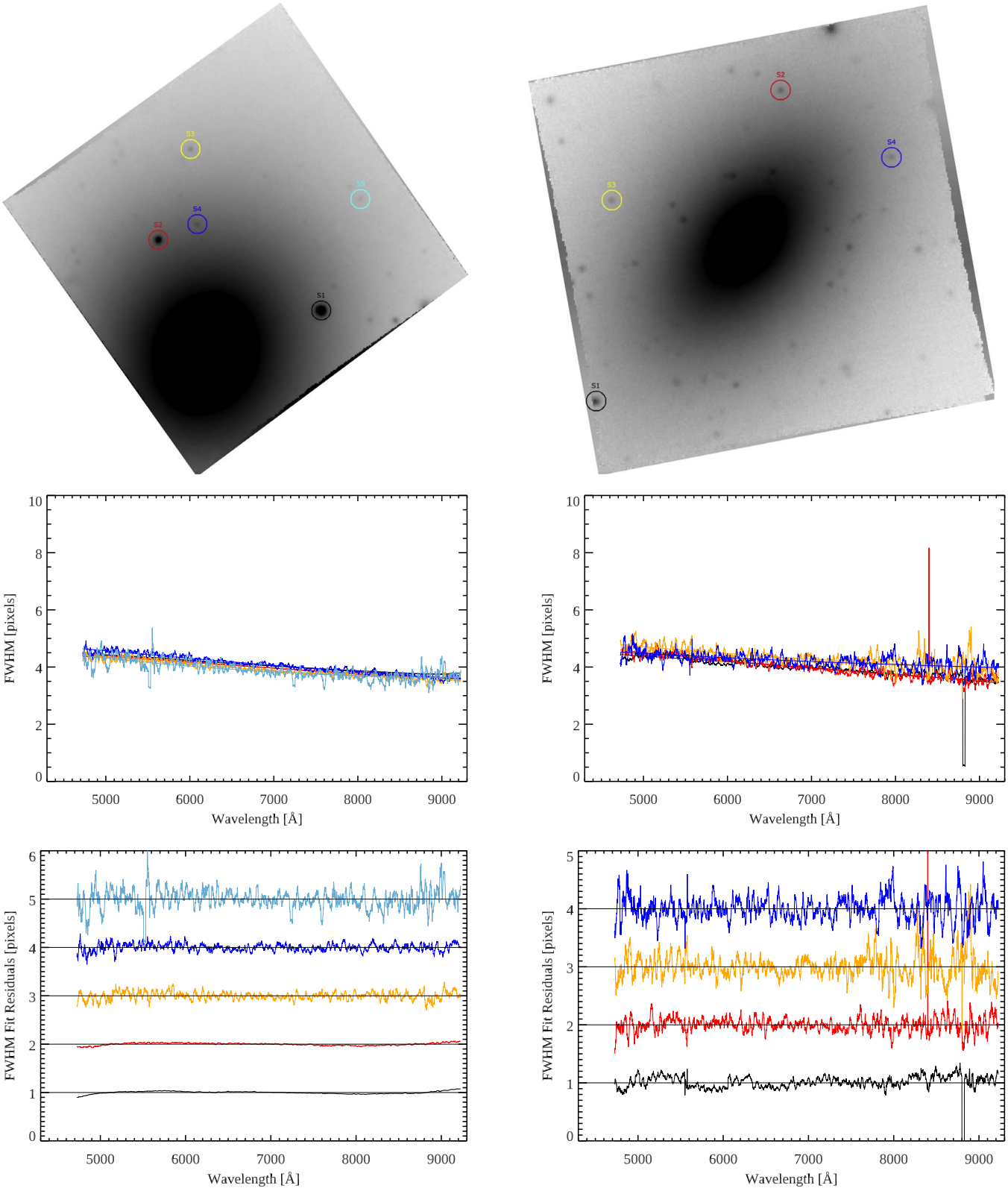

Figure 61. The top panels show the continuum images for the nuclear fields of NGC 1404 (left) and NGC 1351 (right). The PSF stars are identified with colored markers. The middle panels show the wavelength dependence of the stars' PSFs' by plotting their best-fit FWHMs. The data are fit with a second-degree polynomial. The lower panels show the residuals from this fit, with the brightest star on the bottom and the faintest on the top. Each curve is offset by 1.0 from the previous curve for clarity. The colors correspond to those shown in the images. Note the large residuals associated with the fainter stars.

order polynomial. The different colors correspond to those used to identify the stars in the top panel.

As can clearly be seen from residuals in the bottom panel, stars S1 and S2 in NGC 1404, are bright enough to deliver well-behaved FWHM values that are fitted well by the polynomials. Their FWHM values are almost identical and vary slowly with wavelength, as expected from theory (Kamann et al. 2013). Of course, as the stellar flux decreases,

Table 13
PSF Stars

NGC 1404 PSF Stars					
Star	R.A. (2000)	Decl. (2000)	FWHM (pixels)	Total Flux[a]	Apcor Δmag
S1 (blk)	3:38:50.16	−35:35:30.4	4.41	3011413	0.154
S2 (red)	3:38:52.66	−35:35:17.2	4.41	650172	0.168
S3 (yel)	3:38:52.16	−35:35:00.3	4.10	38331	0.159
S4 (blu)	3:38:52.06	−35:35:14.3	4.60	4762	0.306
S5 (cya)	3:38:49.55	−35:35:09.6	4.32	1672	0.005
NGC 1351 PSF Stars					
Star	R.A. (2000)	Decl. (2000)	FWHM (pixels)	Total Flux[a]	Apcor Δmag
S1 (blk)	3:30:36.46	−34:51:39.5	4.39	68552	0.100
S2 (red)	3:30:34.54	−34:50:50.9	4.31	26782	0.217
S3 (yel)	3:30:36.30	−34:51:08.3	4.72	18659	0.273
S4 (blu)	3:30:33.38	−34:51:01.2	4.50	12373	0.181

Note.
[a] Units of 10^{-20} erg cm^{-2} s^{-1}, bandpass [4968, 5018 Å].

the fits for the fainter stars become less and less reliable. In NGC 1351, all the PSF objects are faint, and their PSF fits are much noisier.

The brightest star, S1, happens to be located at the edge of the field. This does not dramatically affect the Gaussian fit, but becomes important for measuring an aperture correction, as will be shown below.

Figures 62 and 63 plot the radial profiles of the PSF stars in units of flux. Each dot represents the flux of a given pixel in the continuum image shown in Figure 61. The radius from the stellar centroid is given in units of MUSE spaxels and must be multiplied by 0.2 to convert to arcseconds. The Gaussian and Moffat fits to the data are also shown.

The bright star S1 in NGC 1404 is located at the edge of the field. Nevertheless, its profile is extremely well defined. It is even possible to recognize the advantage of a Moffat fit over a simple Gaussian, specifically in the core and in the wings of the PSF. Star S2 in NGC 1404 is also well behaved, but for the fainter stars, the scatter becomes visibly larger, and the background becomes the dominant source of error. Notably, this background scatter is not all photon noise: it also arises from the spatial variation of the galaxy light underlying the star. The strongest gradients are generally found in elliptical galaxies, but they can also be important in the spiral arms of later-type systems where crowding of partially resolved clusters, luminous supergiant stars, etc. presents a surface brightness distribution that is anything but smooth. The effect is quite visible for the PSF stars in NGC 1351 in Figure 63. Our software to compute the Gaussian/Moffat fits and create the radial plots involves a correction for background surface brightness distributions that are variable on long scales. We fit a third-order, two-dimensional, polynomial to the input image, where the star and a sufficient margin around it are masked out. The background model is then subtracted such that the resulting intensity around the star is essentially a flat zero. This procedure works well, even across the steep gradients of elliptical galaxies. However, it becomes limited when the PSF star is relatively faint in comparison to a crowded, partially resolved, stellar background.

To obtain our aperture corrections, we first inspected the PSF fit for each star and discarded any result that was obviously an outlier. Following Paper I, we then measured the stars' curves of growth using the `APER` program in `DAOPHOT` (Stetson 1987). Figure 64 shows (top to bottom) the resultant aperture corrections for the stars of NGC 1404. The panels plot, from top to bottom, apertures with radii of 3, 4, 5 (and where applicable, also 6) pixels as a function of wavelength. Unsurprisingly, the curves for S1 (black) and S2 (red) are quite similar and well behaved. Moreover, although the curves for S3 are much noisier, a polynomial fit is still in good agreement with the curves for the brighter stars. Conversely, the curves for S4 deviate strongly from expectations, and the ones for S5 are completely useless. If we ignore the latter two stars, we can formally derive the observation's mean correction for a 4 pixel aperture to be 0.160 ± 0.007 mag

In contrast, an assessment of aperture correction for NGC 1351 is much more difficult. As Figure 65 reveals, the curves all deviate significantly one from another, and there is

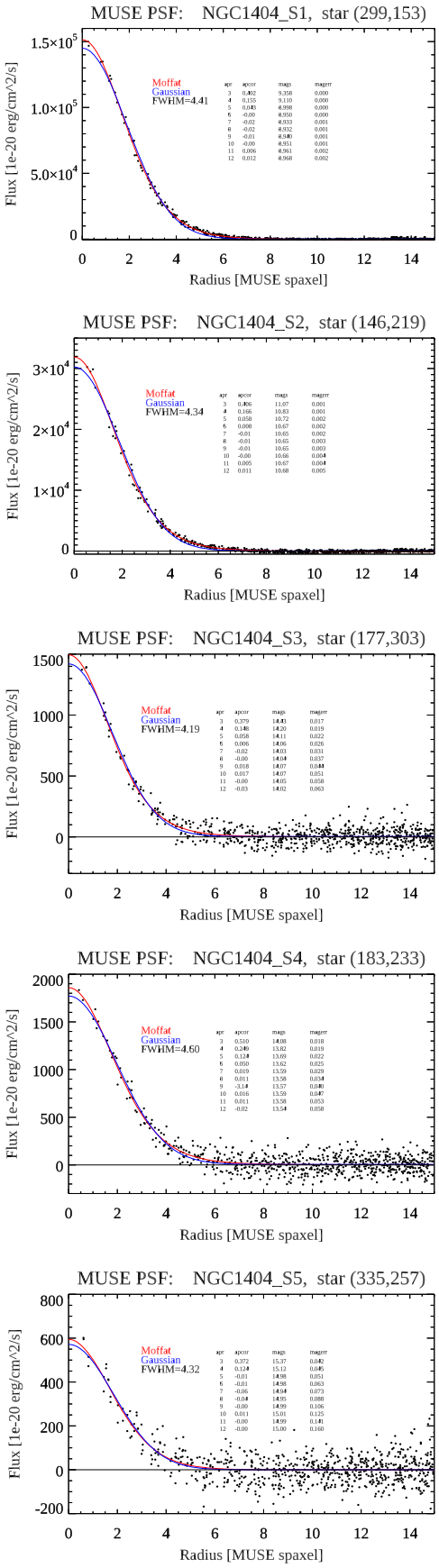

Figure 62. NGC 1404 PSF star radial plots, obtained from the image shown in Figure 61.

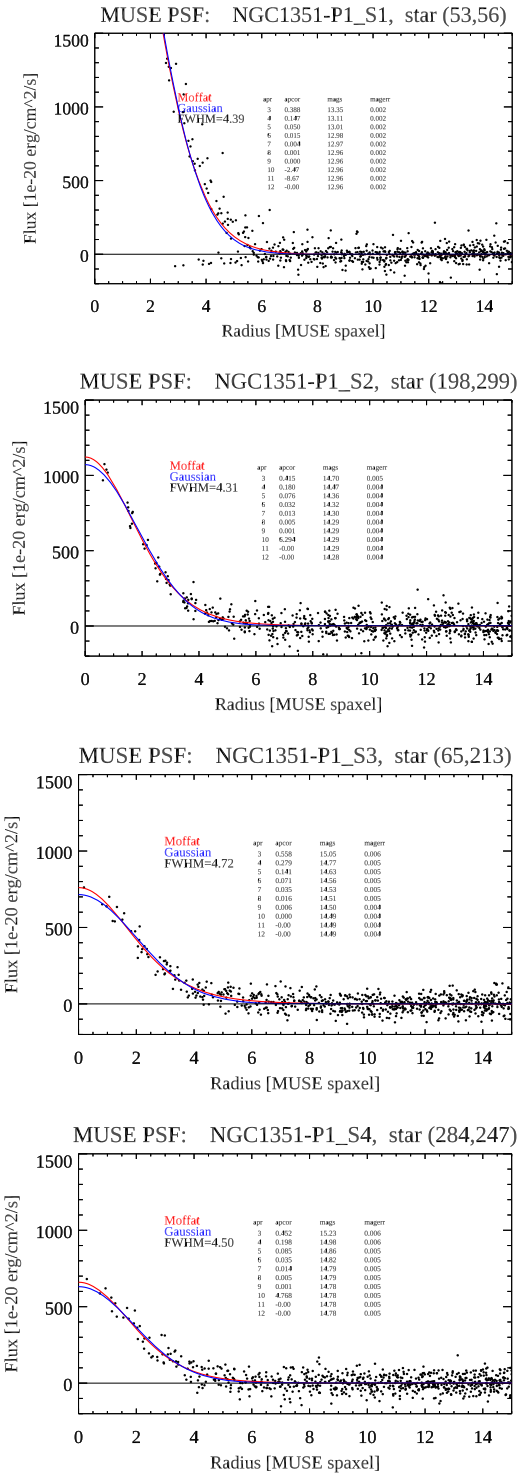

Figure 63. NGC 1351 PSF star radial plots, obtained from the image shown in Figure 61.

an apparent trend of the higher aperture corrections being associated with the fainter stars. In a case like this, it is tempting to adopt the data from the brightest star (S1) as the best estimate, but the star's proximity to the edge of the field complicates the situation. Deriving a reliable correction and statistical error for this galaxy is therefore challenging, and the best we can do is adopt an error value of between 0.1 and

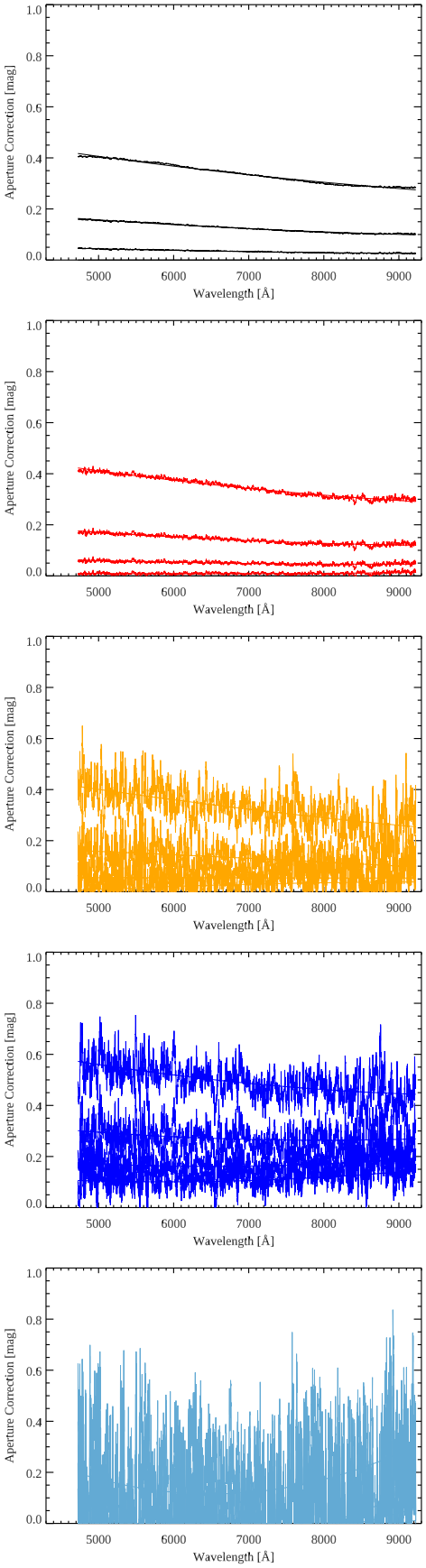

Figure 64. NGC 1404 PSF star aperture corrections as a function of wavelength, obtained from the image shown in Figure 61. PSF stars S1–S5 are shown from top to bottom.

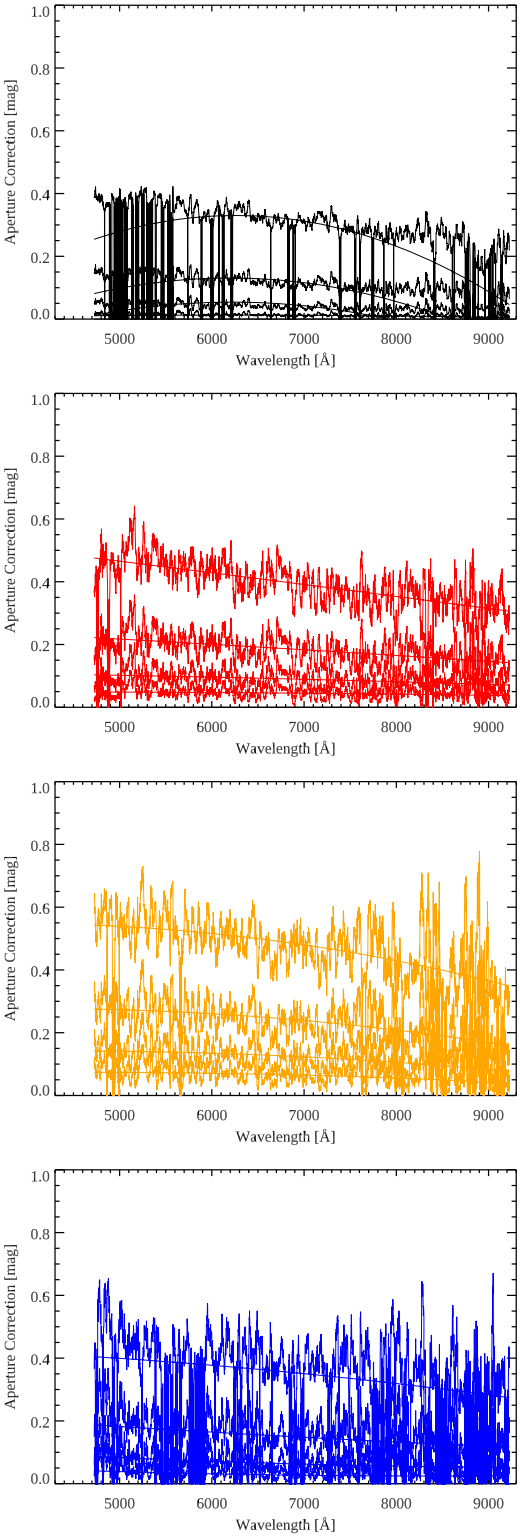

Figure 65. NGC 1351 PSF star aperture corrections as a function of wavelength, obtained from the image shown in Figure 61. PSF stars S1–S4 are shown from top to bottom.

0.2 mag. Clearly, a more sophisticated approach for measuring the PSF, and hence, the zero-point of the photometry, is required to make the best use of the archival data for NGC 1351. However, that is beyond the scope of the current work.

ORCID iDs

George H. Jacoby https://orcid.org/0000-0001-7970-0277
Robin Ciardullo https://orcid.org/0000-0002-1328-0211
Martin M. Roth https://orcid.org/0000-0003-2451-739X
Magda Arnaboldi https://orcid.org/0000-0001-7214-3009
Peter M. Weilbacher https://orcid.org/0000-0003-4766-902X

References

Aaronson, M. 1977, PhD thesis, Harvard Univ.
Anand, G. S., Tully, R. B., Rizzi, L., Riess, A. G., & Yuan, W. 2022, ApJ, 932, 15
Arnaboldi, M., Aguerri, J. A. L., Napolitano, N. R., et al. 2002, AJ, 123, 760
Arnaboldi, M., Freeman, K. C., Hui, X., Capaccioli, M., & Ford, H. 1994, Msngr, 76, 40
Arnett, W. D. 1982, ApJ, 254, 1
Bacon, R., Accardo, M., Adjali, L., et al. 2010, Proc. SPIE, 7735, 773508
Barmby, P., & Huchra, J. P. 2001, AJ, 122, 2458
Bhattacharya, S., Arnaboldi, M., Gerhard, O., et al. 2021, A&A, 647, A130
Binney, J. J., Davies, R. L., & Illingworth, G. D. 1990, ApJ, 361, 78
Blakeslee, J. P., Cantiello, M., Mei, S., et al. 2010, ApJ, 724, 657
Blakeslee, J. P., Jordán, A., Mei, S., et al. 2009, ApJ, 694, 556
Blakeslee, J. P., Lucey, J. R., Barris, B. J., Hudson, M. J., & Tonry, J. L. 2001, MNRAS, 327, 1004
Blom, C., Forbes, D. A., Foster, C., Romanowsky, A. J., & Brodie, J. P. 2014, MNRAS, 439, 2420
Bottinelli, L., Gouguenheim, L., Paturel, G., & de Vaucouleurs, G. 1984, A&AS, 56, 381
Bottinelli, L., Gouguenheim, L., Paturel, G., & Teerikorpi, P. 1986, A&A, 156, 157
Buta, R. 1986, ApJS, 61, 631
Buta, R., Alpert, A. J., Cobb, M. L., Crocker, D. A., & Purcell, G. B. 1998, AJ, 116, 1142
Buta, R., Ryder, S. D., Madsen, G. J., et al. 2001, AJ, 121, 225
Buta, R., & Williams, K. L. 1995, AJ, 109, 543
Buzzoni, A., Arnaboldi, M., & Corradi, R. L. M. 2006, MNRAS, 368, 877
Cantiello, M., Blakeslee, J. P., Raimondo, G., et al. 2005, ApJ, 634, 239
Caon, N., Capaccioli, M., & D'Onofrio, M. 1994, A&AS, 106, 199
Cardelli, J. A., Clayton, G. C., & Mathis, J. S. 1989, ApJ, 345, 245
Chase, O., Ciardullo, R., Roth, M. M., & Jacoby, G. H. 2023, ApJ, 950, 59
Chu, Y.-H. 2016, JPhCS, 728, 032007
Ciardullo, R. 2010, PASA, 27, 149
Ciardullo, R. 2012, Ap&SS, 341, 151
Ciardullo, R. 2013, in IAU Symp. 289, Advancing the Physics of Cosmic Distances, ed. R. de Grijs (Cambridge: Cambridge Univ. Press), 247
Ciardullo, R. 2022, FrASS, 9, 896326
Ciardullo, R., Feldmeier, J. J., Jacoby, G. H., et al. 2002, ApJ, 577, 31
Ciardullo, R., & Jacoby, G. H. 1992, ApJ, 388, 268
Ciardullo, R., & Jacoby, G. H. 1999, ApJ, 515, 191
Ciardullo, R., Jacoby, G. H., Ford, H. C., & Neill, J. D. 1989, ApJ, 339, 53
Ciardullo, R., Jacoby, G. H., & Harris, W. E. 1991, ApJ, 383, 487
Ciardullo, R., Jacoby, G. H., & Tonry, J. L. 1993, ApJ, 419, 479
Ciardullo, R., Sigurdsson, S., Feldmeier, J. J., & Jacoby, G. H. 2005, ApJ, 629, 499
Cohen, J. G. 1986, AJ, 92, 1039
Dalcanton, J. J., Williams, B. F., Seth, A. C., et al. 2009, ApJS, 183, 67
Dalle Ore, C., Faber, S. M., Jesus, J., Stoughton, R., & Burstein, D. 1991, ApJ, 366, 38
Danieli, S., van Dokkum, P., Abraham, R., et al. 2020, ApJL, 895, L4
Davis, B. D., Ciardullo, R., Jacoby, G. H., Feldmeier, J. J., & Indahl, B. L. 2018, ApJ, 863, 189
Davis, S., Pessi, P. J., Fraser, M., et al. 2021, ApJ, 909, 145
de Carvalho, R. R., Djorgovski, S., & da Costa, L. N. 1991, ApJS, 76, 1067
de Vaucouleurs, G., de Vaucouleurs, A., Corwin, H. G. J., et al. 1991, Third Reference Catalogue of Bright Galaxies (Berlin: Springer)
D'Onofrio, M., Zaggia, S. R., Longo, G., Caon, N., & Capaccioli, M. 1995, A&A, 296, 319
Dopita, M. A., Ho, I. T., Dressel, L. L., et al. 2015, ApJ, 801, 42
Dopita, M. A., Jacoby, G. H., & Vassiliadis, E. 1992, ApJ, 389, 27
Eddington, A. S. 1913, MNRAS, 73, 359
Ekholm, T., Lanoix, P., Teerikorpi, P., Fouqué, P., & Paturel, G. 2000, A&A, 355, 835
Emsellem, E., Schinnerer, E., Santoro, F., et al. 2022, A&A, 659, A191
Esteban, C., Vilchez, J. M., & Smith, L. J. 1994, AJ, 107, 1041
Faber, S. M., Wegner, G., Burstein, D., et al. 1989, ApJS, 69, 763
Fabricius, M. H., Saglia, R. P., Fisher, D. B., et al. 2012, ApJ, 754, 67
Feldmeier, J. J., Ciardullo, R., & Jacoby, G. H. 1997, ApJ, 479, 231
Fensch, J., van der Burg, R. F. J., Jeřábková, T., et al. 2019, A&A, 625, A77
Ferguson, H. C. 1989, AJ, 98, 367
Ferrarese, L., Mould, J. R., Kennicutt, R. C. J., et al. 2000, ApJ, 529, 745
Fiorentino, G., Musella, I., & Marconi, M. 2013, MNRAS, 434, 2866
Forbes, D. A., & Depoy, D. L. 1992, A&A, 259, 97
Foster, C., Pastorello, N., Roediger, J., et al. 2016, MNRAS, 457, 147
Franx, M., Illingworth, G., & Heckman, T. 1989, AJ, 98, 538
Freedman, W. L., Madore, B. F., Hatt, D., et al. 2019, ApJ, 882, 34
Gadotti, D. A., & de Souza, R. E. 2005, ApJ, 629, 797
Gadotti, D. A., Sánchez-Blázquez, P., Falcón-Barroso, J., et al. 2019, MNRAS, 482, 506
Gall, C., Stritzinger, M. D., Ashall, C., et al. 2018, A&A, 611, A58
Gehrels, N. 1986, ApJ, 303, 336
Gesicki, K., Zijlstra, A. A., & Miller Bertolami, M. M. 2018, NatAs, 2, 580
González-Santamaría, I., Manteiga, M., Manchado, A., et al. 2021, A&A, 656, A51
Graham, A. W., Colless, M. M., Busarello, G., Zaggia, S., & Longo, G. 1998, A&AS, 133, 325
Guo, H. L., Chen, B. Q., Yuan, H. B., et al. 2021, ApJ, 906, 47
Hartke, J., Arnaboldi, M., Gerhard, O., et al. 2020, A&A, 642, A46
Hartke, J., Arnaboldi, M., Longobardi, A., et al. 2017, A&A, 603, A104
Herrmann, K. A., Ciardullo, R., Feldmeier, J. J., & Vinciguerra, M. 2008, ApJ, 683, 630
Hoyt, T. J., Beaton, R. L., Freedman, W. L., et al. 2021, ApJ, 915, 34
Iodice, E., Capaccioli, M., Grado, A., et al. 2016, ApJ, 820, 42
Iodice, E., Sarzi, M., Bittner, A., et al. 2019, A&A, 627, A136
Jacoby, G. H., Ciardullo, R., & Ford, H. C. 1990, ApJ, 356, 332
Jacoby, G. H., Ciardullo, R., & Harris, W. E. 1996, ApJ, 462, 1
Jacoby, G. H., & De Marco, O. 2002, AJ, 123, 269
Jang, I. S., Hatt, D., Beaton, R. L., et al. 2018, ApJ, 852, 60
Jang, I. S., & Lee, M. G. 2015, ApJ, 807, 133
Jang, I. S., & Lee, M. G. 2017, ApJ, 836, 74
Jarrett, T. H., Chester, T., Cutri, R., Schneider, S. E., & Huchra, J. P. 2003, AJ, 125, 525
Jedrzejewski, R. I., Davies, R. L., & Illingworth, G. D. 1987, AJ, 94, 1508
Jensen, J. B., Tonry, J. L., Barris, B. J., et al. 2003, ApJ, 583, 712
Kamann, S., Wisotzki, L., & Roth, M. M. 2013, A&A, 549, A71
Kehrig, C., Oey, M. S., Crowther, P. A., et al. 2011, A&A, 526, A128
Khoperskov, S., Zinchenko, I., Avramov, B., et al. 2021, MNRAS, 500, 3870
Kreckel, K., Groves, B., Bigiel, F., et al. 2017, ApJ, 834, 174
Kudritzki, R. P., Méndez, R. H., Feldmeier, J. J., et al. 2000, ApJ, 536, 19
Lang, P., Meidt, S. E., Rosolowsky, E., et al. 2020, ApJ, 897, 122
Lauer, T. R. 1985, ApJS, 57, 473
Laurikainen, E., Salo, H., Buta, R., Knapen, J. H., & Comerón, S. 2010, MNRAS, 405, 1089
Lehmann, I., Becker, T., Fabrika, S., et al. 2005, A&A, 431, 847
Longobardi, A., Arnaboldi, M., Gerhard, O., et al. 2013, A&A, 558, A42
Lynden-Bell, D., Faber, S. M., Burstein, D., et al. 1988, ApJ, 326, 19
McMillan, R., Ciardullo, R., & Jacoby, G. H. 1993, ApJ, 416, 62
Michard, R., & Simien, F. 1988, A&AS, 74, 25
Morelli, L., Pizzella, A., Coccato, L., et al. 2017, A&A, 600, A76
Morelli, L., Pompei, E., Pizzella, A., et al. 2008, MNRAS, 389, 341
Mouhcine, M., Ferguson, H. C., Rich, R. M., Brown, T. M., & Smith, T. E. 2005, ApJ, 633, 810
Muñoz-Mateos, J. C., Gil de Paz, A., Zamorano, J., et al. 2009, ApJ, 703, 1569
Nazé, Y., Rauw, G., Manfroid, J., Chu, Y. H., & Vreux, J. M. 2003, A&A, 408, 171
Neumann, J., Fragkoudi, F., Pérez, I., et al. 2020, A&A, 637, A56
Panagia, N., Gilmozzi, R., Macchetto, F., Adorf, H. M., & Kirshner, R. P. 1991, ApJL, 380, L23
Persson, S. E., Frogel, J. A., & Aaronson, M. 1979, ApJS, 39, 61
Pietrzyński, G., Graczyk, D., Gallenne, A., et al. 2019, Natur, 567, 200
Prugniel, P., & Heraudeau, P. 1998, A&AS, 128, 299
Pulsoni, C., Gerhard, O., Arnaboldi, M., et al. 2018, A&A, 618, A94
Radburn-Smith, D. J., de Jong, R. S., Seth, A. C., et al. 2011, ApJS, 195, 18
Reid, M. J., Pesce, D. W., & Riess, A. G. 2019, ApJL, 886, L27
Reid, W. A., & Parker, Q. A. 2010, MNRAS, 405, 1349
Rekola, R., Richer, M. G., McCall, M. L., et al. 2005, MNRAS, 361, 330
Renzini, A., & Buzzoni, A. 1986, in Spectral Evolution of Galaxies, ed. C. Chiosi & A. Renzini (Dordrecht: D. Reidel), 195
Richer, M. G., & McCall, M. L. 2008, ApJ, 684, 1190
Riess, A. G., Macri, L., Casertano, S., et al. 2011, ApJ, 730, 119
Riess, A. G., Macri, L. M., Hoffmann, S. L., et al. 2016, ApJ, 826, 56
Riess, A. G., Yuan, W., Macri, L. M., et al. 2022, ApJL, 934, L7

Romaniello, M., Zampieri, S., Delmotte, N., et al. 2018, Msngr, 172, 2
Rosado-Belza, D., Falcón-Barroso, J., Knapen, J. H., et al. 2020, A&A, 644, A116
Roth, M. M., Jacoby, G. H., Ciardullo, R., et al. 2021, ApJ, 916, 21
Russell, D. G. 2002, ApJ, 565, 681
Sabbi, E., Calzetti, D., Ubeda, L., et al. 2018, ApJS, 235, 23
Saglia, R. P., Kronawitter, A., Gerhard, O., & Bender, R. 2000, AJ, 119, 153
Sandage, A., & Bedke, J. 1994, The Carnegie Atlas of Galaxies (Washington, D.C.: Carnegie Institution of Washington)
Scheuermann, F., Kreckel, K., Anand, G. S., et al. 2022, MNRAS, 511, 6087
Schlafly, E. F., & Finkbeiner, D. P. 2011, ApJ, 737, 103
Schönberner, D., Jacob, R., Sandin, C., & Steffen, M. 2010, A&A, 523, A86
Schweizer, F., Burns, C. R., Madore, B. F., et al. 2008, AJ, 136, 1482
Shaya, E. J., Tully, R. B., Hoffman, Y., & Pomarède, D. 2017, ApJ, 850, 207
Shen, Z., Danieli, S., van Dokkum, P., et al. 2021, ApJL, 914, L12
Soemitro, A. A., Roth, M. M., Weilbacher, P. M., et al. 2023, A&A, 671, A142
Sorce, J. G., Tully, R. B., Courtois, H. M., et al. 2014, MNRAS, 444, 527
Sparks, W. B., Wall, J. V., Jorden, P. R., Thorne, D. J., & van Breda, I. 1991, ApJS, 76, 471
Spriggs, T. W., Sarzi, M., Galán-de Anta, P. M., et al. 2021, A&A, 653, A167
Spriggs, T. W., Sarzi, M., Napiwotzki, R., et al. 2020, A&A, 637, A62
Springob, C. M., Masters, K. L., Haynes, M. P., Giovanelli, R., & Marinoni, C. 2009, ApJS, 182, 474
Stetson, P. B. 1987, PASP, 99, 191
Thater, S., Krajnović, D., Weilbacher, P. M., et al. 2022, MNRAS, 509, 5416
Theureau, G., Hanski, M. O., Coudreau, N., Hallet, N., & Martin, J. M. 2007, A&A, 465, 71
Tonry, J. L., Blakeslee, J. P., Ajhar, E. A., & Dressler, A. 2000, ApJ, 530, 625
Tonry, J. L., Dressler, A., Blakeslee, J. P., et al. 2001, ApJ, 546, 681
Tremonti, C. A., Heckman, T. M., Kauffmann, G., et al. 2004, ApJ, 613, 898
Tully, R. B. 1988, Nearby Galaxies Catalog (Cambridge: Cambridge Univ. Press)
Tully, R. B., Rizzi, L., Shaya, E. J., et al. 2009, AJ, 138, 323
Valenzuela, L. M., Méndez, R. H., & Miller Bertolami, M. M. 2019, ApJ, 887, 65
van Dokkum, P., Danieli, S., Cohen, Y., et al. 2018, Natur, 555, 629
Varenius, E., Conway, J. E., Martí-Vidal, I., et al. 2014, A&A, 566, A15
Veale, M., Ma, C.-P., Thomas, J., et al. 2017, MNRAS, 464, 356
Weilbacher, P. M., Monreal-Ibero, A., Verhamme, A., et al. 2018, A&A, 611, A95
Weilbacher, P. M., Palsa, R., Streicher, O., et al. 2020, A&A, 641, A28
Willick, J. A., Courteau, S., Faber, S. M., et al. 1997, ApJS, 109, 333
Willmer, C. N. A., Focardi, P., da Costa, L. N., & Pellegrini, P. S. 1989, AJ, 98, 1531
Zabel, N., Davis, T. A., Sarzi, M., et al. 2020, MNRAS, 496, 2155
Zepf, S. E., Stern, D., Maccarone, T. J., et al. 2008, ApJL, 683, L139